

Metal-silicate partitioning systematics of siderophile elements at reducing conditions: A new experimental database

E.S. Steenstra^{a,b,c,*}, A.X. Seegers^b, R. Putter^b, J. Berndt^c, S. Klemme^c, S. Matveev^d, E.S. Bullock^a, W. van Westrenen^b

^a The Geophysical Laboratory, Carnegie Institution of Science, Washington D.C., the United States of America

^b Faculty of Science, Vrije Universiteit Amsterdam, the Netherlands

^c Institute of Mineralogy, University of Münster, Germany

^d Department of Geosciences, Utrecht University, the Netherlands

ARTICLE INFO

Keywords:

Core
Accretion
Mercury
Metal-silicate
Siderophile
Aubrites

ABSTRACT

The differences in FeO mantle contents and core masses between the terrestrial planets suggest the oxygen fugacity (f_{O_2}) during their differentiation likely varied significantly. The metal-silicate partitioning of siderophile (iron-loving) elements is a function of f_{O_2} and of their valence state(s) in silicate melts. Silicon (Si) is known to partition into metal at low f_{O_2} and has been proposed as a possible light element in the cores of Mercury and the aubrite parent body (AuPB).

To systematically study the metal-silicate partitioning behavior of siderophile elements into Si-bearing metal, 69 high pressure (P) – temperature (T) metal-silicate partitioning experiments were performed under moderately to highly reducing conditions. Oxygen fugacities ranged between 1 and 7 units below the iron-wüstite buffer (ΔIW). Experimental pressures and temperatures ranged between 1 and 5 GPa and 1883 to 2273 K, respectively. A comparison of the ΔIW values and the f_{O_2} based on the Si-SiO₂ buffer ($\Delta Si-SiO_2$) indicates that the activity coefficient of FeO in silicate melts decreases significantly from reducing to highly reducing conditions under C-saturated conditions. It was found that at conditions more reducing than $\Delta IW = -3$ to -4 , the metal-silicate partitioning behavior of the majority of the siderophile elements deviates significantly from values corresponding to their expected valence state(s). These results indicate that the activity in metal of the elements considered, including that of Si itself, is decreased as a function of Si metal content, and a thermodynamic approach was used to quantify these effects. Interaction coefficients of trace elements in Si-bearing, Fe-rich alloys (ϵ_M^{Si}) derived from the new experiments are in good agreement with previously proposed values at similar pressures below 5 GPa. However, ϵ_M^{Si} values obtained for C-free systems decrease within the 1 to 11 GPa range, suggesting extrapolation of lower-pressure parameters may yield erroneous results at much higher pressures. Altogether, the new results provide an extensive experimental foundation for future studies of planetary differentiation under (highly) reduced conditions.

1. Introduction

Various lines of geochemical evidence suggest that the redox state during core formation varied considerably among the terrestrial bodies (e.g. Rai and van Westrenen, 2014; Wade and Wood, 2005; Chabot et al., 2014). Mars, the Moon, the angrite parent body and Vesta likely differentiated at 1–2 log units below the iron-wüstite buffer (ΔIW) (e.g. Wadhwa, 2008; Rai and van Westrenen, 2013, 2014; Steenstra et al., 2016, 2017a). The Earth likely accreted at more reducing conditions ($\Delta IW = -4$ to -2) and progressively oxidized during differentiation (e.g. Wade and Wood, 2005; Corgne et al., 2008; Siebert et al., 2011;

Rubie et al., 2015). Mercury may have accreted at even more reducing conditions ($\Delta IW = -2.6$ to -7.3) judging from its low silicate FeO, high S contents of silicate phases and its large metal:silicate mass ratio (e.g. McCubbin et al., 2012; Hauck II et al., 2013; Zolotov et al., 2013; Chabot et al., 2014; Malavergne et al., 2014; Knibbe and van Westrenen, 2015; Namur et al., 2016). Mercury's bulk composition should be dominated by or include Bencubbinite (CB) and/or EH chondrite-like materials, both of which are highly reduced relative to other chondrite groups (Malavergne et al., 2010; Brown and Elkins-Tanton, 2009; Namur et al., 2016; Nittler et al., 2019). The parent body of the aubrites, a suite of highly reduced achondrites, may also have

* Corresponding author at: The Geophysical Laboratory, Carnegie Institution of Science, Washington D.C., the United States of America.

E-mail address: steenstra@carnegiescience.edu (E.S. Steenstra).

<https://doi.org/10.1016/j.icarus.2019.113391>

Received 21 February 2019; Received in revised form 17 July 2019; Accepted 29 July 2019

Available online 05 August 2019

0019-1035/ © 2019 Elsevier Inc. All rights reserved.

Table 1
Experimental conditions.

Run	P (GPa)	T(K)	t (min)	Starting comp. ^b	ΔIW ^c <i>ideal</i>	$\Delta Si-SiO_2$ ^d <i>ideal</i>	γ_{Fe}^{metal} ^e	γ_{Si}^{metal} ^f	ΔIW ^g <i>non-ideal</i>	$\Delta Si-SiO_2$ ^h <i>non-ideal</i>	$\gamma_{FeO}^{silicate}$ ⁱ	ΔIW ^j <i>corrected for $\gamma_{FeO}^{silicate}$</i>
<i>C saturated</i>												
GGR1Si-1	1.0	1883	60	GG; 1 wt% Si + MSE1	-1.77	-	0.72	0.059	-1.49	-	1	-1.49
GGR1Si-2	1.0	1883	15	GG; 1 wt% Si + MSE1	-2.75	-	0.72	0.055	-2.46	-	1	-2.46
GGR1Si-3	1.0	1883	30	GG; 1 wt% Si + MSE1	-1.65	-	0.72	0.054	-1.36	-	1	-1.36
GGR1Si-4	1.5	1883	60	GG; 1 wt% Si + MSE1	-1.10	6.77	0.72	0.057	-0.81	9.27	1	-0.81
GGR1Si-5	2.0	1883	60	GG; 1 wt% Si + MSE1	-1.06	6.59	0.72	0.051	-0.77	9.18	1	-0.77
GGR1Si-6	2.5	1883	5	GG; 1 wt% Si + MSE1	-1.29	6.13	0.72	0.053	-1.00	8.69	1	-1.00
GGR1Si-4b	1.5	1883	60	GG; 1 wt% Si + MSE1	-1.63	6.28	0.72	0.051	-1.35	8.87	1	-1.35
GGR1Si-5b	2.0	1883	60	GG; 1 wt% Si + MSE1	-1.49	6.73	0.72	0.053	-1.21	9.28	1	-1.21
GGR1Si-6b	2.5	1883	60	GG; 1 wt% Si + MSE1	-1.77	-	0.72	0.053	-1.49	-	1	-1.49
GGR3-Si1	1.0	1883	5	GG; 3 wt% Si + MSE1	-4.53	2.75	0.68	0.073	-4.20	5.02	1	-4.20
GGR3-Si2	1.5	1883	60	GG; 3 wt% Si + MSE1	-4.82	2.30	0.66	0.082	-4.47	4.48	1	-4.47
GGR3-Si3	2.0	1883	60	GG; 3 wt% Si + MSE1	-1.94	6.65	0.71	0.074	-1.64	8.91	1	-1.64
GGR3-Si4	2.5	1883	60	GG; 3 wt% Si + MSE1	-4.22	2.33	0.66	0.084	-3.86	4.49	1	-3.86
GGR3-Si1b	1.0	1883	60	GG; 3 wt% Si + MSE1	-4.99	2.41	0.67	0.079	-4.63	4.62	1	-4.63
GGR3-Si2b	1.5	1883	60	GG; 3 wt% Si + MSE1	-4.97	2.30	0.66	0.081	-4.61	4.49	1	-4.61
GGR3-Si3b	2.0	1883	60	GG; 3 wt% Si + MSE1	-4.32	2.83	0.69	0.075	-3.99	5.09	1	-3.99
GGR3-Si4b	2.5	1883	60	GG; 3 wt% Si + MSE1	-4.11	2.81	0.69	0.076	-3.78	5.05	1	-3.78
GGR6Si-1	1.0	1883	30	GG; 6 wt% Si + MSE1	-5.45	1.68	0.57	0.130	-4.97	3.45	0.71	-5.26
GGR6Si-2	1.5	1883	30	GG; 6 wt% Si + MSE1	-4.81	1.54	0.55	0.128	-4.29	3.33	0.30	-5.35
GGR6Si-3 ^k	2.0	1883	60	GG; 6 wt% Si + MSE1	-3.80	1.63	0.58	0.104	-3.33	3.59	0.12	-5.17
GGR6Si-4	2.5	1883	60	GG; 6 wt% Si + MSE1	-4.40	1.76	0.59	0.121	-3.94	3.60	0.25	-5.16
GGR6Si-1b ^l	1.0	1883	60	GG; 6 wt% Si + MSE1	-3.83	1.63	0.53	0.189	-3.28	3.08	0.076	-5.52
GGR6Si-2b	1.5	1883	45	GG; 6 wt% Si + MSE1	-5.15	1.76	0.59	0.115	-4.69	3.64	0.60	-5.13
GGR6Si-3b	2.0	1883	60	GG; 6 wt% Si + MSE1	-4.86	1.77	0.60	0.107	-4.41	3.71	0.46	-5.08
GGR6Si-4b	2.5	1883	60	GG; 6 wt% Si + MSE1	-4.51	1.56	0.56	0.123	-4.01	3.38	0.22	-5.31
GGRFeSi-1	1.0	1883	60	GG; Fe ₈₃ Si ₁₇ + MSE2	-5.03	0.93	0.49	0.099	-4.41	2.94	0.25	-5.62
GGRFeSi-2	1.5	1883	60	GG; Fe ₈₃ Si ₁₇ + MSE2	-2.57	0.91	0.49	0.100	-1.95	2.92	0.014	-5.64
GGRFeSi-3	2.0	1883	30	GG; Fe ₈₃ Si ₁₇ + MSE2	-2.83	0.87	0.49	0.101	-2.21	2.86	0.018	-5.67
GGRFeSi-4	2.5	1883 ^m	60	GG; Fe ₈₃ Si ₁₇ + MSE2	-2.08	0.85	0.50	0.095	-1.48	2.89	0.008	-5.65
GGRFeSi-5	1.0	1883	30	GG; Fe ₈₃ Si ₁₇ + MSE3	-4.07	1.24	0.49	0.143	-3.45	2.92	0.081	-5.63
GGRFeSi-6	1.5	1883 ^l	30	GG; Fe ₈₃ Si ₁₇ + MSE3	-2.86	1.26	0.59	0.131	-2.26	3.02	0.022	-5.56
GGRFeSi-7	1.5	1883	60	GG; Fe ₈₃ Si ₁₇ + MSE3	-2.67	1.44	0.56	0.105	-2.17	3.40	0.027	-5.30
GGRFeSi-8	2.0	1883	60	GG; Fe ₈₃ Si ₁₇ + MSE3	-3.35	1.26	0.50	0.135	-2.76	3.00	0.039	-5.58
KBR1Si-1	1.0	1883	60	KB, 1 wt% Si + MSE1	-1.72	6.19	0.72	0.052	-1.43	8.75	1	-1.43
KBR3Si-1	1.0	1883	5	KB, 3 wt% Si + MSE1	-4.51	2.52	0.68	0.060	-4.18	4.96	1	-4.18
KBR6Si-1	1.0	1883	60	KB, 6 wt% Si + MSE1	-5.20	2.08	0.63	0.104	-4.79	4.04	0.94	-4.85
<i>C-free</i>												
LG1Si-1	1	1883	125	LG; 1 wt% Si + VSE	-2.67	6.17	1.00	0.009	-2.67	10.31	1	-2.67
LG1Si-2	1	1883	60	LG; 1 wt% Si + VSE	-3.07	5.08	1.00	0.009	-3.07	9.22	1	-3.07
LG1Si-3	1	1883	18	LG; 1 wt% Si + VSE	-3.55	3.83	1.00	0.009	-3.55	7.95	1	-3.55
LG1Si-4	2	1883	15	LG; 1 wt% Si + VSE	-2.66	5.32	1.00	0.009	-2.66	9.45	1	-2.66
LG1Si-5	2.5	1883	15	LG; 1 wt% Si + VSE	-2.41	5.94	1.00	0.009	-2.41	10.06	1	-2.41
GG1Si-1	1	1883	30	GG; 1 wt% Si + VSE	-1.74	8.13	1.00	0.009	-1.74	12.26	1	-1.74
GG1Si-2	2	1883	30	GG; 1 wt% Si + VSE	-2.19	7.25	1.00	0.008	-2.19	11.40	1	-2.19
GG1Si-3	2.5	1883	30	GG; 1 wt% Si + VSE	-2.32	6.79	1.00	0.008	-2.32	10.94	1	-2.32
GG3Si-1	1	1883	30	GG; 3 wt% Si + VSE	-4.04	2.59	0.99	0.009	-4.03	6.71	1	-4.03
GG3Si-2	2	1883	30	GG; 3 wt% Si + VSE	-4.07	1.89	0.97	0.011	-4.05	5.83	1	-4.05
GG3Si-3	2.5	1883	5	GG; 3 wt% Si + VSE	-3.71	1.99	0.96	0.011	-3.68	5.90	1	-3.68
GG6Si-1	1	1883	30	GG; 6 wt% Si + VSE	-5.06	1.55	0.95	0.012	-5.02	5.39	1	-5.02
GG6Si-2	2	1883	30	GG; 6 wt% Si + VSE	-4.50	1.63	0.94	0.013	-4.45	5.42	1	-4.45
GG6Si-3	2.5	1883	30	GG; 6 wt% Si + VSE	-3.90	2.73	0.99	0.008	-3.89	6.88	1	-3.89
GG6Si-1b	1	1883	30	GG; 6 wt% Si + VSE	-5.11	1.50	0.94	0.013	-5.05	5.26	1	-5.05
GG6Si-2b	2	1883	30	GG; 6 wt% Si + VSE	-4.61	1.44	0.91	0.015	-4.53	5.07	1	-4.53
GG6Si-3b	2.5	1883	30	GG; 6 wt% Si + VSE	-4.11	1.56	0.92	0.015	-4.04	5.22	1	-4.04
GGRFeSi-1	1	1883	30	GG; Fe ₈₃ Si ₁₇ + VSE	-7.08	0.80	0.79	0.028	-6.87	3.90	1	-6.87
GGRFeSi-2	2	1883	30	GG; Fe ₈₃ Si ₁₇ + VSE	-5.76	0.76	0.76	0.034	-5.52	3.69	1	-5.52
GGRFeSi-3	2.5	1883	30	GG; Fe ₈₃ Si ₁₇ + VSE	-5.47	0.86	0.74	0.035	-5.20	3.77	1	-5.20
GGRFeSi-1b	1	1883	30	GG; Fe ₈₃ Si ₁₇ + VSE	-6.62	0.94	0.85	0.022	-6.48	4.27	1	-6.48
GGRFeSi-2b	2	1883	30	GG; Fe ₈₃ Si ₁₇ + VSE	-5.18	1.04	0.83	0.025	-5.02	4.24	1	-5.02
GGRFeSi-3b	2.5	1883	30	GG; Fe ₈₃ Si ₁₇ + VSE	-5.44	0.89	0.73	0.039	-5.17	3.72	1	-5.17
PR1451	4(109) ^a	2173	5	GG; Fe ₈₃ Si ₁₇ + VSE	-5.60	0.81	0.90	0.031	-5.51	3.82	1	-5.51
PR1453	4(109)	2140 ^m	5	GG; 6 wt% Si + VSE	-5.68	0.77	0.89	0.034	-5.57	3.72	1	-5.57
PR1455	4(109)	2173	5	GG; 3 wt% Si + VSE	-4.79	2.35	0.99	0.015	-4.78	5.97	1	-4.78
PR1457	4(109)	2173	0.5	GG; 6 wt% Si + VSE	-5.60	0.56	0.81	0.050	-5.41	3.16	1	-5.41
PR1458	4(109)	2260 ^m	5	GG; 3 wt% Si + VSE	-5.10	1.89	0.98	0.017	-5.08	5.45	1	-5.08

(continued on next page)

Table 1 (continued)

Run	P (GPa)	T(K)	t (min)	Starting comp. ^b	ΔIW^c ideal	$\Delta\text{Si-SiO}_2^d$ ideal	$\gamma_{\text{Fe}}^{\text{metal } e}$	$\gamma_{\text{Si}}^{\text{metal } f}$	ΔIW^g non-ideal	$\Delta\text{Si-SiO}_2^h$ non-ideal	$\gamma_{\text{FeO}}^{\text{silicate } i}$	ΔIW^j corrected for $\gamma_{\text{FeO}}^{\text{silicate}}$
PR1459	4(109)	2173	5	GG; Fe ₈₃ Si ₁₇ + VSE	-6.57	0.50	0.81	0.051	-6.39	3.10	1	-6.39
PR1512	5(145)	2273	4	GG; Fe ₈₃ Si ₁₇ + VSE	-5.64	0.78	0.90	0.038	-5.55	3.62	1	-5.55
PR1513	5(145)	2273	4	GG; 6 wt% Si + VSE	-5.40	0.95	0.92	0.034	-5.32	3.89	1	-5.32
PR1514	5(145)	2273	4	GG; 3 wt% Si + VSE	-4.70	1.51	0.97	0.023	-4.67	4.77	1	-4.67
PR1515	5(145)	2273	4	GG; 1 wt% Si + VSE	-3.65	3.66	1.00	0.017	-3.65	7.21	1	-3.65

^a Numbers in parentheses represent oil pressure in bars ^b GG: Apollo 15 green glass; LG: lunar granite; KB = Knippa Basalt (see Steenstra et al., 2017a, 2017b and references therein); MSE (moderately siderophile elements) and VSE (volatile siderophile elements) refer to trace element compositions of metallic synthetic starting mixtures (MSE1 = P, V, Cr, Mn, Ni, Cu, Ge, Mo, Sn, W; MSE2 = V, Cr, Mn, Cu, Sn, W; MSE3 = P, V, Cr, Mn, Ni, Ge, Mo; VSE = Ni, As, Se, Cd, In, Sb, Te, Pb) ^c oxygen fugacity relative to the Fe-FeO buffer derived assuming ideal $\gamma_{\text{FeO}}^{\text{silicate}}$, $\gamma_{\text{Fe}}^{\text{metal}} = 1$ ^d oxygen fugacity relative to the Si-SiO₂ buffer derived assuming ideal $\gamma_{\text{SiO}_2}^{\text{silicate}}$, $\gamma_{\text{Si}}^{\text{metal}} = 1$ ^e values of $\gamma_{\text{Fe}}^{\text{metal}}$ were calculated using the online metal activity calculator (Wade and Wood, 2005) ^f Values of $\gamma_{\text{Si}}^{\text{metal}}$ were calculated using the online metal activity calculator (Wade and Wood, 2005) ^g Oxygen fugacity relative to the Fe-FeO buffer derived using reported $\gamma_{\text{Fe}}^{\text{metal}}$ values and assuming ideal $\gamma_{\text{FeO}}^{\text{silicate}} = 1$ ^h Oxygen fugacity relative to the Si-SiO₂ buffer derived using reported $\gamma_{\text{Si}}^{\text{metal}}$ values and assuming ideal $\gamma_{\text{SiO}_2}^{\text{silicate}} = 1$ ⁱ Calculated $\gamma_{\text{FeO}}^{\text{silicate}}$ values for GGR6Si, GGRFeSi and KBR6Si runs, that were derived by using the correlation between $\Delta\text{Si-SiO}_2$ and ΔIW ($\Delta\text{IW} = 0.7203 * \Delta\text{Si-SiO}_2 - 7.6597$; $R^2 = 0.97$; Fig. 2.) ^j Calculated assuming $\gamma_{\text{FeO}}^{\text{silicate}}$ values derived using the relationship between $\Delta\text{Si-SiO}_2$ and ΔIW . The ΔIW values in this column are the recommended values and will be used throughout the study ^k The metal consisted of both Si-poor and Si-rich phases (l) The metal suffered from significant Pt contamination and was therefore excluded from further analyses ^m Run temperatures were approximated using output power – temperature relationships.

experienced core formation under extremely reducing conditions ($\Delta\text{IW} = -5$; Casanova et al., 1993).

The outcomes of geochemical core formation models are largely based on combining observed siderophile element depletions in planetary mantles with experimental measurements of metal-silicate siderophile element partitioning. The metal-silicate partitioning of elements is affected by the $f\text{O}_2$ during metal/silicate segregation and by changes in their valence state(s) in silicate melts. Some siderophile elements, including Cr, Ge, Sn, Mo, W, show a transition in valence state as a function of $f\text{O}_2$, pressure (P), temperature (T) and/or composition (e.g. Capobianco and Amelin, 1994; Capobianco et al., 1999; Corgne et al., 2008; Righter et al., 2011; Righter et al., 2016; Steenstra et al., 2017a).

At the $f\text{O}_2$ relevant for differentiation of Mercury and the Aubrite Parent Body (AuPB), Si is expected to partition into metal (e.g. Kilburn and Wood, 1997; Wade and Wood, 2005; Ricolleau et al., 2011; Righter et al., 2017, 2018; Vogel et al., 2018). Although the effects of Si in metal on the activities of siderophile elements and on the resulting metal-silicate partition coefficients have been studied in these previous works, the extent to which these effects change with pressure is unconstrained. Similarly, the intrinsic variables that affect the metal-silicate partitioning of Si itself is not well quantified. Some authors suggest significant pressure effects (Wade and Wood, 2005; Ricolleau et al., 2011), whereas others argue that Si metal-silicate partitioning is only affected by changes in silicate melt composition (Tuff et al., 2011).

Here, we present an extensive database consisting of over 950 new experimentally determined metal-silicate partition coefficients for nominally lithophile (oxygen-loving) and siderophile elements (Si, P, Ti, V, Cr, Mn, Ni, Cu, Zn, Ga, Ge, As, Se, Mo, Cd, In, Sn, Sb, Te, W, Pb) at high P - T and moderately to highly reducing conditions. These results are used to 1) assess the effects of $f\text{O}_2$ on their metal-silicate partitioning behavior; 2) quantify interaction coefficients that describe the effects of dissolved Si in metal on their activities in Fe-rich alloys and 3) assess if/how these interaction coefficients change with pressure.

2. Methods

2.1. Experimental techniques

Lower P - T experiments were performed in a Bristol type end-loaded piston cylinder (PC) press (Boyd and England, 1960) in the high-pressure laboratory at the Vrije Universiteit Amsterdam, the Netherlands. Higher P - T experiments were conducted using a 1500-ton multi-anvil (MA) apparatus at the Geophysical Laboratory, Carnegie Institution of Science, Washington D.C., United States. Thirty-six PC experiments were

conducted in graphite capsules (1.7 mm O.D., 0.7 mm I.D., 4–5 mm long) placed within sealed Pt outer capsules (2 mm O.D., 1.7 mm I.D., 7–8 mm long) (Table 1). The other 23 PC experiments and all 10 MA experiments were conducted in MgO capsules manufactured from polycrystalline MgO rods (3 mm O.D., 1.5 mm I.D.; 3 mm long for MA; 4 mm long for PC). Sixty-one experiments were performed using a synthetic analogue of a primitive basaltic composition modelled after the primitive lunar Apollo 15C green glass (GG, chosen to facilitate comparison to previous studies; Steenstra et al., 2017a). Three experiments were run with a terrestrial Knippa basaltic composition (KB) and five using a lunar granitic composition (LG) (Table 1–3; Steenstra et al., 2017a; Appendix Section A.1).

Metal powder mixtures were prepared by doping high-purity Fe metal powder with variable amounts (0.5 to 1.5 wt%) of siderophile elements P, V, Cr, Mn, Cu, Ge, As, Se, Mo, Cd, In, Sn, Sb, Te, W, Pb and 0 to 5 wt% Ni (Table 1). Four metal trace element powders were made with each containing a characteristic set of elements (moderately siderophile element sets “MSE1, MSE2, MSE3”; and volatile siderophile element set “VSE”; Table 1). Variable amounts of Fe₈₃Si₁₇ (based on mass proportions) were added to these mixtures to generate different $f\text{O}_2$ and Si concentrations in the metal. The silicate and metal mixtures were loaded in a 2:1 ratio by weight into the capsule. After filling and insertion of the graphite capsules, the Pt capsules were crimped and welded shut. The MgO capsules were fitted with a tightly fitting lid.

The PC experiments were conducted at a constant temperature of 1883 K and pressures between 1 and 2.5 GPa using a 13 mm diameter talc-pyrex pressure cell assembly that consists of concentric sleeves of natural talc (outer), pyrex glass (inner), a graphite furnace and a MgO crushable spacer. This assembly was pressure calibrated by van Kan Parker et al. (2011), based on the fayalite + quartz = ferrosillite and albite = jadeite + quartz equilibria, resulting in a friction correction of < 3% and a pressure uncertainty of 0.1 GPa. Experimental run temperatures were measured and controlled using a type “D” W–Re (W₉₇–Re₃ – W₇₅–Re₂₅) thermocouple contained in a four-bore alumina sleeve. Platinum capsules were glued in the MgO sleeve. A 0.6 mm thick ruby disc was placed between the Pt/MgO capsule and thermocouple to prevent puncture of the capsule through the thermocouple tip. This increased the distance between the thermocouple tip and sample, resulting in a 10 K deviation from the measured temperature (Wood et al., 2014). Reported temperatures were adjusted 10 K upwards as done in previous work (Steenstra et al., 2017a). After initial compression to 0.5 GPa, samples were heated at a rate of 100 K/min to 1073 K. At 1073 K, samples sintered for 60 min to reduce surface tension and minimize infiltration of metal into the graphite/MgO capsule, followed by further heating at a rate of 100 K/min to 1883 K (Table 1). Pressure was gradually increased during heating.

Multi-anvil experiments were conducted using 18 mm edge length Cr-doped MgO (run PR1458) or ZrO₂ octahedra (all other runs). In run PR1458, a ZrO₂ sleeve was used as an additional thermal insulator. All MA experiments were conducted using graphite heaters and MgO spacers. Temperatures were monitored and controlled using a type “C” W–Re (W₉₅-Re₅ - W₇₄-Re₂₆) thermocouple that was contained in a four bore Al₂O₃ sleeve. Temperature uncertainties are estimated to be 25 K for this particular setup (van Westrenen et al., 2003; Corgne et al., 2007). The pressure calibrations for MA experiments were based on Corgne et al. (2007). In the MA experiments samples were first pressurized to target pressure and subsequently heated at a rate of 100 K/min to 1273 K. The samples were then sintered for 1 to 2 h and after this heated at 150 K/min to the target temperature (2173–2273 K).

Peak temperature run times were 0.5–125 min but generally between 30 and 60 min to ensure a steady state between metal and silicate (Table 1; Appendix Section A.4). Run times for experiments conducted in MgO capsules were shorter to prevent extreme MgO enrichment of the silicate melts due to chemical reaction with the capsule walls. Run durations of 15 min had previously been shown to be sufficient for attaining a steady state between metals and silicates in similar experimental set-ups at comparable conditions (Siebert et al., 2011; Tuff et al., 2011; Steenstra et al., 2017a, 2017b), and a time series performed specifically for the current study confirms this (Appendix Section A.4). At the end of the desired run times, experiments were rapidly quenched by shutting off the power to the furnace while maintaining pressure. The capsules were mounted in petropoxy resin, sectioned and polished to a fine (< 1 µm) finish for electron microprobe analyser (EPMA) and laser ablation inductively coupled plasma mass spectrometry (LA-ICP-MS) analyses.

2.2. Analytical techniques

Silicate and metal major element abundances were determined with a JXA JEOL 8530F field emission electron probe micro analyser at the Dutch National Geological Facility at Utrecht University, the Netherlands (Tables 2–5). Analyses were performed using a defocused beam because of the textures of the quenched silicate melts (containing spinifex crystals of olivine in a glassy matrix) and metallic melt (containing Fe-rich and Si-rich quench phases, Fig. 1). Measurement points were set in lines and/or raster grids, depending of the available surface area of the analysed phases. Care was taken to avoid analysis of areas close the edge of each phase and/or the graphite/MgO capsule. The beam size was approximately equivalent to the step size (5–15 µm), while using a beam current of 20 nA and an accelerating voltage of 15 kV. Dwell times of 20–30 s on peak and 10–15 s on each background were used. At least 25 repeat analyses were performed for the metal and silicate phases.

Metal standards were KTiPO₅ for P, tephroite for Mn, galena for Pb, InAs for In and As, CdS for Cd, diopside for Si and pure metal standards for V, Cr, Fe, Ni, Cu, Ge, Se, Sn, Sb, Mo, W and Pt. Silicate analyses were calibrated using diopside for Si and Ca, forsterite for Mg, corundum for Al, hematite for Fe, tephroite for Mn, KTiPO₅ for P and K, TiO₂ for Ti, jadeite for Na and pure metal standards for V, Cr, Fe, Ni, Cu, Ge, Se, Sn, Sb, Mo, W and Pt. Primary standards were also used as secondary standards. Calibrations were considered successful when the primary standard compositions were reproduced within 1% relative deviation. Data-reduction was performed using the $\Phi(\rho Z)$ correction (Armstrong, 1995). For more details on EPMA analyses and quantitative assessments of the reliability of the EPMA approach employed here, the reader is referred to Steenstra et al. (2019).

Carbon contents in the C-saturated metallic alloys were determined with a JXA JEOL 8530F field emission EPMA at the Carnegie Institution for Science utilizing a cold-finger to minimize hydrocarbon contamination in the chamber (Table 4; Robaut et al., 2006). Prior to

analyses, samples were iridium coated using a Cressington sputter coater at the Geophysical Laboratory. The beam current was 30 nA, the accelerating voltage was 15 kV and the beam size varied between 5 and 20 µm. Carbon was measured simultaneously with Fe, Ni and Si. Standards consisted of synthetic Fe₃C and Fe₇C₃ (Liu et al., 2016), Fe metal, Ni metal and a basaltic glass. The C concentrations were recalculated to include elements present but not analysed for, in order to obtain the appropriate matrix corrections.

LA-ICP-MS at the University of Münster, Germany, was used to quantify the abundances of trace elements (Tables 2–5; Appendix Section A.2). Sample ablation of metals and silicates was done with a pulsed 193 nm ArF excimer laser (Analyte G2, Photon Machines) using a repetition rate of 10 Hz and an energy of ~3–4 J/cm². Beam diameters were varied between 25 and 50 µm, depending on the available surface area. The following isotopes were measured: ²⁹Si, ³¹P, ⁴³Ca, ⁴⁹Ti, ⁵¹V, ⁵³Cr, ⁵⁵Mn, ⁶⁰Ni, ⁶¹Ni, ⁶³Cu, ⁶⁶Zn, ⁶⁹Ga, ⁷³Ge, ⁷⁵As, ⁸²Se, ⁹⁵Mo, ¹¹¹Cd, ¹¹⁵In, ¹¹⁸Sn, ¹²¹Sb, ¹²⁵Te, ¹⁸²W, ¹⁹⁵Pt and ²⁰⁸Pb, with yields calibrated on the NIST 612 glass standard as primary reference material. USGS basaltic glass standards BCR-2G and BIR-1G were used to monitor precision and accuracy for silicate phases. Results match or are close to the published range of elemental concentrations given in the GeoRem database (version 18; Jochum et al., 2005). Internal standards for metal and silicate were Ni and Si, respectively, with their abundances quantified using EMPA, except for GGRFeSi runs (Table 1), for which Si was used as a metal internal standard. Data reduction was performed with GLITTER software (van Achterbergh et al., 2001; Griffin et al., 2008) and was also used to monitor and/or identify the ablation of heterogeneities such as metal inclusions in silicate phases or cracks.

In Appendix Section A.2 and Steenstra et al. (2019) we show that there is good agreement between the measured and reported trace element abundances in a variety of silicate reference materials. There is also good agreement between trace elements abundances (> 300–400 ppm) measured in the silicate melt by LA-ICP-MS and EMPA. For some elements in the metal, corrections on LA-ICP-MS values are required due to preferential ablation of volatile elements and insufficient ablation of refractory elements (Steenstra et al., 2019; Appendix Section A.2). All metal-silicate partition and exchange coefficients reported here are based on EPMA measurements of metals in the case of major elements in the metal, whereas for trace elements LA-ICP-MS values were used that were corrected as discussed and/or described in Appendix Section A.2 and Steenstra et al. (2019).

2.3. Metal-silicate partitioning of siderophile elements

Metal-silicate partitioning of siderophile elements can be considered as a reaction that describes the distribution of element M between a metal phase and a silicate melt (Eq. 1):



where n is the valence of the cation M in the silicate melt. The partition coefficient D_M^* is defined as the ratio between the molar fraction of M in the metal and $MO_{n/2}$ in the silicate melt (Eq. (2)):

$$D_M^* = \frac{x_M^{\text{metal}}}{x_{MO_{n/2}}^{\text{silicate}}} \quad (2)$$

Effects of P - T on metal-silicate partitioning can be identified by considering that the metal-silicate exchange of cation M is related to the reduction-oxidation of Fe-FeO (Wade and Wood, 2005; Corgne et al., 2008):

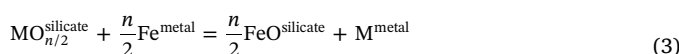


Table 2
Silicate melt major and minor element composition of silicate melts of GGR-KBR series (C-saturated experiments).

Run #	GGR1Si-1	GGR1Si-2	GGR1Si-3	GGR1Si-4	GGR1Si-5	GGR1Si-6	GGR1Si-4b	GGR1Si-5b	GGR1Si-6b	GGR3Si-1	GGR3Si-2	GGR3Si-3	GGR3Si-4
EMPA	N = 55 ^a	N = 36	N = 32	N = 25	N = 26	N = 27	N = 26	N = 24	N = 22	N = 23	N = 27	N = 29	N = 30
MgO(wt%)	15.71(2) ^b	15.57(3)	14.01(5)	13.78(19)	13.97(21)	15.50(13)	16.89(3)	16.48(7)	17.19(6)	17.49(12)	19.07(4)	14.79(3)	15.78(8)
SiO ₂	54.36(13)	63.04(7)	52.60(11)	46.27(16)	44.80(23)	47.63(10)	52.73(6)	50.72(19)	53.29(10)	64.16(32)	62.78(6)	57.97(9)	63.21(18)
Al ₂ O ₃	6.93(1)	6.60(2)	6.00(3)	5.92(5)	5.87(11)	6.52(5)	7.09(2)	7.32(3)	7.50(3)	7.69(3)	7.97(2)	6.23(2)	9.40(3)
CaO	7.28(1)	6.95(1)	6.01(1)	6.18(6)	6.31(7)	7.12(4)	7.85(1)	8.15(2)	8.25(2)	8.14(3)	8.75(2)	6.58(1)	10.01(5)
FeO	9.60(2)	3.19(2)	11.15(6)	20.79(10)	21.94(35)	16.92(22)	11.66(4)	13.72(6)	9.88(3)	0.23(1)	0.21(1)	7.68(2)	0.54(3)
K ₂ O	0.043(1)	0.119(2)	0.545(3)	0.06(1)	0.06(1)	0.025(4)	b.d.l. ^c	b.d.l.	0.015(2)	0.037(2)	0.037(2)	0.182(2)	0.055(5)
Na ₂ O	0.347(4)	1.16(1)	2.08(2)	0.33(3)	0.60(5)	0.11(1)	0.061(4)	0.048(4)	0.044(4)	0.40(1)	0.23(1)	0.67(1)	0.44(1)
MnO	0.221(4)	0.31(1)	0.27(1)	0.20(1)	0.20(1)	0.22(1)	0.23(1)	0.22(1)	0.25(1)	0.27(1)	0.28(1)	0.291(5)	0.29(1)
V ₂ O ₅	1.74(1)	0.52(1)	2.45(2)	1.83(2)	1.82(3)	1.26(2)	1.21(1)	0.90(1)	1.33(2)	< 0.02(1)	b.d.l.	1.15(1)	< 0.02(1)
Cr ₂ O ₃	1.46(1)	0.69(1)	2.05(3)	1.87(3)	1.65(3)	1.42(3)	1.52(1)	1.51(1)	1.60(2)	0.09(1)	0.077(5)	1.24(1)	0.065(4)
TiO ₂	0.224(3)	0.223(5)	0.198(5)	0.19(1)	0.19(1)	0.209(4)	0.24(1)	0.242(5)	0.25(1)	0.223(5)	0.217(5)	0.199(4)	0.207(4)
P ₂ O ₅	0.083(4)	0.03(1)	0.08(1)	0.32(1)	0.33(4)	0.19(2)	0.06(1)	0.15(1)	0.03(1)	–	–	0.02(1)	–
SnO ₂	0.06(1)	< 0.02	0.15(1)	0.21(4)	0.20(6)	0.15(4)	0.09(1)	0.11(1)	0.08(1)	–	–	0.15(1)	–
Total	98.10(14)	98.43(8)	97.61(11)	97.96(27)	97.93(17)	97.28(26)	99.62(9)	99.57(22)	99.69(10)	98.87(20)	99.63(6)	97.15(12)	100.00(7)

LA-ICP-MS	N = 8	N = 8	N = 6	N = 12	N = 11	N = 9	N = 9	N = 4	N = 7	N = 8	N = 7	N = 10	N = 9	N = 6	N = 10
	N (P) = 8 ^e	N (P) = 5	N (P) = 5	N (P) = 5	N (P) = 5	N (P) = 5	N (P) = 10	N (P) = 4	N (P) = 4	N (P) = 5	N (P) = 4	N (P) = 6	N (P) = 6	N (P) = 6	N (P) = 5
CaO (wt%)	6.83(3)	6.84(2)	6.18(7)	5.69(5)	6.23(4)	9.03(13)	7.78(2)	8.21(6)	7.89(2)	8.77(5)	8.60(6)	6.27(3)	8.67(21)		
P (ppm)	218(3)	37(3)	468(20)	1963(17)	1956(25)	1044(39)	341(3)	731(16)	231(2)	29(3)	33(4)	89(10)	40(11)		
Ti	1357(8)	1416(10)	1293(13)	1149(11)	1243(7)	1740(25)	1506(8)	1559(8)	1539(5)	1595(15)	1348(14)	1254(6)	1168(24)		
V	10720(53)	2899(67)	16166(498)	10826(136)	11369(90)	100060(149)	7863(68)	5839(40)	8399(55)	241(8)	136(2)	7182(32)	168(4)		
Cr	8977(39)	4215(70)	13707(363)	11542(132)	10725(102)	11423(142)	8904(96)	9058(73)	9220(56)	865(25)	513(8)	7835(35)	381(7)		
Mn	1626(6)	2236(11)	2003(17)	1319(10)	1448(8)	2077(31)	1680(5)	1561(8)	1763(4)	2345(20)	2044(98)	2097(10)	1999(32)		
Fe	–	–	–	–	–	–	–	–	–	–	1459(26)	56,123(649)	–		
Ni	6.4(10)	b.d.l.	7.1(6)	15(2)	6.3(7)	33(2)	10(1)	14(1)	9.0(4)	2.6(1)	2.07(1)	6.1(5)	b.d.l.		
Cu	6.0(5)	57(6)	75(5)	9.5(7)	10(1)	288(17)	30(3)	30(8)	59(2)	62(4)	3.0(12)	16.7(5)	6.4(7)		
Zn	n.d. ^d	n.d.	50(2)	n.d.	n.d.	n.d.	570(9)	365(5)	524(4)	n.d.	n.d.	n.d.	n.d.		
Ga	n.d.	n.d.	0.9(1)	n.d.	n.d.	n.d.	1.5(1)	1.9(4)	1.43(5)	n.d.	n.d.	n.d.	n.d.		
Ge	31(1)	3.9(4)	26(2)	60(1)	114(5)	65(1)	27(1)	30(1)	19.5(2)	1.7(1)	1.5(1)	17.6(2)	6.6(12)		
Mo	0.22(3)	0.21(4)	0.7(2)	2.1(1)	4.9(3)	2.9(2)	0.4(1)	0.5(1)	0.27(3)	0.5(1)	0.5(1)	0.27(2)	1.0(3)		
In	67(1)	1.7(1)	6.2(1)	6.4(2)	7.9(1)	6.5(2)	4.60(4)	5.0(1)	4.25(4)	0.42(2)	b.d.l.	5.49(4)	1.3(1)		
Sn	932(5)	396(12)	1656(17)	1735(52)	2138(35)	1764(36)	1217(11)	1326(14)	1113(11)	83(6)	49(1)	1453(12)	46(2)		
W	9(1)	0.27(4)	22(2)	120(2)	223(8)	34(2)	14.7(2)	28(1)	5.6(2)	0.5(1)	0.3(1)	3.7(1)	0.4(1)		
Pt	0.032(3)	1.67(4)	2.4(16)	11(5)	6.7(44)	11(5)	34(21)	26(11)	0.08(2)	0.12(1)	40(15)	0.06(1)	40(19)		
Pb	3.5(1)	2.98(3)	7.7(4)	3.8(2)	5.7(3)	4.9(1)	33(1)	22.2(2)	28.0(4)	1.01(4)	1.0(1)	6.0(1)	0.65(4)		

Run #	GGR3Si-1b	GGR3Si-2b	GGR3Si-3b	GGR3Si-4b	GGR6Si-1	GGR6Si-2	GGR6Si-3	GGR6Si-4	GGR6Si-1b	GGR6Si-2b	GGR6Si-3b	GGR6Si-4b	GGRFeSi1
EMPA	N = 34	N = 29	N = 24	N = 27	N = 27	N = 17	N = 23	N = 28	N = 28	N = 26	N = 32	N = 39	N = 30
MgO(wt%)	17.80(3)	18.27(4)	18.47(3)	17.83(9)	18.38(7)	17.58(20)	17.79(4)	14.94(27)	17.51(12)	18.03(4)	19.05(7)	18.01(15)	17.35(21)
SiO ₂	62.11(19)	60.70(14)	63.98(13)	62.57(15)	64.62(19)	65.83(17)	63.03(9)	63.90(13)	65.06(23)	64.83(7)	63.79(11)	63.57(5)	64.01(34)
Al ₂ O ₃	7.90(2)	7.98(2)	7.92(2)	8.55(4)	7.71(3)	7.50(5)	7.56(2)	9.47(8)	7.83(3)	8.20(1)	8.16(2)	8.98(4)	8.03(5)
CaO	8.54(3)	8.85(1)	8.73(1)	9.85(7)	8.27(5)	8.05(4)	7.91(2)	10.37(14)	8.36(3)	8.77(1)	9.08(3)	9.64(7)	8.48(6)
FeO	0.23(1)	0.23(1)	0.51(2)	0.64(3)	0.11(1)	0.26(2)	0.85(1)	0.43(2)	0.79(2)	0.16(1)	0.25(2)	0.37(2)	0.21(1)
K ₂ O	b.d.l.	b.d.l.	b.d.l.	b.d.l.	b.d.l.	0.101(3)	0.31(1)	0.23(1)	b.d.l.	b.d.l.	b.d.l.	b.d.l.	0.04(1)
Na ₂ O	0.27(1)	0.087(4)	0.067(4)	0.14(1)	0.171(5)	0.28(1)	0.68(1)	0.51(2)	0.33(1)	0.13(1)	0.064(4)	0.053(3)	0.23(1)
MnO	0.27(1)	0.25(1)	0.27(1)	0.30(1)	0.27(1)	0.25(1)	0.45(1)	0.30(1)	0.07(1)	0.29(1)	0.33(1)	0.36(1)	0.46(1)
V ₂ O ₅	< 0.032(5)	< 0.03(1)	0.27(1)	0.09(1)	< 0.008	< 0.01(1)	0.17(1)	< 0.05(1)	< 0.06(1)	< 0.051(4)	< 0.06(1)	< 0.071(4)	b.d.l.

(continued on next page)

(continued on next page)

Table 2 (continued)

Run #	GGR3Si-1b	GGR3Si-2b	GGR3Si-3b	GGR3Si-4b	GGR6Si-1	GGR6Si-2	GGR6Si-3	GGR6Si-4	GGR6Si-1b	GGR6Si-2b	GGR6Si-3b	GGR6Si-4b	GGRFeSi1
EMPA	N = 34	N = 29	N = 24	N = 27	N = 27	N = 17	N = 23	N = 28	N = 28	N = 26	N = 32	N = 39	N = 30
Cr ₂ O ₃	0.069(4)	0.071(4)	0.14(1)	0.13(1)	0.07(1)	0.05(1)	0.39(1)	0.05(1)	0.25(1)	0.08(1)	0.11(1)	0.11(1)	0.08(1)
TiO ₂	0.212(4)	0.21(1)	0.24(1)	0.248(5)	0.19(1)	0.159(4)	0.25(1)	0.243(4)	0.081(4)	0.233(4)	0.256(4)	0.263(4)	0.24(1)
Total	97.50(16)	96.77(14)	100.42(13)	100.38(11)	99.87(23)	100.07(32)	99.40(7)	100.50(13)	100.36(11)	100.79(7)	101.18(12)	101.46(6)	99.13(10)

LA-ICP-MS	N = 10	N = 11	N = 9	N = 8	N = 6	N = 10	N = 6	N = 7	N = 2	N = 6	N = 10	N = 9	N = 8
	N (P) = 5	N (P) = 6	N (P) = 5	N (P) = 4	N (P) = 4	N (P) = 10	N (P) = 10	N (P) = 6	N (P) = 5	N (P) = 4	N (P) = 5	N (P) = 5	N = 8
CaO (wt%)	7.93(6)	8.06(6)	8.70(6)	8.96(41)	8.56(4)	8.32(9)	6.62(10)	9.72(12)	8.42(14)	8.66(10)	8.71(8)	9.31(32)	8.46(5)
P (ppm)	32(3)	17(2)	35(3)	25(3)	99(2)	25(2)	39(2)	101(13)	164(36)	27(2)	35(2)	30(3)	–
Ti	1296(14)	1245(13)	1522(7)	1433(78)	1313(7)	1093(25)	1301(26)	1426(10)	499(9)	1471(21)	1509(14)	1635(62)	1566(12)
V	130(2)	142(10)	276(2)	276(19)	82(2)	78(3)	933(29)	137(9)	246(10)	132(4)	138(4)	186(7)	62(1)
Cr	484(6)	514(15)	867(10)	751(20)	495(5)	349(5)	2273(32)	246(3)	1264(92)	132(4)	633(7)	775(32)	557(14)
Mn	1953(20)	1781(34)	2082(15)	2119(40)	2211(6)	1970(16)	2805(60)	2198(57)	449(8)	2321(18)	2446(22)	2783(36)	3448(39)
Fe	1651(22)	1523(26)	3074(72)	2660(454)	750(10)	881(218)	n.d.	n.d.	3401(276)	1146(71)	1356(32)	n.d.	1639(59)
Ni	b.d.l.	b.d.l.	b.d.l.	b.d.l.	b.d.l.	2.4(12)	3.3(2)	b.d.l.	8.7(8)	2.8(10)	2.4(11)	4.9(18)	–
Cu	1.0(1)	4.3(6)	2.5(1)	7.1(5)	3.4(1)	10(1)	22(1)	2.1(7)	8.7(1)	2.1(2)	3.8(6)	4.1(6)	5.0(2)
Zn	15(1)	21(2)	31.9(4)	194(19)	n.d.	n.d.	n.d.	n.d.	6.2(4)	32(1)	21(1)	107(2)	13.1(5)
Ga	0.62(4)	0.59(4)	1.06(5)	1.0(1)	n.d.	n.d.	n.d.	n.d.	0.6(1)	0.59(4)	0.72(4)	0.8(1)	0.71(3)
Ge	b.d.l.	1.9(1)	2.7(4)	b.d.l.	1.5(1)	1.4(1)	5.1(3)	b.d.l.	8.8(6)	1.85(3)	2.0(1)	b.d.l.	–
Mo	0.64(6)	0.20(1)	0.2(1)	b.d.l.	0.5(1)	0.29(3)	0.3(1)	b.d.l.	3.2(2)	0.32(2)	0.4(1)	0.4(1)	–
In	0.38(3)	0.38(2)	0.61(2)	0.47(4)	0.43(2)	0.38(1)	0.9(1)	0.38(1)	0.19(4)	0.42(3)	0.40(2)	0.40(5)	0.38(2)
Sn	73.0(6)	70(5)	129(1)	93(7)	68(1)	77(1)	228(16)	65(7)	35(4)	80(2)	78(1)	76(3)	72(4)
W	0.32(5)	0.10(1)	0.045(4)	0.09(1)	0.20(2)	0.07(1)	0.14(4)	0.07(4)	25(2)	0.16(3)	0.12(2)	0.06(2)	0.14(3)
Pt	0.16(2)	0.09(1)	0.045(4)	9.3(53)	0.07(1)	b.d.l.	b.d.l.	b.d.l.	0.6(2)	0.3(1)	0.12(2)	0.3(1)	0.37(4)
Pb	0.82(3)	2.0(2)	1.78(3)	5.2(4)	0.83(2)	0.89(3)	2.2(1)	0.72(2)	0.64(5)	1.47(5)	1.22(2)	4.62(5)	1.53(2)

Run #	GGRFeSi2	GGRFeSi3	GGRFeSi4	GGRFeSi5	GGRFeSi6	GGRFeSi7	GGRFeSi8	KBR3Si	KBR6Si	KBR1Si
EMPA	N = 49	N = 28	N = 22	N = 39	N = 25	N = 25	N = 25	N = 20	N = 31	N = 25
MgO (wt%)	16.38(47)	17.59(6)	12.53(20)	18.12(2)	15.75(5)	16.87(12)	17.67(4)	9.79(31)	10.77(2)	11.96(3)
SiO ₂	59.51(18)	59.83(16)	57.04(8)	63.05(10)	62.66(9)	59.41(24)	60.91(6)	65.90(79)	58.39(12)	48.48(7)
Al ₂ O ₃	7.68(29)	8.24(5)	9.82(4)	8.12(2)	7.69(2)	7.98(3)	8.01(2)	6.63(14)	7.92(3)	7.75(2)
CaO	8.07(12)	8.87(2)	10.54(6)	8.49(2)	8.11(2)	8.46(5)	8.62(2)	8.71(28)	11.64(4)	10.74(2)
FeO	3.44(4)	2.57(2)	6.24(5)	0.60(1)	2.44(2)	3.13(6)	1.37(5)	0.34(3)	0.17(1)	10.42(5)
K ₂ O	< 0.05(1)	< 0.04(1)	< 0.046(2)	< 0.013(2)	< 0.030(2)	< 0.029(2)	< 0.023(2)	1.79(5)	1.984(5)	1.69(1)
Na ₂ O	0.10(1)	0.09(1)	0.11(1)	< 0.055(3)	0.077(4)	0.097(5)	0.125(4)	2.16(2)	2.92(2)	2.78(1)
MnO	0.53(1)	0.48(1)	0.73(1)	0.45(1)	0.39(1)	0.33(1)	0.42(1)	0.13(1)	0.09(1)	0.05(1)
V ₂ O ₃	0.025(4)	0.010(4)	b.d.l.	b.d.l.	0.019(4)	b.d.l.	0.03(1)	b.d.l.	0.05(1)	0.96(1)
Cr ₂ O ₃	0.52(1)	0.51(1)	0.76(2)	0.25(1)	0.38(1)	0.49(1)	0.35(1)	0.08(1)	0.030(5)	0.78(1)
TiO ₂	0.223(5)	0.26(1)	0.30(1)	0.254(5)	0.25(1)	0.24(1)	0.26(1)	2.24(8)	2.18(2)	3.18(1)
P ₂ O ₅	–	–	–	–	–	–	–	–	–	0.26(1)
SnO ₂	–	–	–	–	–	–	–	–	–	0.08(1)
Total	96.62(17)	98.50(9)	98.12(17)	99.42(11)	97.81(9)	97.05(8)	97.89(11)	97.78(16)	96.17(14)	97.12(7)

LA-ICP-MS	N = 8	N = 3	N = 3	N = 7	N = 9	N = 8	N = 8	N = 4	N = 8	N = 5	N = 6
	N (P) = 8	N (P) = 3	N (P) = 3	N (P) = 10	N (P) = 10	N (P) = 10	N (P) = 10	N (P) = 8	N (P) = 8	N (P) = 5	N (P) = 5
CaO (wt%)	7.46(3)	8.54(7)	10.02(9)	8.53(4)	8.42(4)	8.36(3)	9.85(36)	10.47(7)	11.11(4)	13.82(18)	20.823(63)
P (ppm)	–	–	–	75(2)	83(2)	75(1)	109(4)	21(2)	1382(18)	–	–
Ti	1416(8)	1634(10)	1852(24)	1699(11)	1594(8)	1618(8)	15,965(922)	12,431(83)	–	–	–

(continued on next page)

(continued on next page)

Table 2 (continued)

LA-ICP-MS	N = 8	N = 3	N = 3	N = 7	N = 9	N = 7	N = 10	N = 8	N = 4	N = 8	N = 5	N = 6
				N (P) = 10	N (P) = 10	N (P) = 10	N (P) = 10	N (P) = 10	N (P) = 8	N (P) = 8	N (P) = 5	N (P) = 5
V	256(2)	190(5)	144(6)	94(1)	203(1)	155(4)	283(1)	283(1)	403(47)	76(1)	8272(46)	8272(46)
Cr	3429(25)	3527(37)	4463(118)	1727(11)	2786(18)	3322(41)	2482(10)	2482(10)	538(11)	229(5)	5433(12)	5433(12)
Mn	4144(30)	3796(27)	4530(82)	3551(14)	3102(16)	2565(28)	3278(20)	3278(20)	987(38)	653(4)	367(1)	367(1)
Fe	27,194(235)	21,505(1123)	54,742(3090)	4697(47)	-	-	-	-	2663(328)	824(68)	n.d.	n.d.
Ni	-	-	-	1.2(7)	< 1.6	b.d.l.	b.d.l.	b.d.l.	3.7(4)	b.d.l.	4.3(5)	4.3(5)
Cu	15(1)	20(1)	16(2)	0.43(4)	0.70(7)	16(2)	2.4(1)	2.4(1)	26(2)	1.3(1)	21.4(4)	21.4(4)
Zn	164(4)	101(2)	84(1)	82(2)	46(1)	4722(167)	753(5)	753(5)	n.d.	n.d.	n.d.	n.d.
Ga	1.57(2)	1.4(1)	3.4(2)	0.79(1)	1.19(3)	1.4(1)	0.85(2)	0.85(2)	n.d.	n.d.	n.d.	n.d.
Ge	-	-	-	1.7(2)	4.8(6)	7.4(3)	1.5(1)	1.5(1)	b.d.l.	2.3(6)	52(1)	52(1)
Mo	-	-	-	0.11(2)	0.11(1)	0.11(2)	0.10(2)	0.10(2)	0.4(1)	0.22(4)	2.0(1)	2.0(1)
In	2.40(3)	1.84(4)	1.61(5)	0.26(1)	0.41(1)	0.83(2)	0.244(4)	0.244(4)	0.30(3)	0.74(2)	5.2(1)	5.2(1)
Sn	502(5)	225(2)	284(5)	-	-	-	-	-	41(3)	43(2)	1232(5)	1232(5)
W	0.29(2)	0.14(3)	3.3(2)	-	-	-	-	-	0.4(1)	0.13(3)	122(1)	122(1)
Pt	0.11(2)	b.d.l.	b.d.l.	b.d.l.	0.97(8)	3.4(16)	0.15(4)	0.15(4)	b.d.l.	0.07(2)	0.03(1)	0.03(1)
Pb	16.0(2)	9.9(1)	6.8(3)	6.6(1)	5.5(1)	390(14)	49.2(3)	49.2(3)	0.44(3)	6.5(10)	4.8(1)	4.8(1)

^a Number of analyses ^b Values in parentheses are two standard errors for EMPA and LA-ICP-MS in terms of least digits cited ^c b.d.l. = below detection limit ^d n.d. = not determined ^e Number of analyses for P measurements only.

Taking the logarithm of the equilibrium constant K_{app} of Eq. (3) results in Eq. (4):

$$\log K_{app} = \log \frac{(x_{FeO}^{silicate})^{n/2} \cdot (x_M^{metal})}{(x_{MO_{n/2}}^{silicate}) \cdot (x_{Fe}^{metal})^{n/2}} + \log \frac{(\gamma_M^{metal})}{(\gamma_{Fe}^{metal})^{n/2}} + \log \frac{(\gamma_{FeO}^{silicate})^{n/2}}{(\gamma_{MO_{n/2}}^{silicate})} \quad (4)$$

where the first term on the right-hand side is the exchange coefficient or K_M^D . The second and third terms relate to the activity coefficients of M ($O_{n/2}$) and Fe(O).

The online metal activity calculator (described in Wade and Wood, 2005) was used to calculate the activities of Fe and other elements in the metallic liquids. The effects of Si on metal-silicate partitioning of siderophile elements were studied by rearranging the exchange coefficient K_M^D to Eq. (5):

$$\ln K_M^D = \text{const} + \frac{n}{2} \ln \gamma_{Fe}^{metal} - \ln \gamma_M^{metal} \quad (5)$$

where $\ln \gamma_{Fe}^{metal}$ and $\ln \gamma_M^{metal}$ are the activity coefficients of Fe and M in the Si-bearing alloy (Eqs. 6,7):

$$\ln \gamma_{Fe}^{metal} = \epsilon_{Si}^{Fe} (x_{Si}^{metal} + \ln(1 - x_{Si}^{metal})) \quad (6)$$

$$\ln \gamma_M^{metal} = \ln \gamma_{Fe}^{metal} + \ln \gamma_M^0 - \epsilon_M^{Si} \ln(1 - x_{Si}^{metal}) \quad (7)$$

where x_{Si}^{metal} is the mole fraction of Si in the metal, γ_M^0 is the activity coefficient of M infinitely dilute in liquid Fe and ϵ_M^{Si} is the interaction parameter between Si and element M (Wood et al., 2014). Substituting for γ_M^{metal} using Eq. (7) and rearranging yields Eq. (8) (Richter et al., 2018):

$$\ln K_M^D - \left(\frac{n}{2} - 1 \right) \ln \gamma_{Fe}^{metal} = \text{const} - \ln \gamma_M^0 + \epsilon_M^{Si} \ln(1 - x_{Si}^{metal}) \quad (8)$$

The K_M^D values were calculated as the ratio between the molar metal-silicate partition coefficient of element M and Fe or $K_M^D = D_M^* / (D_{Fe}^*)^{n/2}$ (Eqs. 2 and 4) (Wood et al., 2014 and references therein). The latter equations are based on the assumption that $\gamma_{FeO}^{silicate}$ is constant across the wide range of fO_2 considered here. We will later show in Section 3.2 that $\gamma_{FeO}^{silicate}$ is significantly decreased at highly reducing, C-saturated conditions. This variability in $\gamma_{FeO}^{silicate}$ was taken into account in the calculations of D_{Fe}^* (Eq. 2) and therefore $\ln K_M^D$ (Eq. (4)). Parameter $\gamma_{FeO}^{silicate}$ was assumed to be unity for mildly to moderately reduced experiments performed in graphite capsules (GGR1, GGR3Si, KBR1Si, KBR3Si runs) and all experiments performed in MgO capsules (Table 1). This assumption is justified given the strong correlation of the iron-wüstite (ΔIW) and the Si-SiO₂ buffers for these experiments (Rose-Weston et al., 2009; Table 1). For the most reducing experiments (i.e. the runs with lowest log Si-SiO₂ values; GGR6Si, GGRFeSi, KBR6Si; Table 1, Section 3.2), $\gamma_{FeO}^{silicate}$ was calculated using the offset between the iron-wüstite and Si-SiO₂ buffer. Note that in the calculations of interaction coefficients the interaction of trace element M with other elements within the metallic alloy were not taken into account while using the online metal activity calculator. However, consideration of the $\ln \gamma_M^{metal}$ term for non-divalent elements does take these interactions into account via their effects on $\ln \gamma_{Fe}^{metal}$ (Eq. (7)).

Most elements considered here are expected to exist in a 2+ valence state in the silicate melt. In this case, no correction for $\ln \gamma_{Fe}^{metal}$ is required, and the slope of plots of $\ln K_M^D$ versus $\ln(1 - x_{Si}^{metal})$ directly yields ϵ_M^{Si} (Eq. 8). It should be noted that this is only valid under the assumption that the other elements in the metal do not significantly affect the activity of either M or Si. However, for lower or higher valence elements the effects of different $\ln \gamma_{Fe}^{metal}$ with Si must be taken into account. In the calculations above the following valence states were assumed as discussed in Section 3.2: Cu¹⁺, Cr²⁺, Mn²⁺, Ni²⁺, Zn²⁺, Ge²⁺, Cd²⁺, Sn²⁺, Pb²⁺, V³⁺, Ga³⁺, In³⁺, Sb³⁺, Si⁴⁺, Ti⁴⁺, Mo⁴⁺, P⁵⁺, As⁵⁺, W⁶⁺.

Table 3
Silicate melt major and minor element composition of silicate melts of LG-GG-PR series (carbon-free experiments).

Run #	LG1Si-1	LG1Si-2	LG1Si-3	LG1Si-4	LG1Si-5	GG1Si-1	GG1Si-2	GG1Si-3	GG3Si-1	GG3Si-2	GG3Si-3	GG6Si-1
EPMA (wt%)	N = 56 ^a	N = 39	N = 45	N = 30	N = 30	N = 28	N = 26	N = 20	N = 30	N = 31	N = 24	N = 28
MgO	22.79(15) ^b	21.60(2)	26.35(5)	21.29(24)	9.10(26)	24.53(341)	27.92(287)	23.43(171)	33.19(181)	25.63(56)	18.93(120)	31.69(82)
SiO ₂	52.77(8)	54.96(5)	54.68(5)	55.59(18)	63.53(31)	40.73(21)	47.93(88)	49.03(31)	51.66(68)	53.79(36)	60.97(35)	52.04(24)
Al ₂ O ₃	9.47(4)	9.99(2)	8.56(2)	9.24(4)	10.64(3)	8.08(103)	6.24(61)	8.01(17)	6.22(38)	8.54(19)	8.45(43)	7.53(15)
CaO	1.18(14)	1.32(1)	1.07(1)	1.10(3)	1.20(3)	9.44(140)	7.07(88)	9.85(26)	7.16(58)	10.01(20)	9.09(38)	8.05(30)
FeO	5.18(3)	3.27(9)	1.94(2)	5.26(15)	6.44(21)	15.44(50)	9.74(13)	8.14(21)	1.19(5)	1.05(4)	1.49(9)	0.34(1)
K ₂ O	6.11(6)	6.57(1)	5.20(5)	5.81(12)	6.71(11)	< 0.04(1)	< 0.038(5)	< 0.045(3)	b.d.l.	b.d.l.	< 0.041(3)	b.d.l.
Na ₂ O	0.532(5)	0.55(1)	0.46(1)	0.51(2)	0.55(1)	< 0.03(1)	b.d.l.	< 0.034(5)	b.d.l.	< 0.041(4)	< 0.05(1)	b.d.l.
MnO	0.058(4)	0.059(4)	0.089(4)	0.072(4)	0.06(1)	0.20(1)	0.22(1)	0.26(1)	0.27(1)	0.37(1)	0.37(1)	0.28(1)
Cr ₂ O ₃	b.d.l.	b.d.l.	b.d.l.	b.d.l.	b.d.l.	0.28(1)	0.25(1)	0.27(1)	0.11(1)	0.074(5)	0.15(1)	0.11(1)
TiO ₂	0.263(3)	0.235(4)	0.235(4)	0.243(4)	0.29(1)	0.25(4)	0.19(2)	0.26(1)	0.19(2)	0.244(4)	0.26(1)	0.22(1)
SeO ₂	0.06(1)	0.04(1)	0.08(1)	< 0.03(1)	< 0.02(1)	0.11(2)	b.d.l.	0.02(1)	0.16(2)	0.07(1)	0.02(1)	0.31(1)
CaO	0.05(1)	< 0.03(1)	< 0.03(1)	0.12(1)	0.13(1)	0.33(5)	0.24(3)	0.25(2)	< 0.02(1)	< 0.03(1)	0.05(1)	0.06(4)
In ₂ O ₃	0.18(1)	0.14(1)	0.085(4)	0.11(1)	0.32(2)	0.05(1)	< 0.03(1)	< 0.03(1)	< 0.03(1)	< 0.03(1)	0.04(1)	< 0.03(1)
TeO ₂	b.d.l.	< 0.02(1)	< 0.02(1)	< 0.02(1)	< 0.01(1)	< 0.01(1)	b.d.l.	< 0.01(1)	< 0.02(1)	b.d.l.	b.d.l.	0.04(1)
PbO	0.09(1)	0.07(1)	< 0.03(1)	0.08(1)	0.16(1)	0.05(1)	< 0.03(1)	0.04(2)	< 0.02(1)	< 0.02(1)	< 0.02(1)	< 0.01(1)
Total	98.76(5)	98.89(7)	98.85(10)	99.50(10)	99.18(11)	99.62(32)	100.08(35)	99.73(14)	100.32(18)	99.99(40)	99.98(16)	100.75(19)

LA-ICP-MS	N = 15	N = 13	N = 8	N = 13	N = 10	N = 12	N = 10	N = 10	N = 4	N = 11	N = 2	N = 10
CaO (wt%)	1.10(2)	1.35(2)	1.06(1)	1.05(2)	1.00(3)	8.82(22)	7.11(10)	9.16(36)	6.55(18)	9.41(24)	5.62(15)	7.81(3)
Ti (ppm)	1584(18)	1636(20)	1491(11)	1437(53)	1521(31)	1504(34)	1226(14)	1565(54)	1123(32)	1473(33)	1124(58)	1420(6)
V	5.9(1)	5.1(1)	5.2(2)	6.4(2)	5.1(2)	10.7(1)	8.6(1)	10.2(1)	3.8(1)	2.9(1)	6.0(3)	2.10(3)
Cr	60(1)	61(1)	54(1)	87(2)	74(3)	1880(15)	1616(10)	1743(37)	750(14)	541(9)	1573(82)	769(3)
Mn	391(6)	456(3)	686(5)	502(7)	347(15)	1478(12)	1596(10)	1914(26)	2059(30)	2915(43)	2619(5)	2179(8)
Ni	13(1)	6(3)	4.4(2)	14(1)	24(2)	42(2)	22(1)	11.3(5)	3.0(5)	5.8(6)	9.3(19)	2.4(9)
Cu	1.3(1)	1.3(1)	0.8(1)	1.2(2)	b.d.l. ^c	5.9(3)	2.1(1)	1.6(3)	0.9(1)	1.3(1)	b.d.l.	1.0(1)
As	0.6(1)	0.6(1)	0.4(1)	1.4(2)	6.1(4)	0.43(3)	b.d.l.	b.d.l.	1.8(8)	0.9(1)	2.4(13)	0.9(2)
Se	452(8)	483(16)	822(16)	302(23)	223(12)	1009(26)	193(3)	284(15)	1015(68)	642(28)	136(27)	1991(10)
Cd	560(13)	357(5)	416(7)	1153(60)	801(41)	3052(70)	2324(47)	2417(111)	202(9)	298(15)	422(7)	114(2)
In	1170(13)	888(23)	529(16)	588(32)	2556(66)	440(11)	223(2)	248(11)	178(3)	198(10)	139(3)	202(1)
Sn	0.15(1)	0.18(1)	b.d.l. ^c	0.12(1)	0.21(1)	0.15(1)	b.d.l.	0.23(13)	b.d.l.	0.17(1)	b.d.l.	b.d.l.
Sb	1.1(2)	0.7(1)	0.13(2)	2.1(3)	2.8(2)	2.2(3)	0.47(2)	0.6(2)	2.1(11)	2.2(3)	1.5(4)	0.3(1)
Te	80(2)	99(11)	122(2)	60(3)	59(2)	240(9)	37(1)	48(2)	182(6)	103(4)	12(2)	438(4)
Pb	717(14)	548(9)	204(2)	665(19)	1377(23)	446(12)	275(2)	338(15)	75(3)	102(5)	108(13)	37.2(2)

Run #	GG6Si-2	GG6Si-3	GG6Si-1b	GG6Si-2b	GG6Si-3b	GGFeSi-1	GGFeSi-2	GGFeSi-3	GGFeSi-1b	GGFeSi-2b	GGFeSi-3b	PR1451
EPMA(wt%)	N = 32	N = 26	N = 28	N = 26	N = 30	N = 30	N = 30	N = 31	N = 26	N = 25	N = 25	N = 66
MgO	20.91(18)	17.19(119)	27.50(5)	19.72(8)	17.35(22)	30.78(65)	28.50(54)	18.49(91)	32.54(184)	21.05(59)	17.30(35)	51.42(94)
SiO ₂	58.25(10)	60.97(38)	55.06(5)	60.94(5)	60.71(14)	52.26(21)	53.21(24)	57.72(16)	51.48(61)	57.17(10)	61.71(14)	39.27(44)
Al ₂ O ₃	8.60(8)	9.13(39)	7.06(2)	7.98(4)	9.08(9)	7.73(13)	7.76(12)	10.20(35)	6.90(40)	9.62(31)	9.12(13)	3.53(65)
CaO	9.91(8)	10.21(36)	8.04(2)	9.39(6)	10.54(10)	8.85(24)	9.04(17)	11.77(40)	7.74(68)	10.62(26)	10.79(11)	4.10(98)
FeO	0.61(1)	1.31(7)	0.31(2)	0.52(1)	0.92(5)	0.03(1)	0.13(1)	0.17(1)	0.05(1)	0.26(2)	0.18(1)	0.18(3)
Na ₂ O	< 0.033(4)	< 0.030(4)	< 0.029(3)	0.046(4)	0.040(4)	< 0.035(3)	< 0.030(4)	0.05(1)	< 0.026(4)	< 0.040(5)	< 0.041(4)	0.41(6)
K ₂ O	< 0.020(2)	< 0.025(2)	< 0.021(2)	< 0.027(2)	< 0.025(1)	< 0.032(3)	< 0.021(1)	0.036(2)	< 0.017(2)	< 0.028(2)	< 0.021(1)	b.d.l.
MnO	0.36(1)	0.33(1)	0.321(5)	0.42(1)	0.335(4)	0.25(1)	0.36(1)	0.43(1)	0.27(1)	0.37(1)	0.43(1)	0.08(1)
Cr ₂ O ₃	0.14(1)	0.23(1)	0.08(1)	0.11(1)	0.16(1)	< 0.010(3)	0.025(4)	0.03(1)	< 0.025(4)	0.07(1)	0.04(1)	< 0.010(3)
TiO ₂	0.266(5)	0.27(1)	0.221(4)	0.252(5)	0.274(4)	0.196(5)	0.28(1)	0.28(1)	0.20(1)	0.268(5)	0.261(5)	0.10(2)
SeO ₂	0.14(1)	0.03(1)	0.36(1)	0.17(1)	0.07(1)	0.79(2)	0.81(4)	0.55(3)	0.75(4)	0.37(3)	0.52(2)	0.90(19)
CdO	b.d.l.	0.05(1)	b.d.l.	< 0.02(1)	< 0.03(1)	b.d.l.	b.d.l.	b.d.l.	b.d.l.	< 0.02(1)	< 0.01(1)	< 0.01(1)

(continued on next page)

Table 3 (continued)

Run #	GG6Si-2	GG6Si-3	GG6Si-1b	GG6Si-2b	GG6Si-3b	GGFeSi-1	GGFeSi-2	GGFeSi-3	GGFeSi-1b	GGFeSi-2b	GGFeSi-3b	PR1451
EPMA (wt%)	N = 32	N = 26	N = 28	N = 26	N = 30	N = 30	N = 30	N = 30	N = 26	N = 25	N = 25	N = 66
In ₂ O ₃	0.04(1)	0.05(1)	< 0.03(1)	0.05(1)	0.06(1)	< 0.02(1)	< 0.02(1)	< 0.03(1)	< 0.04(1)	0.04(1)	0.05(1)	0.017(5)
TeO ₂	b.d.l.	b.d.l.	< 0.02(1)	b.d.l.	b.d.l.	0.13(1)	0.05(1)	b.d.l.	0.14(1)	< 0.02(1)	b.d.l.	0.32(7)
PbO	< 0.01(1)	< 0.02(1)	< 0.01(1)	< 0.02(1)	< 0.02(1)	< 0.01(1)	< 0.01(1)	< 0.02(1)	< 0.01(1)	b.d.l.	< 0.01(1)	0.04(1)
ZrO ₂	–	–	–	–	–	–	–	–	–	–	–	0.21(6)
Total	99.34(16)	99.89(22)	99.11(5)	99.71(5)	99.67(20)	101.17(13)	100.24(28)	99.86(10)	100.23(14)	100.00(9)	100.53(11)	99.89(48)
LA-ICP-MS	N = 11	N = 12	N = 1	N = 17	N = 13	N = 10	N = 15	N = 13	N = 14	N = 7	N = 10	N = 8
N (Fe) = 6 ^d	N (Fe) = 4	N (Fe) = 7	N (Fe) = 7	N (Fe) = 8	N (Fe) = 7	N (Fe) = 8	N (Fe) = 7	N (Fe) = 5	N (Fe) = 6	N (Fe) = 9	N (Fe) = 8	–
CaO (wt%)	9.59(1)	9.52(18)	7.89(26) ^e	9.12(8)	10.34(15)	8.41(8)	8.54(8)	10.09(36)	7.74(20)	9.67(28)	10.74(7)	3.87(39)
FeO	0.62(1)	1.40(14)	–	0.58(2)	0.82(7)	0.033(2)	0.13(1)	0.135(2)	0.063(3)	0.16(1)	0.156(3)	–
Ti (ppm)	1580(19)	1667(40)	1351(210)	1500(14)	1683(26)	1208(10)	1350(8)	1603(38)	1206(30)	1594(41)	1716(12)	674(101)
V	2.32(3)	3.9(2)	1.4(1)	2.00(5)	1.9(1)	0.29(2)	0.77(3)	0.79(4)	0.6(1)	1.03(4)	0.70(4)	1.22(24)
Cr	946(7)	1759(72)	612(34)	779(9)	1010(25)	105(1)	171(3)	216(4)	197(5)	434(17)	331(16)	98(11)
Mn	2717(10)	2488(14)	2156(92)	2903(21)	2403(16)	1884(8)	2614(21)	3129(28)	1914(25)	2620(36)	2980(13)	689(82)
Ni	4.5(7)	b.d.l.	6.6(6)	2.4(2)	2.9(17)	2.0(8)	b.d.l.	b.d.l.	1.9(10)	2.55(3)	b.d.l.	8.3(21)
Cu	0.8(1)	1.1(1)	0.7(1)	0.66(4)	0.91(5)	0.49(4)	1.1(1)	0.8(1)	0.49(3)	0.45(4)	0.74(4)	9.6(27)
Zn	–	–	12(1)	12.1(4)	21(1)	–	–	–	6.9(3)	8.4(5)	9.5(3)	2.1(4)
Ga	–	–	0.47(7)	0.43(3)	0.53(2)	–	–	–	0.42(2)	0.47(4)	0.51(2)	0.55(13)
As	0.6(1)	0.4(1)	15(1)	0.75(5)	0.9(1)	5.2(1)	0.49(3)	0.38(1)	1.6(2)	0.85(1)	0.54(3)	9.5(29)
Se	867(19)	324(20)	1643(908)	1079(29)	611(18)	3944(45)	4162(48)	2534(122)	3790(41)	1962(68)	2853(117)	4993(1007)
Zr	–	–	–	–	–	–	–	–	–	–	–	1303(239)
Cd	243(3)	547(14)	126(8)	238(5)	328(8)	42(1)	91(2)	123(5)	60(3)	123(11)	143(3)	139(28)
In	304(4)	338(10)	154(6)	261(4)	343(22)	208(2)	169(2)	211(11)	229(8)	176(9)	357(5)	114(24)
Sn	0.18(2)	0.29(3)	b.d.l.	0.08(1)	0.148(4)	0.16(7)	0.21(6)	0.15(6)	0.145(2)	b.d.l.	0.12(5)	0.103(4)
Sb	0.6(1)	0.28(4)	3.4(2)	0.7(1)	0.41(5)	2.7(5)	0.46(5)	0.12(1)	1.7(3)	1.4(3)	0.3(1)	7.7(20)
Te	119(3)	37(3)	285(25)	112(2)	71(2)	1104(11)	551(6)	207(9)	1365(84)	257(9)	246(8)	2518(557)
Pb	105(1)	215(22)	37(2)	83(2)	153(4)	6.4(4)	19.3(3)	17(1)	9.7(4)	23(2)	46(1)	32(6)
Run #	PR1453	PR1455	PR1457	PR1458	PR1459	PR1512	PR1513	PR1514	PR1515			
EPMA (wt%)	N = 91	N = 30	N = 47	N = 55	N = 56	N = 51	N = 32	N = 29	N = 16			
MgO	48.36(94)	45.70(260)	43.06(222)	44.51(191)	49.30(111)	44.52(134)	44.28(209)	42.61(246)	43.31(157)			
SiO ₂	39.21(33)	38.18(54)	43.59(38)	38.37(49)	38.36(52)	38.64(35)	38.35(58)	38.04(48)	38.63(44)			
Al ₂ O ₃	5.21(58)	6.98(113)	6.02(83)	6.58(87)	3.51(44)	7.84(85)	7.21(126)	8.21(118)	8.35(102)			
CaO	6.37(92)	8.61(185)	7.05(171)	8.31(207)	4.00(78)	8.53(85)	8.20(135)	9.86(167)	9.63(101)			
FeO	0.17(2)	0.52(6)	0.17(2)	0.35(3)	0.06(1)	0.17(3)	0.23(3)	0.54(6)	1.88(18)			
K ₂ O	< 0.029(4)	< 0.02(1)	< 0.015(4)	< 0.015(4)	< 0.012(3)	b.d.l.	b.d.l.	0.02(1)	n.d.			
Na ₂ O	0.05(1)	0.03(1)	< 0.026(5)	0.04(1)	< 0.02(1)	0.03(1)	0.04(1)	0.05(1)	n.d.			
MnO	0.09(1)	0.14(2)	0.15(1)	0.10(1)	0.030(4)	0.10(1)	0.10(1)	0.12(3)	n.d.			
Cr ₂ O ₃	< 0.014(3)	0.04(1)	< 0.013(3)	< 0.025(4)	b.d.l.	0.03(1)	< 0.015(4)	0.02(1)	0.08(2)			
TiO ₂	0.15(1)	0.22(4)	0.16(2)	0.19(3)	0.06(1)	0.22(2)	0.21(3)	0.24(4)	0.24(2)			
SeO ₂	1.06(14)	0.38(9)	0.90(15)	0.32(6)	0.81(14)	0.70(9)	0.99(18)	0.37(11)	0.15(2)			
CdO	< 0.010(4)	< 0.01(1)	b.d.l.	b.d.l.	< 0.01(1)	< 0.014(4)	< 0.012(4)	< 0.02(1)	b.d.l.			
In ₂ O ₃	0.03(1)	< 0.01(1)	0.03(1)	0.03(1)	0.03(1)	0.03(1)	< 0.012(4)	< 0.02(1)	0.13(1)			
TeO ₂	0.21(3)	< 0.01(1)	0.08(2)	0.02(1)	0.45(7)	0.05(2)	0.08(2)	b.d.l.	b.d.l.			
PbO	b.d.l.	< 0.03(1)	< 0.01(1)	< 0.01(1)	b.d.l.	< 0.02(1)	< 0.02(1)	< 0.03(1)	0.04(1)			
ZrO ₂	0.04(1)	0.07(2)	0.06(2)	0.97(23)	3.48(75)	0.03(1)	0.13(3)	0.22(5)	n.d.			
Total	101.00(26)	100.99(22)	101.37(21)	99.86(14)	100.14(20)	100.89(25)	99.90(23)	100.42(27)	102.55(25)			
LA-ICP-MS	N = 8	N = 12	N = 5	N = 10	N = 11	N = 9	N = 12	N = 10	N = 15			
N (Fe) = 8	N (Fe) = 12	N (Fe) = 5	N (Fe) = 10	N (Fe) = 11	N (Fe) = 9	N (Fe) = 12	N (Fe) = 10	N (Fe) = 15	N (Fe) = 15			
(continued on next page)												

Table 3 (continued)

LA-ICP-MS	N = 8	N = 12	N = 5	N = 10	N = 11	N = 9	N = 12	N = 10	N = 15
CaO (wt%)	6.41(54)	8.39(80)	5.86(56)	9.69(115)	5.73(50)	7.60(50)	8.41(56)	9.46(65)	9.61(49)
Ti (ppm)	1028(75)	1511(113)	935(82)	1340(121)	525(38)	1280(74)	1350(71)	1534(85)	1552(75)
V	2.34(12)	2.7(1)	0.95(17)	1.82(13)	0.90(15)	1.15(15)	0.75(10)	5.3(3)	7.9(3)
Cr	130(5)	312(14)	101(10)	195(11)	34(3)	159(6)	125(5)	180(8)	386(11)
Mn	713(28)	1110(56)	1119(84)	825(53)	278(15)	834(17)	783(37)	921(41)	1172(36)
Ni	4.9(5)	11(1)	24(2)	9.0(10)	4.1(5)	4.2(5)	7.5(10)	4.6(6)	22(1)
Cu	5.0(6)	0.92(12)	2.9(8)	3.7(3)	5.1(8)	1.24(16)	1.58(15)	1.18(14)	1.88(20)
Zn	5.4(4)	3.0(3)	2.4(5)	3.7(13)	3.2(8)	3.3(3)	2.50(22)	3.2(2)	4.5(3)
Ga	1.05(12)	1.54(17)	1.06(14)	2.47(35)	1.84(19)	0.95(7)	1.13(11)	2.01(17)	1.40(10)
As	5.6(1)	< 1.6	17(2)	b.d.l.	48(5)	2.20(43)	2.6(6)	< 1.4	< 1.4
Se	7444(456)	2236(207)	4464(622)	3003(356)	6509(589)	3833(164)	6254(434)	1985(179)	726(47)
Zr	221(17)	403(38)	359(40)	7742(811)	38,762(3421)	110(8)	770(53)	1374(103)	395(23)
Cd	160(10)	154(13)	129(12)	181(10)	95(6)	103(4)	133(7)	192(15)	964(36)
In	295(20)	71(8)	318(34)	351(25)	183(21)	96(3)	61(3)	67(7)	568(58)
Sn	0.21(6)	< 0.10	0.11(1)	0.19(2)	0.18(5)	0.12(1)	< 0.15	0.12(2)	0.14(3)
Sb	2.8(3)	0.79(24)	32(5)	0.39(5)	14(1)	2.7(2)	1.82(64)	0.11(1)	1.61(68)
Te	2064(108)	498(38)	1118(200)	592(58)	5409(505)	999(39)	1325(71)	299(26)	174(15)
Pb	49(4)	47(6)	95(17)	45(3)	25(1)	30(1)	33(1)	40(3)	457(36)

^a Number of analyses ^b Values in parentheses are two standard errors for EPMA and LA-ICP-MS in terms of least digits cited ^c b.d.l. = below detection limit ^d Number of analyses for Fe measurements only ^e 1 sigma error due to lack of analyses.

3. Results

3.1. Run products

Run products consisted of Fe-rich blobs embedded in quenched silicate glass (Fig. 1). In both C-free and C-saturated experiments silicate compositions showed a marked decrease of FeO compared to their initial abundances, reflecting reduction through addition of metallic Si (Tables 2, 3).

The silicate melts of experiments performed in graphite capsules usually quenched to a homogeneous glass with the exception of the runs performed in MgO capsules. Despite relatively short run durations, silicate melts in these experiments showed substantial enrichment of MgO due to reaction with the capsule walls. This reaction also resulted in the formation of magnesiowustite and forsterite crystals along the walls. Due to the increased MgO contents most silicate melts in these series quenched to a heterogeneous, spinifex-textured glass. The C-saturated Fe-rich alloys were generally homogenous and occasionally showed dendritic quenching textures (Tables 4, 5). The Fe-rich alloys of C-free experiments occasionally showed heterogeneous regions, in the case of run GG8Si-1 at the rim, which were characterized by substantial enrichments in trace elements Cd, Se, Te and Pb (e.g. Rose-Weston et al., 2009; Vogel et al., 2018). The smaller-sized quench textures which were homogeneously distributed within the Fe-rich alloy were taken into account by using a broad defocused beam and a large number of measurements (Section 2.2; Vogel et al., 2018). Given the unconstrained 3-D distribution of the rim quench textures in run GG8Si-1 we cannot explicitly account for its contribution to the overall bulk metal composition of this specific experiment. However, given the well-defined dependencies of exchange coefficients for C-free experiments as a function of Si contents it is unlikely it affects the results presented in this study.

3.2. Oxygen fugacity, FeO activity and valence states

The oxygen fugacity (f_{O_2}) can be defined relative to the iron-wüstite buffer (ΔIW):

$$\Delta IW = 2 \log \left(\frac{a_{FeO}^{silicate}}{a_{Fe}^{metal}} \right) = 2 \log \left(\frac{x_{FeO}^{silicate}}{x_{Fe}^{metal}} \right) + 2 \log \left(\frac{\gamma_{FeO}^{silicate}}{\gamma_{Fe}^{metal}} \right) \quad (9)$$

where $a_{FeO}^{silicate}$ and a_{Fe}^{metal} are the activities of FeO and Fe in the silicate and metallic melt, respectively. The activity coefficient of Fe in the metal (γ_{Fe}^{metal}) was calculated using the online metal activity calculator (Wade and Wood, 2005). The activity coefficient of FeO in the silicate melt ($\gamma_{FeO}^{silicate}$) was assumed to be unity, except for the highly reduced runs conducted in graphite capsules that clearly show evidence for non-idealities of $\gamma_{FeO}^{silicate}$ (see discussion below). These experiments yield apparent moderately reducing conditions based on FeO contents of the silicate melt, whereas the Si content of the metals implies much more reducing conditions. The most likely explanation for this discrepancy is that $\gamma_{FeO}^{silicate}$ significantly decreases at very reducing conditions, yielding artificially more oxidizing conditions (e.g. Rose-Weston et al., 2009; Wykes et al., 2015; Wohlers and Wood, 2017). Unfortunately, it is unclear how $\gamma_{FeO}^{silicate}$ varies with silicate melt composition at very low f_{O_2} . One approach to assess the variability of $\gamma_{FeO}^{silicate}$ (and therefore ΔIW) is to compare computed values of ΔIW with the f_{O_2} relative to the Si-SiO₂ buffer (Rose-Weston et al., 2009), which is defined as:

$$\log f_{O_2} (\Delta Si - SiO_2) = 2 \log \left(\frac{a_{SiO_2}^{silicate}}{a_{Si}^{metal}} \right) = 2 \log \left(\frac{x_{SiO_2}^{silicate}}{x_{Si}^{metal}} \right) + 2 \log \left(\frac{\gamma_{SiO_2}^{silicate}}{\gamma_{Si}^{metal}} \right) \quad (10)$$

where γ_{Si}^{metal} was calculated with the online metal activity calculator (Wade and Wood, 2005). One drawback of this method is that

Table 4
Major and minor element composition of metallic melts of GGR-KBR series (carbon-saturated experiments).

Run #	GGR1Si-1	GGR1Si-2	GGR1Si-3	GGR1Si-4	GGR1Si-5	GGR1Si-6	GGR1Si-4b	GGR1Si-5b	GGR1Si-6b	GGR3Si-1	GGR3Si-2	GGR3Si-3	GGR3Si-4
EMPA	N = 46 ^a	N = 40	N = 30	N = 26	N = 26	N = 27	N = 21	N = 25	N = 21	N = 43	N = 26	N = 29	N = 35
Fe (wt%)	72.36(36) ^b	82.23(18)	83.26(19)	79.97(11)	83.78(36)	83.03(17)	85.24(13)	84.83(25)	84.31(21)	78.02(10)	77.12(18)	77.72(37)	75.38(36)
P	1.02(6)	0.89(5)	0.82(6)	0.74(3)	0.68(7)	0.79(3)	1.00(4)	1.13(9)	1.08(7)	0.46(2)	1.01(3)	0.80(5)	0.60(1)
V	0.42(2)	0.77(4)	0.36(3)	0.075(5)	0.09(1)	0.14(1)	0.22(2)	0.12(1)	0.27(1)	1.26(3)	0.94(1)	0.35(3)	1.05(14)
Cr	0.52(1)	0.93(1)	0.62(1)	0.19(1)	0.22(1)	0.32(1)	0.42(1)	0.35(1)	0.52(1)	1.05(1)	1.08(1)	0.51(1)	0.92(1)
Mn	< 0.006	< 0.009	b.d.l. ^c	b.d.l.	b.d.l.	b.d.l.	b.d.l.	< 0.006	< 0.005	0.075(5)	0.088(5)	< 0.004	0.092(5)
Ni	1.57(2)	1.76(4)	1.90(4)	1.83(2)	1.85(9)	1.87(3)	1.81(2)	1.84(6)	1.73(2)	2.68(3)	2.74(3)	3.51(12)	2.91(2)
Cu	b.d.l.	0.76(4)	0.18(1)	0.01(1)	b.d.l.	0.64(3)	b.d.l.	b.d.l.	0.13(1)	1.07(2)	0.08(1)	0.09(2)	0.36(1)
Ge	1.80(3)	1.76(7)	1.90(8)	1.83(3)	2.19(20)	1.78(5)	1.76(4)	b.d.l.	1.92(6)	2.31(4)	2.66(3)	3.26(17)	2.88(3)
Mo	1.87(6)	1.70(3)	1.82(5)	2.18(3)	1.64(4)	1.75(3)	1.59(4)	1.90(4)	1.87(4)	2.47(5)	2.82(3)	3.39(7)	2.85(9)
Sn	1.47(5)	1.88(9)	1.67(10)	1.43(2)	1.51(14)	1.37(8)	1.54(6)	1.54(10)	1.82(6)	2.02(3)	2.50(14)	2.88(21)	2.02(5)
W	1.88(5)	1.74(3)	1.80(3)	1.89(2)	1.89(4)	1.85(2)	1.74(2)	1.78(2)	1.72(3)	1.91(3)	1.79(2)	2.25(6)	1.95(12)
Pt	9.47(65)	b.d.l.	b.d.l.	2.14(19)	b.d.l.	b.d.l.	b.d.l.	b.d.l.	b.d.l.	b.d.l.	b.d.l.	b.d.l.	b.d.l.
Si	b.d.l.	< 0.007	< 0.008	0.012(2)	0.015(2)	0.028(2)	0.03(2)	0.015(3)	< 0.008	1.77(2)	2.87(3)	0.018(2)	2.71(2)
Total	92.50(21)	94.44(11)	94.35(20)	92.29(17)	93.87(37)	93.57(19)	95.36(13)	95.28(25)	95.38(18)	95.11(15)	95.70(13)	94.78(18)	93.73(12)
Fe (wt%)	n.d. ^d	n.d.	N = 12	N = 15	N = 16	N = 11	n.d.	n.d.	n.d.	N = 20	N = 18	N = 27	N = 20
Ni	-	-	85.81(72)	81.45(36)	85.56(40)	87.52(57)	-	-	-	78.01(157) ^g	77.91(67)	81.38(61)	75.83(43)
Si	-	-	1.83(5)	1.79(3)	1.75(3)	1.82(3)	-	-	-	2.00(4)	2.68(5)	2.43(5)	2.87(2)
C	-	-	0.007(2)	0.003(2)	0.005(1)	0.008(1)	-	-	-	1.24(7)	2.72(4)	0.0057(9)	2.62(3)
Total	-	-	4.59(7)	4.43(7)	4.72(7)	4.83(8)	-	-	-	4.50(10)	3.66(8)	4.80(9)	3.60(5)
Total	-	-	101.05(66)	98.07(37)	100.17(38)	102.85(55)	-	-	-	98.31(162)	99.93(67)	102.14(61)	97.84(43)

LA-ICP-MS	N = 10	N = 9	N = 5	N = 8	N = 7	N = 12	N = 6	N = 5	N = 7	N = 7	N = 10	N = 10	N = 9
Si (wt%)	b.d.l.	b.d.l.	b.d.l.	b.d.l.	b.d.l.	b.d.l.	0.17(2)	b.d.l.	b.d.l.	b.d.l.	2.84(3)	b.d.l.	2.64(4)
Ti (ppm)	b.d.l.	b.d.l.	b.d.l.	27(1)	b.d.l.	20(3)	25(5)	b.d.l.	b.d.l.	b.d.l.	156(3)	44(17)	79(4)
Ti _{corr}	b.d.l.	b.d.l.	b.d.l.	39(2)	b.d.l.	29(4)	36(7)	b.d.l.	b.d.l.	b.d.l.	225(4)	63(25)	114(6)
V	2553(271)	4653(205)	3502(1106)	667(51)	597(31)	848(40)	1697(75)	679(32)	1995(74)	10,052(181)	7627(60)	3158(199)	6588(139)
V _{corr}	3549(377)	6468(285)	4868(1537)	927(71)	830(44)	1179(56)	2357(104)	944(45)	2773(103)	13,972(252)	10,602(84)	4390(23)	9157(66)
Cr	2913(97)	5689(78)	4245(189)	1602(43)	1529(51)	2253(84)	3158(153)	2210(75)	3849(106)	11,809(247)	9510(42)	4786(389)	7423(57)
Mn	11(1)	35(1)	8.7(10)	6.2(8)	5.4(3)	7.6(8)	16(1)	9.4(26)	14(1)	908(11)	871(5)	17(2)	879(8)
Ni	Int. ^e	Int.	Int.	Int.	Int.	Int.	Int.	Int.	Int.	Int.	Int.	Int.	Int.
Cu	273(5)	9493(118)	3001(50)	645(8)	193(4)	7364(256)	761(23)	615(9)	1993(85)	20,066(1330)	1650(7)	1724(120)	4564(403)
Cu _{corr} ^f	177(3)	6170(77)	1951(33)	419(5)	125(2)	4787(166)	495(15)	400(6)	1295(55)	13,043(865)	1073(5)	1121(78)	2967(262)
Zn	n.d.	n.d.	19(1)	n.d.	n.d.	n.d.	141(7)	103(6)	171(4)	n.d.	n.d.	n.d.	n.d.
Zn _{corr}	-	-	4.5(3)	-	-	-	34(2)	25(1)	41(1)	-	-	-	-
Ga	n.d.	n.d.	2.8(3)	n.d.	n.d.	n.d.	3.5(2)	3.14(1)	4.8(10)	n.d.	n.d.	n.d.	n.d.
Ga _{corr}	-	-	2.1(3)	-	-	-	2.7(2)	2.41(1)	3.7(10)	-	-	-	-
Ge	14,476(118)	13,871(108)	16,124(102)	15,453(48)	17,365(68)	12,710(575)	15,792(91)	16,028(131)	17,366(167)	26,947(404)	22,986(50)	29,064(201)	24,996(141)
Mo	8603(282)	9343(123)	9297(383)	10,312(383)	9298(453)	9126(578)	10,910(1124)	9236(279)	11,238(634)	19,655(725)	17,181(315)	20,429(653)	15,061(159)
Mo _{corr}	13,593(446)	14,762(194)	14,689(605)	16,293(605)	14,691(716)	14,419(913)	17,238(1776)	14,593(441)	17,756(1002)	31,055(1146)	27,146(498)	32,278(1032)	23,796(251)
In	67(1)	80(2)	85(3)	65(1)	65(1)	53(1)	63(3)	68(1)	75(1)	134(5)	134(2)	149(8)	102(3)
In _{corr}	33(1)	39(1)	42(2)	32(1)	32(10)	26(1)	31(2)	34(1)	37(1)	66(3)	66(1)	73(5)	50(2)
Sn	18,245(334)	21,454(359)	23,026(716)	18,101(348)	17,632(233)	14,679(335)	17,193(698)	18,643(171)	207,633(340)	35,833(1460)	32,800(418)	40,813(2335)	25,671(1037)
Sn _{corr}	13,319(244)	15,661(262)	16,809(523)	13,214(254)	12,871(170)	10,716(245)	12,551(510)	13,609(125)	15,157(248)	26,158(1066)	29,793(1705)	18,740(757)	18,740(757)
W	7742(290)	8546(150)	7284(364)	7514(392)	9028(614)	7126(1056)	9887(937)	6581(273)	9245(608)	15,857(635)	9705(229)	13,061(835)	8208(279)
W _{corr}	13,703(513)	15,126(266)	12,893(644)	13,300(694)	15,980(1087)	12,613(1869)	17,500(1658)	11,648(483)	16,364(1076)	28,067(1124)	17,178(404)	23,118(1478)	14,530(493)
Pt	78,941(3767)	6.2(2)	51(42)	31,624(642)	49(16)	102(36)	460(285)	18.9(3)	20(1)	4336(2496)	10.6(5)	36(6)	12,121(3019)
Pb	3.0(1)	5.4(2)	3.7(3)	1.6(1)	2.2(4)	1.9(1)	14(1)	8.9(2)	8.8(6)	8.0(9)	14(1)	4.6(3)	8.2(9)
Pb _{corr}	1.06(5)	1.90(8)	1.31(10)	0.58(3)	0.78(15)	0.65(23)	4.8(2)	3.1(1)	3.1(2)	2.8(3)	5.0(3)	1.61(1)	2.9(3)

(continued on next page)

Table 4 (continued)

Run #	GGR3Si-1b	GGR3Si-2b	GGR3Si-3b	GGR3Si-4b	GGR6Si-1	GGR6Si-2	GGR6Si-3 Si-rich	GGR6Si-3 Si-poor	GGR6Si-4	GGR6Si-1b	GGR6Si-2b	GGR6Si-3b	GGR6Si-4b
EMPA	N = 42	N = 74	N = 25	N = 49	N = 29	N = 30	N = 14	N = 17	N = 22	N = 27	N = 29	N = 31	N = 34
Fe (wt%)	75.82(36)	77.35(9)	78.31(28)	77.87(37)	70.03(83)	70.75(70)	75.66(50)	70.61(67)	72.94(35)	47.04(73)	72.51(47)	73.10(20)	72.47(25)
P	0.95(5)	0.84(1)	1.15(7)	1.15(5)	1.09(26)	0.81(6)	0.69(6)	0.85(5)	0.93(1)	0.62(7)	1.17(2)	1.08(4)	1.12(4)
V	0.92(4)	0.83(1)	0.88(1)	1.03(3)	0.90(5)	0.88(15)	0.79(10)	1.04(20)	0.88(6)	0.88(30)	0.88(2)	0.93(2)	0.69(6)
Cr	1.04(4)	1.04(1)	1.25(2)	1.08(1)	1.29(6)	1.12(4)	1.00(5)	1.42(5)	1.10(2)	0.34(4)	1.27(1)	1.47(1)	1.30(2)
Mn	0.088(5)	0.081(3)	0.06(1)	0.065(4)	0.17(1)	0.17(1)	0.03(1)	0.03(1)	0.18(1)	0.123(5)	0.123(5)	0.116(5)	0.116(5)
Ni	2.49(3)	2.82(1)	2.71(4)	2.59(8)	4.31(6)	4.28(6)	3.74(4)	4.79(18)	3.52(3)	2.47(9)	3.67(3)	3.66(3)	3.84(8)
Cu	b.d.l.	0.11(1)	b.d.l.	0.09(2)	0.59(3)	0.90(11)	0.55(3)	0.17(2)	0.31(2)	0.004(4)	0.11(3)	0.23(1)	0.26(1)
Ge	2.24(5)	2.28(2)	2.54(6)	2.32(5)	4.00(8)	2.13(5)	2.13(5)	4.36(20)	2.74(3)	2.08(5)	3.07(3)	2.90(5)	2.99(6)
Mo	2.46(9)	2.48(2)	2.70(12)	2.63(8)	3.77(30)	3.31(18)	2.94(18)	4.62(23)	4.02(9)	3.99(62)	3.54(3)	3.07(4)	3.42(8)
Sn	2.33(10)	2.43(6)	2.89(22)	2.68(11)	3.17(14)	3.09(44)	2.55(19)	4.26(20)	2.71(5)	1.58(20)	3.08(7)	3.52(13)	3.45(9)
W	1.92(6)	2.09(1)	1.94(7)	1.88(3)	2.13(33)	1.79(17)	1.21(8)	2.07(19)	2.05(9)	2.12(51)	1.70(3)	1.66(3)	1.66(7)
Pt	0.84(29)	b.d.l.	b.d.l.	b.d.l.	b.d.l.	b.d.l.	b.d.l.	b.d.l.	b.d.l.	31.57(47)	b.d.l.	b.d.l.	b.d.l.
Si	2.49(3)	2.88(2)	1.58(4)	1.58(11)	6.03(15)	7.23(24)	6.48(22)	0.14(1)	5.37(3)	4.32(15)	5.48(26)	5.37(5)	6.86(3)
Total	93.59(25)	95.24(8)	95.99(13)	94.97(14)	97.50(17)	97.57(22)	97.78(24)	94.36(44)	96.76(28)	97.04(23)	96.60(18)	97.13(18)	98.18(10)
Fe (wt%)	N = 7	N = 19	N = 4	N = 7	N = 15	N = 10	N = 5	N = 6	N = 15	N = 8	N = 13	N = 6	N = 8
Ni	78.59(39)	77.77(32)	78.72(96)	77.60(14)	70.37(89)	70.85(109)	77.44(131)	74.73(56)	71.37(41)	50.82(150)	72.30(39)	74.55(51)	73.17(79)
Si	2.32(1)	2.74(8)	2.33(5)	2.65(5)	4.06(13)	4.09(7)	3.67(4)	4.43(9)	3.52(3)	2.73(10)	3.58(3)	3.56(4)	3.66(7)
C	2.44(3)	2.79(9)	1.68(2)	1.95(6)	5.93(27)	6.76(27)	6.40(14)	0.11(1)	5.59(19)	4.75(20)	5.75(4)	5.16(7)	6.53(5)
Total	4.10(11)	4.28(13)	4.61(8)	4.84(17)	2.60(16)	2.44(19)	1.71(18)	4.33(8)	2.49(6)	1.35(22)	2.50(3)	3.13(10)	2.68(4)
Total	99.90(58)	99.76(30)	101.61(111)	99.97(16)	99.48(99)	99.45(115)	101.11(135)	95.48(60)	94.07(42)	103.07(153)	99.20(37)	101.40(59)	101.06(81)

LA-ICP-MS	N = 5	N = 6	N = 5	N = 6	N = 9	N = 7	N = 2	N = 2	N = 8	N = 6	N = 5	N = 6	N = 5
Si (wt%)	2.88(9)	2.70(6)	2.20(14)	1.81(2)	4.97(27)	6.21(31)	5.76(15)	0.147(2)	5.19(8)	4.04(9)	5.71(7)	4.52(11)	6.42(8)
Ti (ppm)	152(8)	107(5)	124(10)	104(7)	142(8)	196(30)	21(3)	20(2)	240(5)	32(6)	154(8)	154(24)	109(5)
Ti _{corr}	219(12)	154(7)	179(14)	150(10)	204(12)	282(43)	30(4)	29(3)	346(7)	46(9)	222(12)	222(35)	157(7)
V	8335(334)	5045(197)	8441(142)	5914(174)	4687(226)	5854(440)	4433(184)	7007(234)	5951(157)	2341(459)	6334(68)	4508(281)	4894(178)
V _{corr}	11,586(464)	7013(274)	11,733(197)	8220(242)	6515(314)	8137(611)	6162(255)	9740(325)	8272(218)	3254(638)	8804(95)	6266(391)	6803(247)
Cr	10,786(238)	7941(214)	11,995(153)	7113(143)	8596(334)	10,371(639)	8127(76)	10,213(259)	7766(96)	1809(46)	9243(88)	8797(797)	9408(106)
Mn	891(4)	809(8)	769(21)	584(7)	1343(46)	1900(67)	303(13)	313(6)	1733(11)	147(4)	1214(10)	1290(35)	1109(7)
Ni	Int.	Int.	Int.	Int.	Int.	Int.	Int.	Int.	Int.	Int.	Int.	Int.	Int.
Cu	207(3)	2346(39)	462(4)	2175(29)	6218(498)	13,243(981)	8268(131)	4323(485)	4549(85)	403(4)	3200(17)	5194(219)	3899(51)
Cu _{corr}	134(2)	1525(25)	300(3)	1414(17)	4042(324)	8608(638)	5374(85)	2810(315)	2957(55)	262(2)	2080(11)	3376(142)	534(33)
Zn	241(11)	394(24)	532(19)	567(21)	n.d.	n.d.	n.d.	n.d.	n.d.	216(14)	437(13)	282(10)	444(9)
Zn _{corr}	58(3)	95(6)	128(5)	136(5)	–	–	–	–	–	52(3)	105(3)	68(2)	106(2)
Ga	4.5(3)	3.7(1)	6.8(4)	3.0(3)	n.d.	n.d.	n.d.	n.d.	n.d.	2.6(2)	4.6(1)	13(2)	4.4(2)
Ga _{corr}	3.5(2)	2.8(1)	5.2(3)	2.3(3)	–	–	–	–	–	2.0(1)	3.6(1)	9.9(13)	3.4(1)
Ge	20,276(162)	21,268(175)	24,466(76)	21,365(111)	23,838(471)	28,197(1477)	16,606(273)	39,496(4378)	23,953(71)	18,448(363)	26,841(102)	28,636(1710)	27,004(77)
Mo	17,999(1149)	11,064(543)	15,779(497)	14,324(385)	16,090(380)	15,882(973)	14,497(1030)	26,085(2617)	20,413(722)	12,538(568)	20,024(223)	10,102(563)	19,377(393)
Mo _{corr}	28,438(1815)	17,481(858)	24,931(785)	22,632(608)	25,422(600)	25,094(1537)	22,905(1627)	41,214(4135)	32,253(1141)	19,810(897)	31,638(352)	15,961(890)	30,616(621)
In	100(6)	117(5)	136(3)	110(2)	144(3)	198(10)	113(4)	163(6)	117(4)	116(12)	150(2)	213(14)	159(3)
In _{corr}	49(4)	57(3)	67(2)	54(1)	70(2)	97(6)	80(4)	80(4)	57(2)	57(7)	73(1)	104(9)	78(2)
Sn	27,095(1459)	31,452(1154)	37,031(923)	29,615(436)	37,164(740)	52,749(2675)	30,961(1024)	43,564(1499)	31,499(1013)	31,434(2960)	40,616(440)	57,765(4403)	42,879(940)
Sn _{corr}	19,779(1065)	22,960(842)	27,033(674)	21,619(318)	27,130(540)	38,507(1953)	22,602(748)	31,802(1094)	22,994(739)	22,947(2161)	29,650(321)	42,168(3214)	31,302(686)
W	11,880(904)	6745(400)	11,973(420)	8351(322)	6704(178)	6780(891)	4275(399)	10,223(364)	8426(370)	4071(294)	8140(108)	3828(291)	7591(184)
W _{corr}	21,028(1600)	11,939(708)	21,192(743)	14,781(570)	11,866(315)	12,001(1577)	7567(706)	18,095(644)	14,914(655)	7206(520)	14,408(191)	6776(515)	13,436(326)
Pt	335(16)	1480(44)	514(11)	12(4)	11(2)	18(1)	9.4(5)	28(2)	797(514)	223,007(5535)	22,169(211)	458(430)	5.6(12)
Pb	5.4(4)	27(5)	16(2)	22(3)	11(1)	14(2)	9.4(5)	13.6(4)	18(2)	4.7(4)	10(1)	13(1)	16(1)
Pb _{corr}	1.9(1)	9.3(18)	5.7(7)	7.7(7)	3.9(4)	4.9(6)	3.3(2)	4.8(1)	6.3(8)	1.66(1)	3.6(3)	4.4(2)	5.7(3)

(continued on next page)

Table 4 (continued)

Run #	GGRFeSi1	GGRFeSi2	GGRFeSi3	GGRFeSi4	GGRFeSi5	GGRFeSi6	GGRFeSi7	GGRFeSi8	KBR1Si-1	KBR3Si-1	KBR6Si-1
EMPA	N = 30	N = 52	N = 30	N = 15	N = 37	N = 25	N = 27	N = 17	N = 19	N = 19	N = 36
Fe (wt%)	76.23(40)	78.20(35)	78.33(25)	80.28(79)	74.98(27)	76.29(20)	77.63(12)	75.89(28)	83.90(38)	81.56(38)	71.38(93)
P	–	–	–	–	1.58(10)	1.97(8)	1.52(2)	1.98(8)	0.54(6)	0.58(2)	1.49(5)
V	0.49(5)	0.52(3)	0.48(5)	0.35(4)	0.47(4)	0.45(4)	0.40(1)	0.31(2)	0.15(1)	0.57(2)	0.39(3)
Cr	0.54(2)	0.60(1)	0.75(2)	0.65(3)	0.90(3)	0.63(1)	0.63(3)	0.84(2)	0.23(1)	1.15(2)	0.99(6)
Mn	0.26(1)	0.24(1)	0.28(1)	0.21(1)	0.15(1)	0.15(1)	0.05(1)	0.11(1)	b.d.l.	0.07(1)	0.08(1)
Ni	–	–	–	–	4.00(5)	3.71(5)	3.06(4)	3.49(4)	1.84(7)	2.41(3)	4.62(27)
Cu	0.30(4)	0.44(7)	0.66(7)	0.29(5)	–	–	–	–	0.10(1)	0.73(2)	0.04(1)
Ge	–	–	–	–	3.34(4)	2.53(3)	2.39(3)	2.67(3)	1.95(22)	1.18(8)	4.52(33)
Mo	–	–	–	–	3.93(22)	3.25(14)	3.19(4)	3.66(18)	1.88(8)	1.50(6)	3.67(13)
Sn	1.09(27)	1.96(35)	1.02(16)	0.67(14)	–	–	–	–	1.50(18)	2.16(8)	3.50(9)
W	1.66(12)	1.93(8)	1.83(11)	1.32(14)	–	–	–	–	1.75(3)	1.19(4)	1.17(5)
Pt	4.16(19)	b.d.l.	b.d.l.	b.d.l.	b.d.l.	b.d.l.	b.d.l.	b.d.l.	b.d.l.	b.d.l.	b.d.l.
Si	14.71(9)	14.81(8)	15.39(9)	15.19(22)	10.62(15)	10.31(15)	7.81(5)	10.04(18)	0.02(1)	2.34(2)	3.44(14)
Total	99.50(17)	98.74(10)	98.83(13)	99.02(45)	99.97(12)	99.33(15)	96.69(11) ^h	95.01(19)	93.87(24)	95.41(37)	95.28(25)
Fe (wt%)	N = 16	N = 12	N = 13	N = 10	N = 16	N = 19	N = 15	N = 19	n.a.	N = 31	N = 14
Ni	75.09(41)	78.72(32)	79.06(54)	80.23(96)	74.82(49)	75.74(35)	78.05(38)	76.00(25)	–	82.08(50)	75.80(55)
Si	0.034(4)	0.034(3)	0.05(1)	0.05(1)	3.78(4)	3.42(5)	2.95(3)	3.32(3)	–	2.10(11)	3.09(28)
Si	13.27(6)	13.88(9)	14.23(11)	14.50(34)	9.50(10)	8.92(16)	7.02(14)	8.75(6)	–	2.58(13)	3.83(29)
C	1.41(6)	1.65(6)	1.78(11)	1.49(14)	1.70(7)	1.63(9)	2.46(3)	1.78(3)	–	4.12(6)	3.50(15)
Total	98.30(43)	99.96(33)	100.58(80)	99.75(65)	101.73(53)	98.71(38)	98.65(29)	101.41(28)	–	100.16(50)	101.96(55)

LA-ICP-MS	N = 7	N = 7	N = 7	N = 7	N = 8	N = 7	N = 7	N = 7	N = 7	N = 7	N = 5	N = 4
Si (wt%)	Int.	Int.	Int.	Int.	Int.	Int.	Int.	Int.	Int.	Int.	Int.	Int.
Ti (ppm)	95(12)	96(5)	92(7)	94(9)	76(10)	84(6)	70(5)	90(8)	b.d.l.	48(11)	2.43(4)	3.14(14)
Ti _{corr}	137(17)	138(7)	132(10)	135(13)	109(14)	121(9)	101(7)	130(12)	69(16)	934(158)	862(106)	862(106)
V	3807(161)	3924(175)	3731(77)	3596(191)	2972(106)	3540(96)	2819(209)	2633(164)	948(38)	1345(228)	1241(153)	1241(153)
V _{corr}	5292(224)	5454(243)	5186(106)	4998(265)	4131(147)	4921(133)	3918(290)	3660(228)	1318(53)	4879(203)	4704(483)	4704(483)
Cr	5450(64)	5609(208)	6906(87)	5818(119)	8381(152)	7449(118)	5188(386)	7715(251)	1587(29)	6782(282)	6539(671)	6539(671)
Mn	2990(93)	2586(118)	2821(51)	2004(50)	1804(32)	1766(36)	481(33)	1129(65)	b.d.l.	10,132(140)	9424(305)	9424(305)
Ni	–	–	–	–	46,175(808)	40,981(546)	28,105(2267)	32,660(2128)	Int.	726(6)	645(7)	645(7)
Cu	5860(404)	6572(599)	8186(312)	3997(175)	298(6)	210(4)	4245(385)	542(33)	Int.	9201(234)	1073(23)	1073(23)
Cu _{corr}	3809(263)	4272(389)	5321(203)	2598(114)	194(4)	137(3)	2759(250)	352(21)	1137(9)	5981(152)	697(15)	697(15)
Zn	126(8)	287(29)	62(4)	38(3)	249(9)	61(2)	37,208(3381)	1982(152)	n.d.	n.d.	n.d.	n.d.
Zn _{corr}	30(2)	69(7)	15(1)	9(1)	60(2)	15(1)	8930(811)	476(36)	–	–	–	–
Ga	6.6(4)	5.6(2)	5.7(1)	5.7(2)	6.6(3)	5.7(2)	5.6(4)	4.7(3)	n.d.	n.d.	n.d.	n.d.
Ga _{corr}	5.1(3)	4.3(2)	4.4(1)	4.4(2)	5.1(2)	4.4(2)	4.4(3)	3.6(2)	–	–	–	–
Ge	–	–	–	–	–	–	–	–	–	–	–	–
Mo	–	–	–	–	–	–	–	–	–	–	–	–
Mo _{corr}	–	–	–	–	–	–	–	–	–	–	–	–
In	77(11)	88(11)	61(5)	50(3)	–	–	–	–	73(1)	87(3)	230(4)	230(4)
In _{corr}	38(7)	43(7)	30(3)	24(2)	–	–	–	–	36(1)	43(2)	113(3)	113(3)
Sn	20,575(2863)	23,852(2976)	15,711(1222)	13,307(846)	–	–	–	–	19,465(362)	23,860(837)	59,278(1338)	59,278(1338)
Sn _{corr}	15,020(2090)	17,412(2172)	11,469(892)	9714(618)	–	–	–	–	14,209(264)	17,418(611)	43,273(977)	43,273(977)
W	9721(944)	13,781(852)	13,081(673)	11,564(991)	–	–	–	–	8287(139)	6103(316)	6373(445)	6373(445)
W _{corr}	17,206(1671)	24,392(1508)	23,153(1191)	20,468(1754)	–	–	–	–	14,668(246)	10,802(560)	11,280(788)	11,280(788)
Pt	36,050(1135)	1.0(1)	0.8(4)	1.3(2)	1.9(1)	1.5(3)	6.4(18)	341(27)	36(3)	22(16)	221(23)	221(23)
Pb	5.6(9)	8.7(17)	11(1)	9.1(6)	18(1)	10(1)	661(121)	62(19)	3.8(1)	6.3(3)	29(3)	29(3)
Pb _{corr}	1.96(32)	3.1(6)	3.9(4)	3.2(2)	6.3(3)	3.6(2)	231(42)	22(7)	1.32(4)	2.2(1)	10(1)	10(1)

^a Number of analyses. ^b Values in parentheses are two standard errors for EMPA and LA-ICP-MS in terms of least digits cited. ^c b.d.l. = below detection limit. ^d n.d. = not determined. ^e Concentration determined by EPMA used as internal standard for LA-ICP-MS processing. ^f Corrected using the model of Steenstra et al. (2019; see Appendix Section A.2). ^g low Fe content presumably due to Pt which was not analysed. ^h Low total of metal in run GGRFeSi7 is due to Zn, which was not measured using EPMA.

Table 5
Major and minor element composition of metallic melts of LG-GG-PR series (carbon-free experiments).

Run #	EPMA (wt%)	LG1Si-1	LG1Si-2	LG1Si-3	LG1Si-4	LG1Si-5	GG1Si-1	GG1Si-2	GG1Si-3	GG3Si-1	GG3Si-2	GG3Si-3	GG6Si-1
		N = 49 ^a	N = 54	N = 54	N = 28	N = 28	N = 29	N = 26	N = 25	N = 30	N = 28	N = 32	N = 25
Fe		88.10(29) ^b	88.71(32)	88.64(26)	89.08(44)	86.89(81)	89.17(39)	90.17(43)	90.20(33)	90.41(19)	89.14(20)	87.96(25)	87.20(27)
Cr		b.d.l.	b.d.l.	b.d.l.	b.d.l.	b.d.l.	b.d.l.	0.030(3)	0.036(3)	0.182(5)	0.137(5)	0.18(1)	0.47(1)
Mn		b.d.l.	b.d.l.	b.d.l.	b.d.l.	b.d.l.	b.d.l.	b.d.l.	b.d.l.	b.d.l.	< 0.020(4)	b.d.l.	0.03(1)
Ni		5.83(2)	5.67(2)	5.60(2)	5.88(3)	6.20(4)	5.80(4)	5.29(3)	5.48(3)	3.85(1)	4.47(2)	4.58(6)	3.85(2)
As		1.37(1)	1.42(2)	1.26(1)	1.35(2)	1.31(2)	1.89(4)	1.09(2)	1.10(3)	1.59(2)	1.17(2)	1.13(4)	1.32(4)
Se		0.67(7)	0.62(9)	0.52(6)	1.03(13)	1.66(30)	0.83(17)	0.36(4)	0.53(9)	0.26(3)	0.37(5)	0.27(5)	0.18(4)
Cd		0.02(2)	0.03(3)	0.06(5)	0.08(9)	0.28(16)	0.10(8)	0.03(1)	0.30(9)	< 0.01(2)	0.06(6)	b.d.l.	b.d.l.
In		0.85(6)	0.75(7)	0.50(3)	0.58(7)	0.81(14)	0.39(7)	0.26(2)	0.31(5)	0.43(2)	0.33(3)	0.27(4)	0.31(3)
Sb		2.06(6)	1.46(3)	1.97(4)	2.08(5)	2.06(7)	2.05(11)	1.95(2)	1.88(7)	2.11(5)	1.63(8)	1.45(8)	1.96(12)
Te		0.25(5)	0.29(8)	0.21(4)	0.45(11)	0.91(17)	0.31(5)	0.14(1)	0.24(4)	0.15(2)	0.18(3)	0.15(2)	0.13(3)
Pb		0.17(8)	0.21(11)	0.11(4)	0.18(9)	0.35(9)	0.08(2)	0.06(1)	0.14(3)	0.05(2)	0.09(3)	0.05(1)	0.04(1)
Si		< 0.021(2)	0.076(2)	0.308(3)	0.058(4)	0.035(5)	b.d.l.	b.d.l.	b.d.l.	1.15(1)	2.84(1)	2.95(13)	3.92(2)
Total		99.50(10)	99.32(12)	99.21(11)	100.76(11)	100.64(20)	100.65(29)	99.39(47)	100.23(14)	100.17(13)	100.43(11)	99.00(4)	99.43(24)

LA-ICP-MS	N = 10	N = 10	N = 11	N = 10	N = 11	N = 10	N = 10	N = 10	N = 9	N = 10	N = 10	N = 7	N = 10
Si (wt%)	b.d.l. ^c	b.d.l.	b.d.l.	b.d.l.	b.d.l.	b.d.l.	b.d.l.	b.d.l.	b.d.l.	0.99(3)	2.46(4)	2.79(29)	3.45(6)
Ti (ppm)	b.d.l.	12(8)	14(7)	9.9(39)	14(6)	b.d.l.	b.d.l.	b.d.l.	b.d.l.	15(1)	15(1)	57(23)	18(2)
Ti _{corr}	–	17(12)	20(12)	14(6)	14(6)	–	–	–	–	22(1)	22(1)	82(33)	26(3)
V	2.2(14)	3.0(2)	3.7(2)	1.63(1)	1.33(4)	b.d.l.	b.d.l.	1.06(7)	0.91(7)	7.7(1)	4.6(3)	5.4(12)	12.5(2)
V _{corr}	3.1(20)	4.2(3)	5.1(3)	2.3(2)	1.85(6)	–	–	1.48(9)	1.26(10)	10.7(2)	6.4(5)	7.5(17)	17.3(3)
Cr	27(2)	45(2)	58(2)	36(1)	28(2)	211(11)	344(6)	417(6)	41(6)	1150(11)	1150(11)	1674(129)	3857(22)
Mn	5.6(34)	11(1)	24(1)	8.9(11)	5.4(3)	6.8(6)	11(1)	11(1)	21(1)	178(4)	349(3)	233(31)	357(14)
Ni	Int. ^d	Int.	Int.	Int.	Int.	Int.	Int.	Int.	Int.	Int.	Int.	Int.	Int.
Cu	1.25(2)	104(1)	68(1)	71(2)	75(3)	263(8)	92(1)	104(2)	104(2)	191(5)	137(1)	175(10)	224(3)
Cu _{corr} ^e	81(1)	68(1)	44(1)	46(1)	49(2)	171(5)	60(1)	68(2)	68(2)	124(3)	89(1)	114(7)	146(2)
As	13.301(147)	14.734(82)	11.219(74)	11.740(108)	12.096(116)	16.838(173)	9856(40)	9856(40)	10,100(106)	14,179(148)	11,193(70)	10,784(158)	14,099(346)
Se	9280(210)	8510(194)	7237(205)	11,184(392)	13,257(469)	9362(685)	5404(101)	5404(101)	9518(294)	3290(177)	5219(115)	5233(570)	3032(141)
Se _{corr}	6683(301)	6127(140)	5211(167)	8052(282)	9545(338)	6741(493)	3891(73)	3891(73)	6853(212)	3758(83)	3768(410)	2183(102)	2183(102)
Cd	3019(556)	2240(142)	3431(195)	4853(283)	7762(618)	11,373(1695)	8083(314)	8083(314)	24,495(891)	2248(151)	6801(189)	3243(387)	2096(258)
Cd _{corr}	423(78)	314(20)	480(32)	679(40)	1087(87)	1132(44)	1132(44)	1132(44)	3429(125)	315(21)	952(26)	454(54)	293(36)
In	14,151(366)	12,861(286)	8643(153)	8091(265)	9153(371)	5516(332)	4395(76)	4395(76)	6136(184)	5876(137)	6083(126)	5553(512)	5294(219)
In _{corr}	6934(179)	6302(140)	4235(87)	3965(130)	4485(182)	2752(163)	2154(37)	2154(37)	3007(90)	2879(67)	2981(62)	2721(251)	2594(107)
Sn	9.8(4)	8.4(4)	4.7(2)	5.5(2)	6.3(3)	5.2(3)	3.4(2)	3.4(2)	3.6(2)	7.84(3)	6.3(2)	7.3(8)	16(1)
Sn _{corr}	7.2(2)	6.2(3)	3.4(1)	4.0(1)	4.6(2)	3.8(2)	2.5(2)	2.5(2)	2.7(1)	5.7(2)	4.6(2)	5.3(6)	11(5)
Sb	24,877(515)	17,886(174)	21,995(274)	20,238(128)	19,624(508)	20,788(735)	20,083(101)	20,083(101)	20,929(318)	22,828(493)	20,122(328)	18,992(668)	28,253(1145)
Sb _{corr}	18,409(381)	13,236(129)	16,276(203)	14,976(95)	14,522(376)	15,383(544)	14,861(75)	14,861(75)	15,487(235)	16,893(365)	14,890(243)	14,047(494)	20,915(847)
Te	3983(301)	4305(145)	2896(52)	6286(251)	10,832(423)	4552(268)	2517(70)	2517(70)	5038(180)	1282(61)	3105(106)	2768(290)	1771(98)
Te _{corr}	1553(117)	1679(57)	1129(20)	2452(98)	4224(165)	1775(105)	982(27)	982(27)	1965(70)	500(24)	1211(41)	1080(113)	691(38)
Pb	2554(483)	1830(101)	1076(47)	1973(138)	2593(180)	1257(136)	929(29)	929(29)	2672(132)	641(35)	1496(52)	862(121)	461(63)
Pb _{corr}	894(169)	641(35)	377(16)	691(48)	908(63)	440(48)	325(10)	325(10)	935(46)	224(12)	524(18)	302(42)	161(22)

Run #	EPMA (wt%)	GG6Si-2	GG6Si-1b	GG6Si-2b	GG6Si-3b	GGFeSi-1	GGFeSi-2	GGFeSi-3	GGFeSi-1b	GGFeSi-2b	GGFeSi-3b	PR1451
		N = 30	N = 18	N = 31	N = 30	N = 27	N = 24	N = 26	N = 29	N = 26	N = 26	N = 42
Fe		86.26(18)	92.33(39)	87.87(17)	86.80(19)	82.26(13)	82.00(27)	81.21(21)	83.87(15)	84.06(26)	81.14(14)	82.16(51)
Cr		0.39(1)	0.30(1)	0.45(1)	0.35(1)	0.51(1)	0.29(1)	0.27(1)	0.63(1)	0.52(1)	0.31(1)	0.333(5)
Mn		< 0.02(1)	b.d.l.	0.040(5)	0.04(1)	< 0.023(4)	0.27(1)	0.11(2)	0.23(1)	0.11(2)	0.09(1)	0.20(1)
Ni		3.83(2)	2.73(9)	3.96(2)	3.68(2)	3.60(2)	4.07(2)	4.16(2)	3.21(2)	4.03(3)	4.49(3)	3.73(5)
As		1.25(2)	1.02(8)	1.13(3)	0.99(2)	0.92(3)	0.97(3)	0.91(3)	1.05(3)	0.95(5)	1.02(3)	2.16(11)

(continued on next page)

Table 5 (continued)

Run #	GG6Si-2	GG6Si-3	GG6Si-1b	GG6Si-2b	GG6Si-3b	GGFeSi-1	GGFeSi-2	GGFeSi-3	GGFeSi-1b	GGFeSi-2b	GGFeSi-3b	PR1451
EPMA (wt%)	N = 30	N = 18	N = 31	N = 30	N = 30	N = 27	N = 24	N = 26	N = 29	N = 29	N = 26	N = 42
Se	0.27(3)	0.36(2)	0.16(2)	0.33(5)	0.22(2)	b.d.l.	0.06(3)	0.06(3)	b.d.l.	0.17(5)	0.05(1)	0.07(3)
Cd	b.d.l.	b.d.l.	b.d.l.	b.d.l.	b.d.l.	b.d.l.	b.d.l.	b.d.l.	b.d.l.	b.d.l.	b.d.l.	0.09(2)
In	0.27(2)	0.32(2)	0.24(2)	0.25(2)	0.21(2)	0.09(1)	0.08(4)	0.12(2)	0.17(3)	0.20(3)	0.13(1)	0.64(6)
Sb	2.27(13)	1.23(17)	1.78(8)	2.25(10)	1.96(9)	1.14(8)	1.34(14)	1.40(6)	1.62(7)	1.72(14)	2.09(7)	2.28(21)
Te	0.12(1)	0.13(2)	0.09(1)	0.13(2)	0.10(1)	0.04(1)	0.06(1)	0.07(2)	0.05(1)	0.09(1)	0.06(1)	0.08(2)
Pb	0.04(1)	0.05(1)	< 0.02(1)	< 0.02(1)	< 0.03(1)	< 0.02(1)	< 0.01(1)	0.03(1)	< 0.02(2)	< 0.02(1)	< 0.02(1)	0.06(2)
Si	4.28(1)	1.26(1)	4.61(1)	5.71(2)	5.03(2)	9.93(8)	11.11(11)	11.27(4)	8.14(5)	8.82(5)	11.78(12)	6.58(22)
Total	98.99(11)	99.13(34)	100.35(11)	100.57(9)	100.48(9)	98.82(13)	100.34(19)	99.62(20)	99.01(16)	100.72(13)	101.18(15)	98.38(32)

LA-ICP-MS	N = 10	N = 8	N = 10	N = 8	N = 10	N = 8	N = 8	N = 10	N = 8	N = 3	N = 10	N = 10
Si (wt%)	3.79(4)	1.87(13)	4.28(8)	5.21(22)	4.69(8)	10.44(24)	10.37(29)	10.39(26)	7.74(10)	8.36(28)	10.95(18)	4.93(18)
Ti (ppm)	17(2)	36(5)	22(2)	21(2)	21(2)	388(7)	117(4)	84(5)	192(3)	47(3)	97(5)	109(20)
Ti _{corr}	24(3)	52(7)	32(3)	30(3)	30(3)	559(10)	168(6)	121(7)	276(4)	68(4)	140(7)	157(29)
V	10.0(4)	5.2(3)	13.2(4)	9.7(2)	7.7(6)	18.0(4)	11.8(2)	10.6(4)	17.1(4)	13(1)	9.8(5)	17(1)
V _{corr}	14(1)	7.2(4)	18(1)	13.5(3)	11(1)	25(1)	16.4(3)	15(1)	24(1)	18(1)	14(1)	24(1)
Cr	3124(26)	2442(64)	3625(48)	3092(66)	3190(44)	5095(64)	2761(36)	2388(35)	5156(47)	4423(215)	2791(31)	2365(60)
Mn	252(13)	98(5)	419(17)	436(318)	288(9)	2814(37)	1593(128)	1538(127)	2112(14)	1650(154)	1376(130)	3086(335)
Ni	Int.	Int.	Int.	Int.	Int.	Int.	Int.	Int.	Int.	Int.	Int.	Int.
Cu	170(2)	181(7)	152(2)	172(4)	188(3)	225(9)	186(5)	192(7)	224(5)	189(3)	268(7)	420(14)
Cu _{corr}	111(1)	118(5)	99(1)	112(3)	122(4)	146(6)	121(3)	125(5)	146(3)	123(2)	174(5)	273(10)
Zn	n.d.	n.d.	251(10)	247(50)	217(9)	n.d.	n.d.	n.d.	223(7)	217(7)	200(15)	119(8)
Zn _{corr}	-	-	60(2)	59(9)	52(2)	-	-	-	53(2)	52(2)	48(4)	29(2)
Ga	n.d.	n.d.	6.7(3)	6.8(1)	5.9(3)	n.d.	n.d.	n.d.	8.5(2)	7.0(6)	6.9(3)	5.9(3)
Ga _{corr}	-	-	5.2(2)	5.2(1)	4.5(3)	-	-	-	6.6(1)	5.4(5)	5.3(2)	4.6(2)
As	11.658(86)	6245(48)	13.216(123)	10.667(116)	14.048(193)	10.680(343)	12.448(303)	10.708(344)	11.429(155)	10.079(110)	13.258(243)	27.239(979)
Se	3379(142)	4980(361)	2504(180)	4504(149)	3257(160)	100(7)	736(155)	917(49)	201(19)	1767(235)	1463(216)	1947(350)
Se _{corr}	2433(102)	3586(260)	1803(130)	3243(107)	2345(115)	72(5)	530(112)	660(35)	145(14)	1272(169)	1053(156)	1402(252)
Cd	1352(64)	1631(152)	1538(175)	1638(224)	1831(124)	710(38)	1052(147)	652(19)	2458(132)	896(137)	4514(1062)	4514(1062)
Cd _{corr}	189(9)	228(21)	215(25)	229(31)	256(17)	99(5)	147(21)	91(3)	122(13)	344(18)	125(19)	632(149)
In	4025(115)	5915(116)	4405(131)	4686(100)	4083(126)	1935(119)	2071(215)	2548(149)	3353(153)	4263(350)	3003(172)	14,095(923)
In _{corr}	1972(56)	2898(57)	2158(64)	2296(49)	2001(62)	948(58)	1015(105)	1249(73)	1643(75)	2089(172)	1471(84)	6907(452)
Sn	13.4(4)	13.1(14)	13.6(4)	13.6(5)	11.1(3)	11(1)	10.1(5)	12(1)	16(1)	13.7(4)	14(1)	23(1)
Sn _{corr}	9.8(3)	9.6(10)	10.0(3)	9.9(4)	8.2(4)	8.0(6)	7.4(4)	8.9(4)	11.6(5)	10.0(3)	10.3(5)	16(1)
Sb	26.657(318)	13.777(1602)	24.313(561)	30.880(670)	27.112(629)	14.905(1160)	18.394(744)	20.071(1034)	21.638(911)	23.617(837)	29.754(1182)	38.956(2336)
Sb _{corr}	19.726(235)	10.195(1185)	17.992(415)	22.851(496)	20.063(465)	11.030(858)	13.612(551)	14.853(765)	16.012(674)	17.477(619)	22.018(875)	28.828(1729)
Te	1575(75)	1772(73)	1242(95)	1795(104)	1408(82)	117(7)	490(79)	370(19)	196(23)	1027(100)	858(153)	2316(435)
Te _{corr}	614(29)	691(28)	484(37)	700(41)	549(64)	46(3)	191(31)	144(7)	76(9)	401(39)	335(60)	903(169)
Pb	343(31)	511(127)	261(29)	275(36)	354(17)	40(2)	118(28)	55(2)	66(10)	194(14)	98(15)	1216(365)
Pb _{corr}	120(11)	179(44)	91(10)	96(13)	124(6)	14(1)	41(10)	19(1)	23(4)	68(5)	34(5)	426(128)

Run #	PR1453	PR1455	PR1457	PR1458	PR1459	PR1512	PR1513	PR1514	PR1515
EPMA (wt%)	N = 76	N = 29	N = 61	N = 47	N = 79	N = 27	N = 15	N = 30	N = 17
Fe	82.28(32)	86.83(61)	79.44(32)	85.71(36)	79.16(8)	79.93(36)	80.42(243)	84.87(45)	78.72(119)
Cr	0.360(4)	0.29(1)	0.224(3)	0.390(5)	0.399(3)	0.54(3)	0.31(1)	0.19(1)	0.15(2)
Mn	0.17(3)	0.11(1)	0.11(1)	0.12(1)	0.331(4)	0.32(5)	0.09(2)	0.12(1)	0.04(1)
Ni	4.47(5)	4.69(5)	3.69(2)	4.23(2)	3.61(1)	3.97(9)	4.94(35)	4.59(6)	4.62(15)
As	2.19(9)	1.45(7)	1.99(4)	1.51(4)	2.37(3)	2.24(17)	2.19(28)	1.71(6)	1.42(4)
Se	0.19(5)	0.80(13)	0.06(3)	0.41(6)	0.016(4)	0.27(9)	0.11(10)	0.86(13)	1.92(33)
Cd	0.07(2)	0.57(20)	0.04(1)	0.20(9)	0.03(1)	0.08(2)	0.04(2)	0.28(5)	0.53(27)

(continued on next page)

Table 5 (continued)

Run #	PR1453	PR1455	PR1457	PR1458	PR1459	PR1512	PR1513	PR1514	PR1515
EPMA (wt%)	N = 76	N = 29	N = 61	N = 47	N = 79	N = 27	N = 15	N = 30	N = 17
In	0.57(5)	0.80(11)	0.25(1)	0.91(9)	0.15(1)	0.75(6)	0.57(28)	0.93(9)	2.07(18)
Sb	2.65(20)	1.75(14)	2.47(7)	1.95(7)	1.77(5)	2.76(27)	3.88(179)	2.26(22)	2.37(14)
Te	0.15(3)	0.71(16)	< 0.03(1)	0.19(3)	< 0.01(3)	0.20(4)	0.23(12)	0.52(7)	0.87(12)
Pb	0.04(2)	0.56(17)	< 0.01(1)	0.06(3)	< 0.01(5)	0.09(3)	0.17(16)	0.28(5)	1.01(27)
Si	6.94(5)	1.04(2)	10.30(4)	1.78(1)	9.53(4)	6.90(9)	5.45(28)	2.83(3)	0.21(4)
Total	100.08(14)	99.61(16)	98.63(11)	97.47(25)	97.44(7)	98.05(38)	98.41(43)	99.94(11)	93.94(104) ^f
LA-ICP-MS	N = 9	N = 10	N = 15	N = 10	N = 10	N = 12	n.a. ^d	N = 10	N = 8
Si (wt%)	4.58(24)	1.04(7)	8.56(22)	1.49(8)	8.33(17)	6.31(9)	–	2.22(615)	0.23(4)
Ti (ppm)	123(23)	62(11)	109(13)	75(17)	549(23)	148(16)	–	65(9)	b.d.l.
Ti _{corr}	177(33)	89(16)	157(19)	108(24)	791(33)	213(23)	–	94(13)	–
V	10(2)	9.2(5)	7.4(11)	10(1)	17(1)	13(2)	–	17(1)	4.1(7)
V _{corr}	14(2)	13(1)	10(2)	14(2)	23(2)	18(3)	–	24(2)	5.7(10)
Cr	2551(27)	2396(42)	1744(32)	3072(40)	3127(28)	4338(34)	–	1535(21)	920(17)
Mn	4003(435)	1212(97)	1530(212)	1561(101)	3140(32)	4802(478)	–	1685(117)	471(40)
Ni	Int.	Int.	Int.	Int.	Int.	Int.	–	Int.	Int.
Cu	386(12)	166(9)	244(8)	203(8)	306(12)	413(19)	–	209(11)	81(8)
Cu _{corr}	251(8)	108(6)	158(6)	132(5)	199(8)	269(13)	–	136(8)	53(5)
Zn	447(26)	108(4)	91(10)	151(7)	133(12)	257(22)	–	129(9)	57(5)
Zn _{corr}	107(7)	26(1)	22(2)	36(2)	32(3)	62(5)	–	31(2)	14(1)
Ga	5.8(4)	3.6(2)	5.7(4)	4.5(3)	6.5(4)	8.2(4)	–	3.4(3)	1.73(30)
Ga _{corr}	4.4(3)	2.7(2)	4.4(3)	3.4(3)	5.0(3)	6.3(3)	–	2.6(3)	1.33(23)
As	31,072(1077)	14,441(460)	24,927(618)	17,608(499)	28,468(483)	28,751(821)	–	19,140(245)	14,104(695)
Se	5870(457)	7848(1285)	1184(257)	5998(588)	114(12)	5376(852)	–	15,804(1424)	21,351(2685)
Se _{corr}	4227(329)	5651(925)	853(185)	4319(423)	82(9)	3871(613)	–	11,379(1025)	15,373(1933)
Cd	6391(943)	16,853(3323)	1176(208)	6712(863)	729(132)	7953(2360)	–	24,648(5128)	40,560(16340)
Cd _{corr}	895(132)	2359(465)	165(29)	940(121)	102(19)	1113(330)	–	3451(718)	5678(2288)
In	17,302(1115)	12,934(1629)	5160(476)	16,515(1199)	3019(319)	15,070(1819)	–	23,736(2277)	30,500(4590)
In _{corr}	8478(547)	6073(798)	2528(233)	8093(588)	1479(156)	7384(891)	–	11,631(1116)	14,945(2249)
Sn	35(1)	7.6(5)	17(1)	8.2(3)	20(2)	21(1)	–	7.9(3)	3.1(4)
Sn _{corr}	26(1)	5.6(4)	13(1)	6.0(2)	14(1)	15(1)	–	5.8(3)	2.3(3)
Sb	56,910(2482)	19,861(1285)	35,222(2184)	25,858(1151)	24,625(1809)	43,510(1197)	–	35,739(1007)	26,400(1159)
Sb _{corr}	42,113(1836)	14,967(951)	26,064(1616)	19,135(852)	18,222(1339)	32,198(886)	–	26,447(745)	19,536(858)
Te	6240(692)	12,492(1847)	955(180)	5021(548)	102(26)	8016(2139)	–	22,149(3067)	25,314(7021)
Te _{corr}	2434(270)	4872(720)	372(70)	1958(214)	40(10)	3126(834)	–	8638(1196)	9872(2738)
Pb	2166(263)	7487(1384)	308(86)	1693(339)	50(12)	2310(778)	–	15,922(4552)	27,101(12157)
Pb _{corr}	758(92)	2620(484)	108(30)	593(199)	17(4)	809(272)	–	5573(1593)	9485(4255)

^a Number of analyses ^b Values in parentheses are two standard errors for EPMA and LA-ICP-MS in terms of least digits cited ^c b.d.l. = below detection limit ^d Concentration determined by EPMA used as internal standard for LA-ICP-MS processing ^e Corrected using the model of Steenstra et al. (2019) ^f Low total due to porous texture of metal phase ^g n.a. = not analysed due to small size.

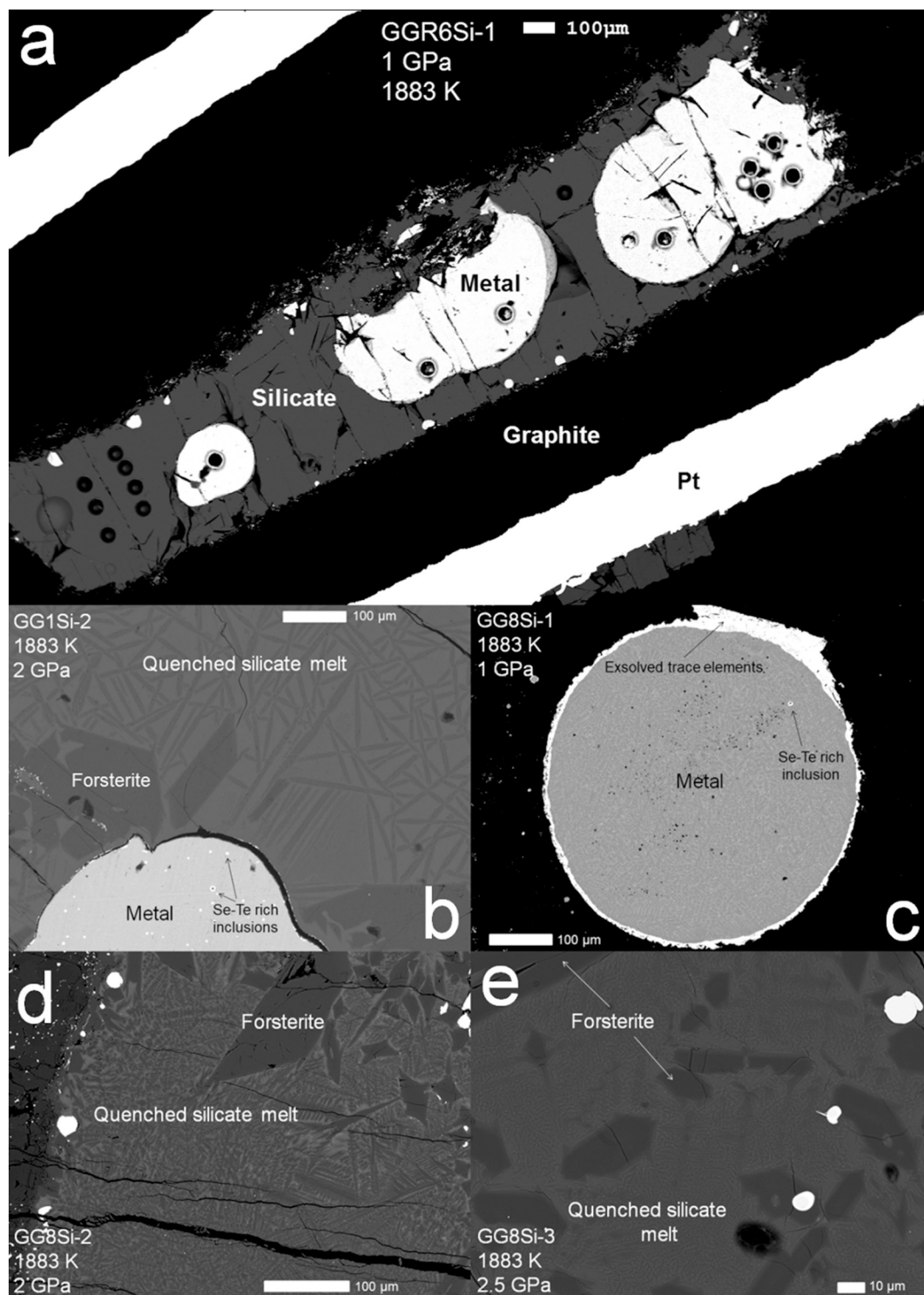


Fig. 1. Backscattered electron images of typical run products (a) run GGR6Si-1, performed at 1883 K and 1 GPa in a graphite inner and Pt outer capsule, showing both metal and silicate phases. Pits are from LA-ICP-MS analyses (b) Close-up of typical quench textures observed in run GG1Si-2 performed in a MgO capsule at 2 GPa and 1883 K (c) Close-up of metallic quench textures in run GG8Si-1, performed in a MgO capsule at 1 GPa and 1883 K (d, e) Additional details of silicate quench textures of runs GG8Si2 and 3. Both experiments were conducted in MgO capsules at 2 and 2.5 GPa at 1883 K, respectively.

$\gamma_{\text{SiO}_2}^{\text{silicate}}$ has to be assumed to be unity, as there is no predictive model for $\gamma_{\text{SiO}_2}^{\text{silicate}}$ at very low f_{O_2} . Previous studies found minor variability of $\gamma_{\text{SiO}_2}^{\text{silicate}}$ in FeO-free melts (Stolyarova et al., 2003) at similar run temperatures, so no significant offset of the new results is expected because of this assumption. Fig. 2 shows a comparison between ΔIW

and $\Delta\text{Si-SiO}_2$ values from this study and previous studies for C-free and C-saturated experiments. The comparison confirms the previous hypothesis that $\gamma_{\text{FeO}}^{\text{silicate}}$ is much lower at highly reducing conditions under C-saturated conditions.

The dramatic variations of $\gamma_{\text{FeO}}^{\text{silicate}}$ are not observed for C-free

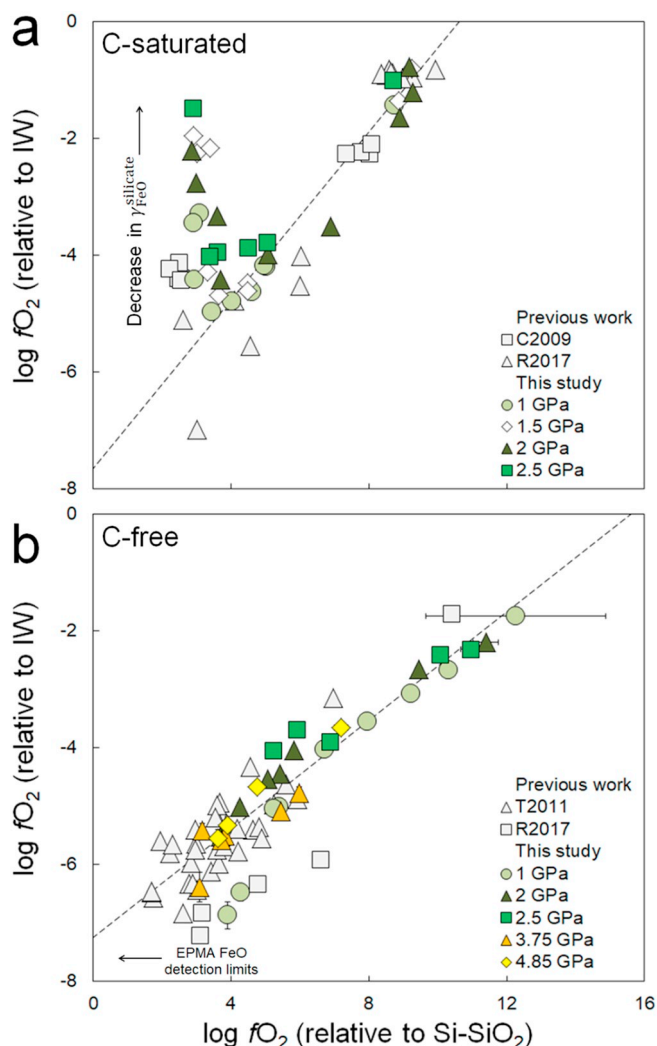


Fig. 2. Comparison of experimental oxygen fugacities calculated using the iron-wüstite buffer (ΔIW) and the Si-SiO₂ buffer ($\Delta\text{Si-SiO}_2$) from this work (filled) and previous studies open symbols from C-free and C-saturated experiments (C2009 = Corgne et al., 2009; T2011 = Tuff et al., 2011; R2017 = Righter et al., 2017). The ΔIW values were calculated assuming non-ideal $\gamma_{\text{Fe}^{\text{metal}}}$ (Table 1). The positive offset of experiments with the lowest $\Delta\text{Si-SiO}_2$ in C-saturated experiments must be due to a substantial decrease of $\gamma_{\text{FeO}^{\text{silicate}}}$. Line represents a linear fit through experimental series GGR1Si, GGR3Si, KBR1Si and KBR3Si runs ($\Delta\text{IW} = 0.7203 \cdot \Delta\text{Si-SiO}_2 - 7.6597$; $R^2 = 0.97$).

experiments. A possible explanation for this is that dissolved C in the silicate melt has a much stronger effect on $\gamma_{\text{FeO}^{\text{silicate}}}$ at highly reduced conditions, compared to less reduced systems, despite the low solubility of C in highly reduced melts (~ 50 ppm, Li et al., 2016). We stress that the abundance of FeO and the behavior of $\gamma_{\text{FeO}^{\text{silicate}}}$ in the C-saturated experiments cannot be the result of analytical issues, as EPMA and LA-ICP-MS derived Fe concentrations of the silicate melt agree well (Fig. A.4).

To calculate the expected $\gamma_{\text{FeO}^{\text{silicate}}}$ for the most reducing experiments performed in graphite capsules, the correlation between ΔIW and $\Delta\text{Si-SiO}_2$ at less reduced conditions is used (Fig. 2) (see Rose-Weston et al., 2009). The $\gamma_{\text{FeO}^{\text{silicate}}}$ values for the most reducing conditions were then calculated using the ΔIW predicted from the latter correlation (Table 1). Corrected ΔIW values for C-saturated experiments with the most Si-rich metals are significantly lower (up to 4 log units). These corrected values will be used for these specific set of runs throughout

the remainder of this paper.

3.2.1. Monovalent and divalent elements: Cu, Cr, Mn, Ni, Ge, Zn, Sn, Cd, Pb

Assuming no other effects of variable silicate and/or metal compositions on siderophile element activities, the slope of $\log D_M^*$ versus $f\text{O}_2$ should yield their valence state(s). Vogel et al. (2018) showed the competing interactions between the effects of Si on trace element activities and possible changes in their valence states. Given the strong effects of Si on elemental activities (Vogel et al., 2018), the valence states of the various elements can therefore only be reliably determined at the most oxidized conditions studied here, in which Si does not partition into the metal. At lower oxygen fugacities and the corresponding partitioning of Si into metal, negative deviations of D values based on valence states illustrate the negative effect of Si on trace element activities in Si-bearing Fe-rich metal alloys.

The new experimental results are most consistent with a 1+ or 2+ valence state for Cu. A 1+ valence state for Cu is proposed in previous work (Righter and Drake, 2000; Holzheid and Lodders, 2001; Vogel et al., 2018), but some contribution of Cu^{2+} is expected, especially for alkali-bearing melts (Schmitt et al., 1989; Holzheid and Lodders, 2001). Corgne et al. (2008) suggested that Cu may be partly present as Cu^{2+} at similar $f\text{O}_2$ in alkali-free melts. For simplicity, we assume a 1+ valence state for Cu in subsequent calculations, based on the recent work of Vogel et al. (2018).

The new results are most consistent with a 2+ valence state of Cr, Mn, Ni, Zn and Pb in the silicate melt up to a $f\text{O}_2$ of $\Delta\text{IW} = -3$ to -1 (Figs. 3–5) (Drake et al., 1989; Berry et al., 2006; Corgne et al., 2008; Wood and Halliday, 2010; Siebert et al., 2011; Steenstra et al., 2017a; Vogel et al., 2018).

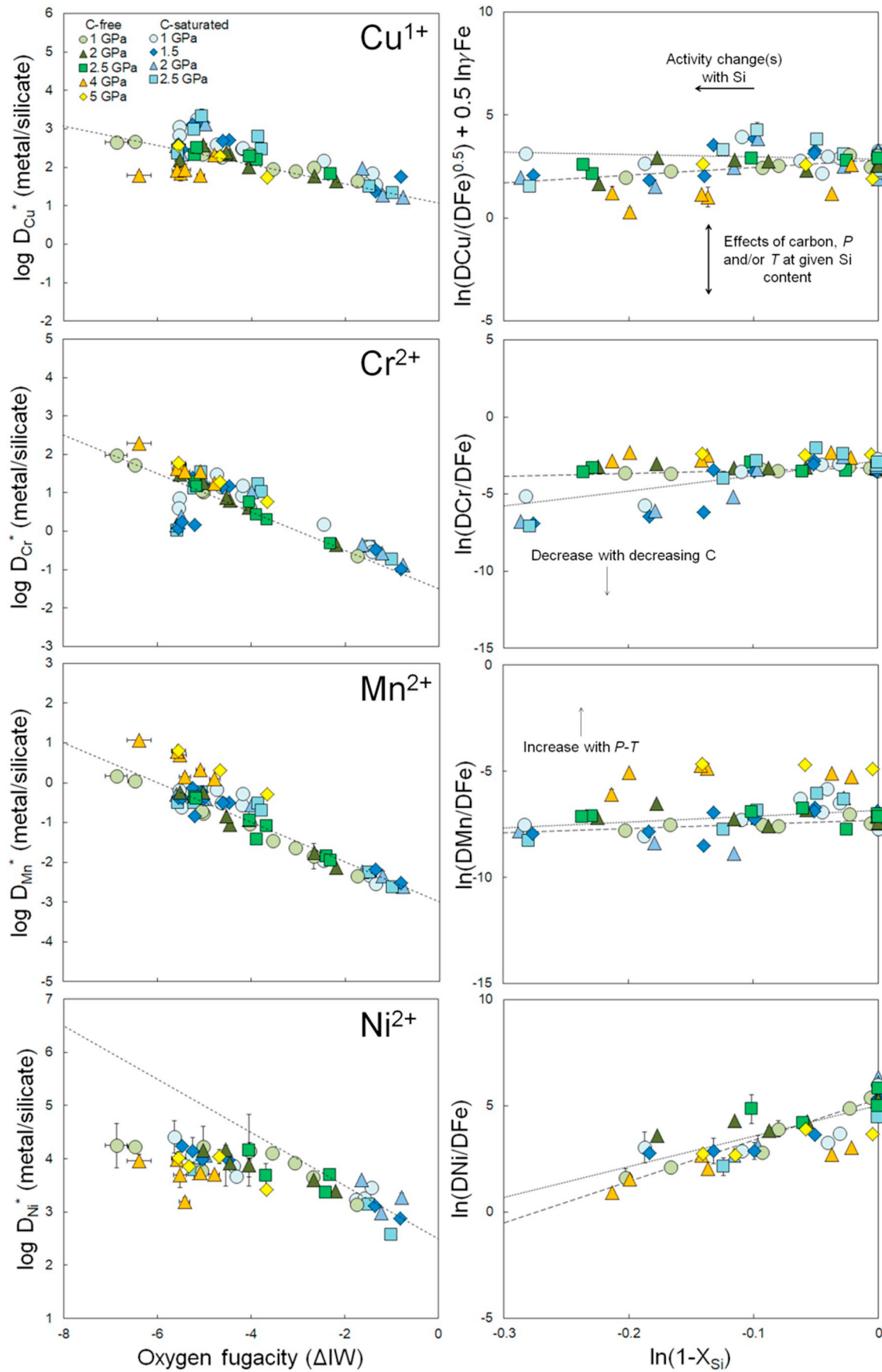
The valence for Cd is difficult to determine due to the strong effects of Si on its activity coefficient in Fe-rich alloys, but is likely 2+ given its geochemical similarities with Zn (Fig. 4). A 2+ valence state for Cd is therefore assumed throughout the study.

Ge and Sn may exist as 2+ and/or 4+ in silicate melts, depending on $f\text{O}_2$ and metal composition (Capobianco et al., 1999). The new experimental data are most consistent with a 2+ valence state for Sn (Fig. 4) which agrees with previous metal-silicate partitioning results at moderately reduced conditions (Capobianco et al., 1999; Vogel et al., 2018). The valence of Ge is also difficult to assess given the significant non-ideal behavior at reduced conditions. The new experimental data is most consistent with similar abundances of Ge^{2+} and Ge^{4+} (Fig. 4), which agrees with the findings of Siebert et al. (2011).

3.2.2. Trivalent and tetravalent elements: V, Ga, In, Sb, Ti, Si, Mo

The new results are most consistent with a 3+ valence state for V, Ga, In and Sb (Fig. 5). A 3+ valence state for V (Fig. 5) agrees with the previous work of Siebert et al. (2011), Steenstra et al. (2017b) and with XANES spectroscopic observations (Righter et al., 2006; Karner et al., 2008). A 3+ valence state for Ga would be consistent with most previous work (Capobianco et al., 1999; Righter and Drake, 2000; Righter et al., 2011; Siebert et al., 2011), although some workers reported a 2+ valence state (Corgne et al., 2008; Mann et al., 2009). Mann et al. (2009) proposed a 1+ valence state for In, but the data from this study is most consistent with a 3+ valence state (Fig. 5).

Due to the strong effects of Si on the activity of Sb in Si-bearing Fe-rich alloys, the dominant valence state of Sb in silicate melts is difficult to assess. A 3+ valence state is therefore assumed, as is suggested from the metal-silicate partitioning behavior of Sb at moderately reduced conditions (Vogel et al., 2018). The new metal-silicate partitioning data for Si is most consistent with a 4+ valence state (Fig. 6). For Ti, the valence state is difficult to determine (Vogel et al., 2018) and we therefore assume a 4+ valence state of Ti in the silicate melt. For Mo, a 4+ valence state is obtained (Fig. 6), which is in agreement with the



(caption on next page)

Fig. 3. Effects of variable oxygen fugacity on the metal-silicate partitioning behavior of Cu, Cr, Mn and Ni. Left panels show the $\log D_M^*$ (metal/silicate) values as a function of oxygen fugacity (fO_2) relative to the iron wüstite buffer (ΔIW) (see Table 1 and Section 3.2). In these plots dashed lines correspond to the expected slope related to the inferred valence(s) of the element. Negative deviations of D values from these slopes illustrate the negative effects of Si on trace element activities in Si-bearing Fe-rich metal alloys. Errors represent propagated errors assuming 2SE for EPMA and LA-ICP-MS analyses. Right panels show the effect of Si on $\ln K_M^D$ values of the elements considered, where $K_M^D = D_M^* / (D_{Fe}^*)^{n/2}$ (Eq. 2). The K_M^D values of non-divalent elements are corrected for different γ_{Fe}^{metal} , whereas all K_M^D values of the GGR6Si, GGR6Si-b, GGRFeSi and KBR6Si runs were corrected for non-ideal $\gamma_{FeO}^{silicate}$ (see Table 1 and Section 3.2). Dashed and finely dashed lines represent linear fits to C-free and C-saturated 1 GPa data, respectively. Errors on K_M^D values represent propagated errors assuming 2SE for EPMA and LA-ICP-MS analyses and are usually smaller than symbol size.

transition of Mo^{6+} to Mo^{4+} at conditions more reducing than $\Delta IW = -1$ previously observed in metal-silicate partitioning experiments (Steenstra et al., 2017a) and XANES measurements (Richter et al., 2016).

3.2.3. Pentavalent and hexavalent elements: P, As, W

The new metal-silicate partitioning data is in agreement with previous observations and predictions of a 5+ valence state of P in silicate melts (Corgne et al., 2008; Siebert et al., 2011; Vogel et al., 2018) (Fig. 7). Due to the very strong effects of Si on the activity of As in Fe-rich metallic alloys, its predominant valence state in silicate melts cannot be derived in this study (Fig. 7). A 5+ valence state for As is therefore assumed (Siebert et al., 2011).

The new data imply a 6+ valence state for W (Fig. 7); no evidence for W^{4+} was found. This is in excellent agreement with previous studies that constrained the metal-silicate partitioning behavior of W under a wider range of pressures, temperatures and/or compositions (Cottrell et al., 2009a, 2009b; Siebert et al., 2011; Wade et al., 2012, 2013). The ideal behaviour of many elements, especially those with higher valences, changes at conditions more reducing than $\Delta IW = -3$ to -4 , where Si starts to partition significantly into metal. As detailed below, this is related to the effects of Si on their activity coefficients in Fe-rich alloys, which will be discussed in Section 3.3.

3.2.4. Selenium and tellurium

The metal-silicate partitioning behaviour of Se and Te also varies strongly as a function of fO_2 . The new data confirms the previously proposed parabolic dependency of Se and Te with fO_2 , which is related to changes in their activity with different FeO contents of the silicate melt (Rose-Weston et al., 2009; Steenstra et al., 2017b, 2018). This behavior results in Se and Te behaving lithophile at conditions more reducing than $\sim \Delta IW -5$ (Fig. 8). Such a dependency has also been found for S which behaves geochemically similar to Se and Te (e.g. Kilburn and Wood, 1997; Rose-Weston et al., 2009). The new results also confirm that, independent of P - T and/or fO_2 , Te always behaves more siderophile than Se.

3.3. The effects of Si on metal-silicate partitioning of siderophile elements

The right panels in Figs. 3–8 illustrate the effects of Si on K_M^D . Note that the well-defined and consistent trends of K_M^D values versus $1 - x_{Si}^{metal}$ for C-saturated experiments show that the variability in $\gamma_{FeO}^{silicate}$ at very reducing conditions was accurately quantified. All elements considered here behave less siderophile with increasing x_{Si}^{metal} , i.e. their activities in the metal are lowered, which is reflected by positive ϵ_M^{Si} values (Table 6). A notable exception could be Cu, for which its siderophile behavior possibly shows a positive dependency with increasing Si. Fig. 9 shows the 1 GPa interaction coefficients or epsilon values (ϵ_M^{Si}) derived for each element for C-free systems. The ϵ_M^{Si} values for C-saturated systems (Table 6) were not considered in the plot, as the addition of C enlarges the uncertainties on derived ϵ_M^{Si} values (Table 6). Ideally, ϵ_M^{Si} values of C-free and C-saturated systems should be identical if all interaction parameters are properly accounted

for. However, the effects of C on the activities of many trace elements are not fully constrained, resulting in discrepancies between both sets of parameters. As is expected from consideration of Eq. (8), the effects of Si on trace element activities generally increase with increasing valence state of the element considered, as defined by Eqs. (5,8) (Fig. 9; Vogel et al., 2018). The siderophile behavior of As is most strongly decreased with increasing Si, reflected by the high ϵ_{As}^{Si} value (Fig. 9; Table 6).

The results for the other elements generally agree well with previous proposed values obtained at similar pressures (Tuff et al., 2011; Richter et al., 2017, 2018), whereas the 11 GPa values of Vogel et al. (2018) are consistently lower than the ϵ_M^{Si} values derived here, most notably for Sb and As (Fig. 9). However, no positive effects of Si on the siderophile behavior of Mn and V are observed as recently proposed by Richter et al. (2018). The difference between the ϵ_{Mo}^{Si} value for C-saturated systems reported by Richter et al. (2016) and the value found here is likely related to the limited range of Si contents explored by Richter et al. (2016), relative to the wider range considered here.

4. Discussion

4.1. Are interaction coefficients dependent on pressure?

Previous studies have shown that structural transitions occur in FeS, FeC and FeSi alloys at higher pressures (e.g. Morard et al., 2007; Sanloup et al., 2011; Shibasaki et al., 2015 and references therein). These transitions have been proposed to result in distinctly different pressure dependencies (i.e. < 5 versus 5 GPa) of the metal-silicate partitioning behavior of several elements, including Ni and Co (Kegler et al., 2008; Sanloup et al., 2011). Besides the direct effects of structural transitions on pressure dependencies of siderophile element partitioning, such transitions could also affect the thermodynamic activities of trace elements. In the case of terrestrial core formation models, low pressure metal-silicate partitioning data and thermodynamic activity models are often extrapolated to much higher pressures. This could result in erroneous results, if ϵ_M^{Si} values are not constant with pressure. The new data can be used to assess the possible effects of pressure on the ϵ_M^{Si} values of the elements considered. To assess pressure effects, we only use ϵ_M^{Si} values derived from the C-free series, given the larger uncertainties on ϵ_M^{Si} values for C-saturated systems.

Fig. 10 shows the derived interaction coefficients or ϵ_M^{Si} values for C-free systems from this study and Vogel et al. (2018) as a function of pressure. The first important observation is that for all elements an initial decrease of ϵ_M^{Si} is observed. For elements Si, Sn, In and possibly V, Ni, As and Sb an overall decrease of ϵ_M^{Si} is observed between 1 and 4 or 11 GPa. For example, the ϵ_{As}^{Si} value is decreased by $> 50\%$ between 1 and 11 GPa. In the case of the other elements and possibly V, Ni, As and Sb, a small increase of ϵ_M^{Si} may be observed after the initial decrease of ϵ_M^{Si} between 1 and 2 GPa. These results show that ϵ_M^{Si} values are not constant with pressure and that this can result in significant uncertainties if extrapolated to much higher pressures (i.e. the pressures relevant to terrestrial core formation).

The observed variability in ϵ_M^{Si} as a function of pressure could be the result of a decrease of γ_{Fe}^{metal} with pressure. However, to obtain a

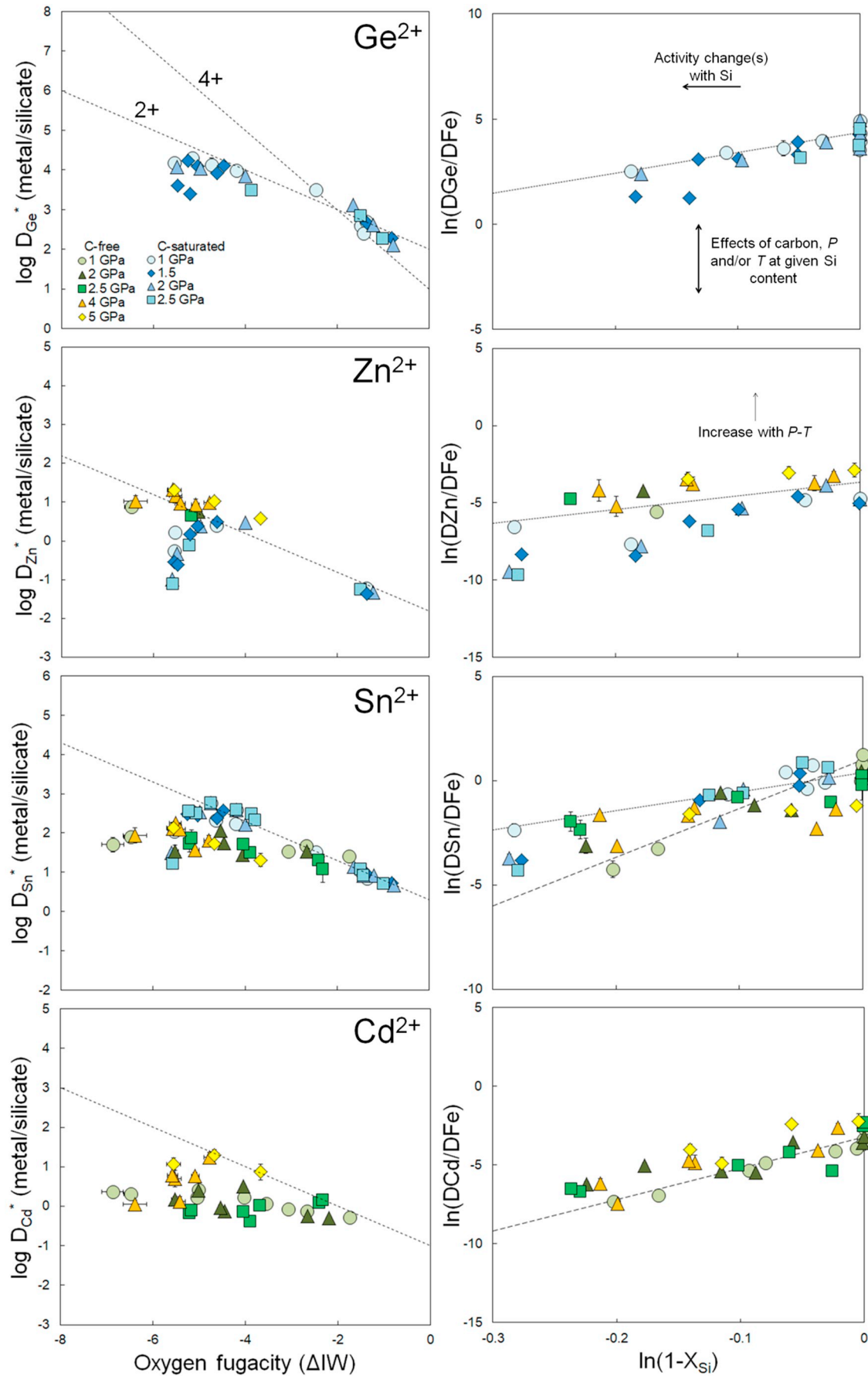


Fig. 4. Effects of variable oxygen fugacity and Si contents in metal on the metal-silicate partitioning behavior of Ge, Zn, Sn and Cd. See Fig. 3 caption for additional details.

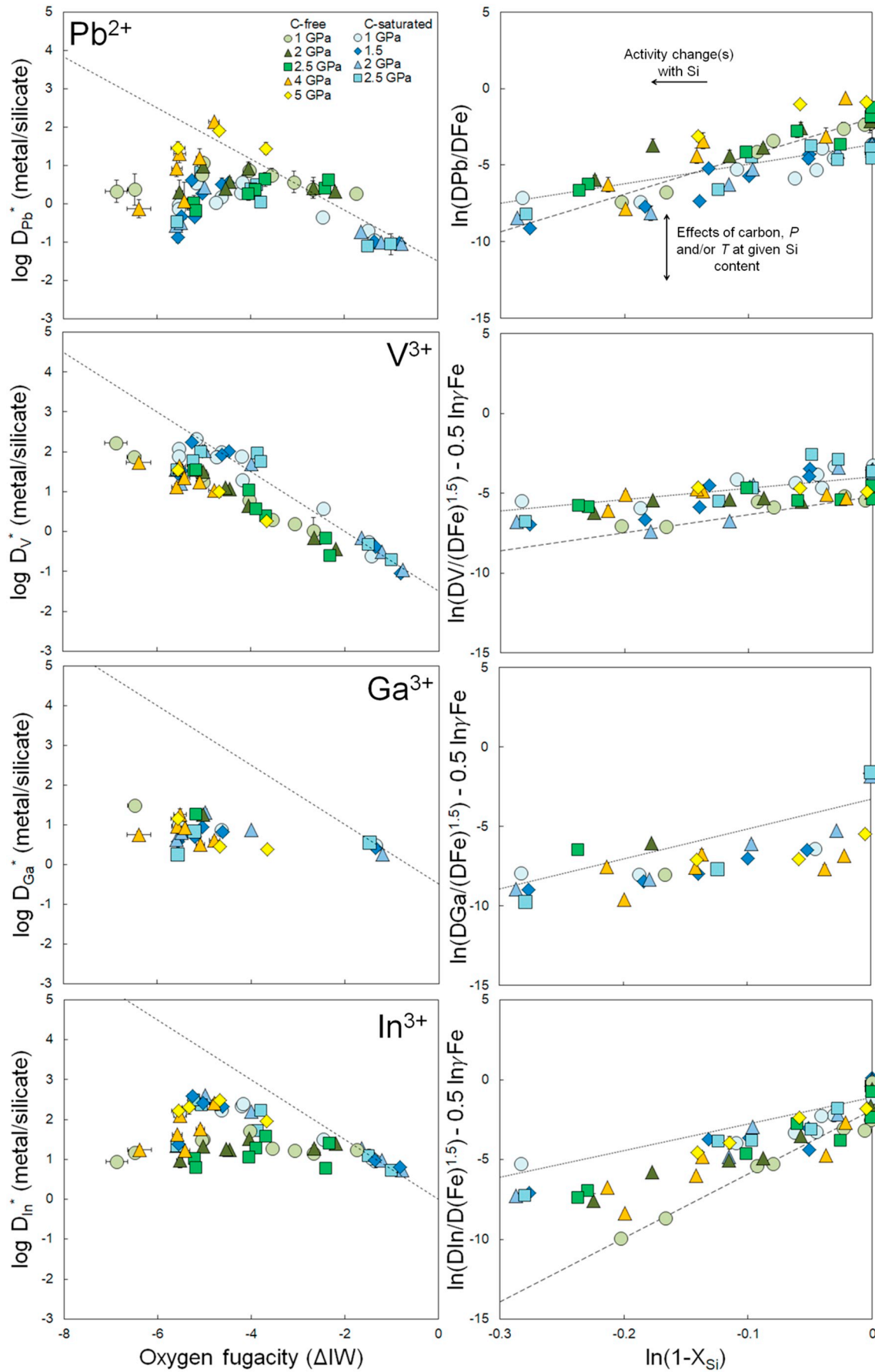


Fig. 5. Effects of variable oxygen fugacity and Si contents in metal on the metal-silicate partitioning behavior of Pb, V, Ga and In. See Fig. 3 caption for additional details.

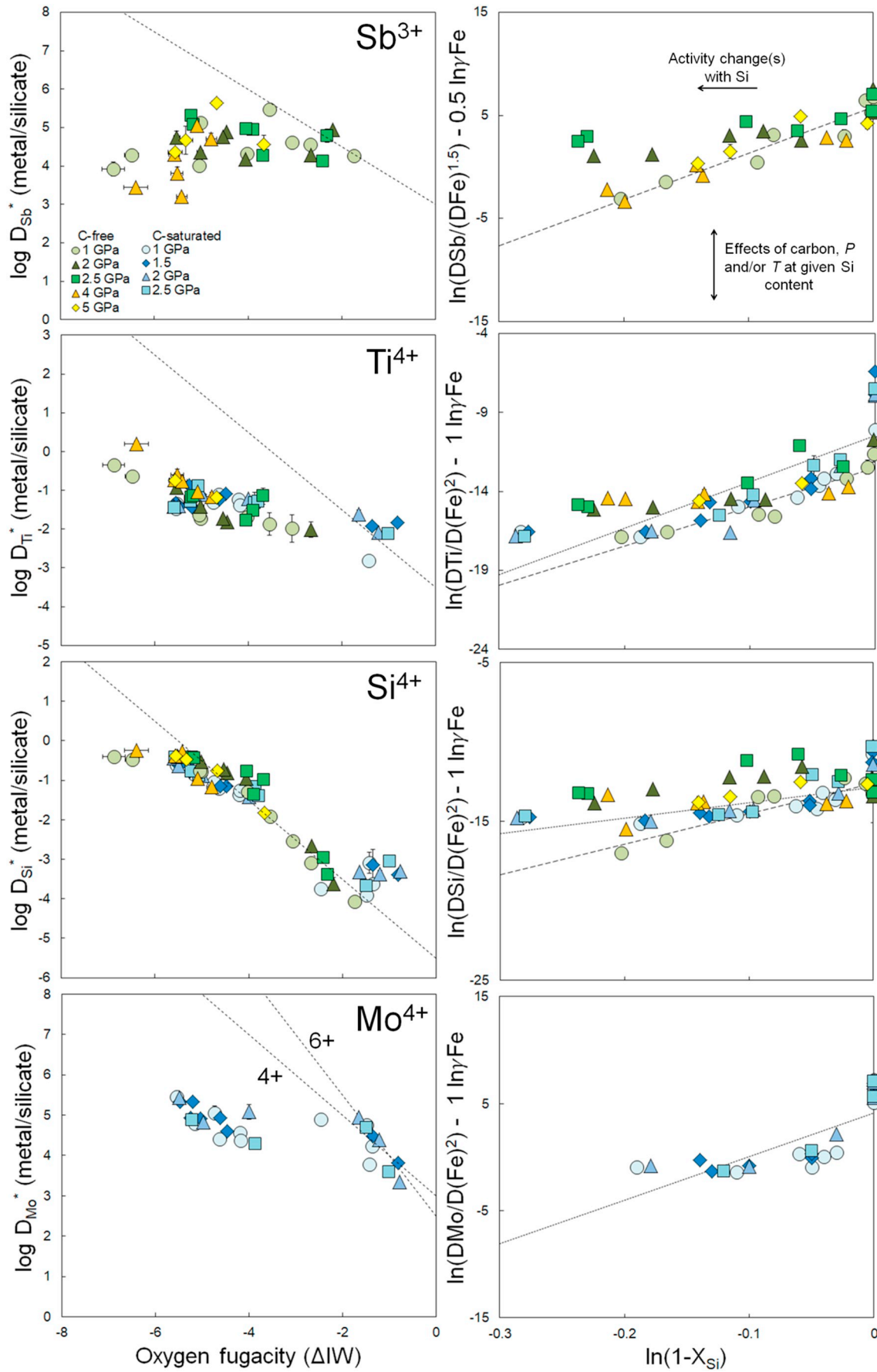


Fig. 6. Effects of variable oxygen fugacity and Si contents in metal on the metal-silicate partitioning behavior of Sb, Ti, Si and Mo. See Fig. 3 caption for additional details.

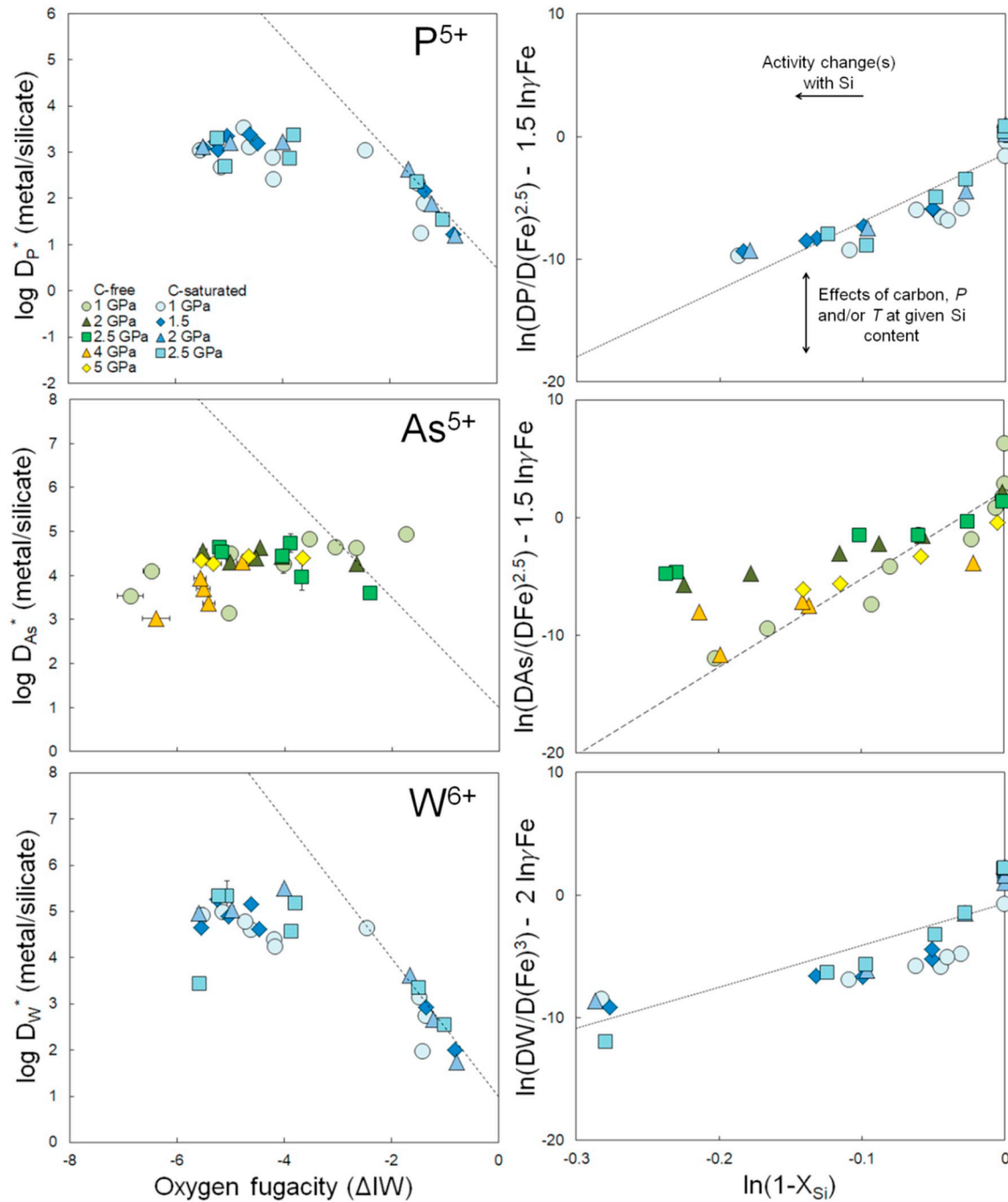


Fig. 7. Effects of variable oxygen fugacity and Si contents in metal on the metal-silicate partitioning behavior of P, As and W. See Fig. 3 caption for additional details.

1 GPa ϵ_{As}^{Si} value close to higher pressure ϵ_{As}^{Si} values, the γ_{Fe}^{metal} should decrease by about a factor of 4 to 5, which seems unlikely given previously proposed effects of Si on γ_{Fe}^{metal} (Bouchard and Bale, 1995; Tuff et al., 2011). In addition, consideration of Eq. (8) implies that divalent elements should remain unaffected by changes in γ_{Fe}^{metal} , whereas the ϵ_M^{Si} values of divalent elements such as Ni, Pb and Sn show similar dependencies as observed for higher or lower valence elements. It is therefore concluded that the observed variations in ϵ_M^{Si} with pressure must be a result of direct pressure effects on ϵ_M^{Si} , perhaps due to

structural transitions in FeSi-alloys within the 1 to 4 GPa range (Shibazaki et al., 2015). Wang et al. (2016) also reported experimental evidence that pressure affects ϵ_M^S values. They found that at pressures of 20 GPa, Zn, Cd and In behave less siderophile with increasing S – opposite of the trend found at low pressures (Wood et al., 2014) – and linked this to a major structural transition in Fe-FeS melts near 15 GPa (Morard et al., 2007). It could also be related to structural changes in the silicate melt occurring at lower pressures (e.g. Lee et al., 2003 and references therein) and the corresponding effects on the activity

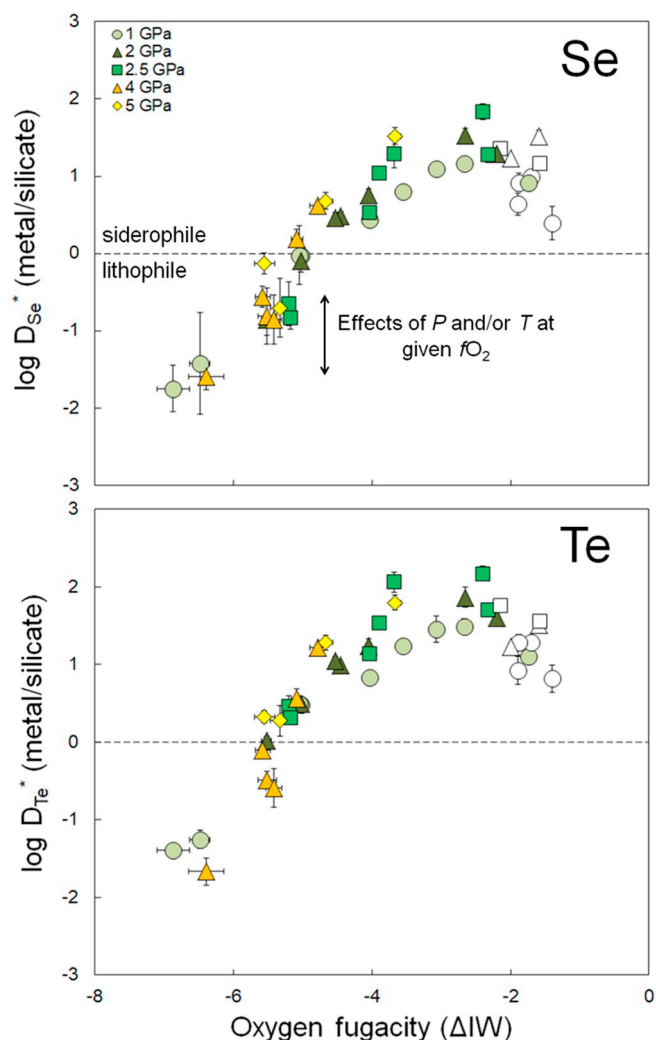


Fig. 8. Effects of variable oxygen fugacity on the metal-silicate partitioning behavior of Se and Te for C-free experiments only. Horizontal dashed line represents the transition from lithophile to siderophile behavior of Se and Te. Errors on $\log D_M^*$ values represent propagated errors assuming 2SE for EPMA and LA-ICP-MS analyses and are usually smaller than symbol size. Open symbols represent C and S-free experiments from Steenstra et al. (2017b).

coefficient of the cation in question. Future studies should additionally constrain ϵ_M^{Si} values at higher pressures (> 5 GPa) so that the pressure evolution of ϵ_M^{Si} can be modelled and implemented in future terrestrial core formation models.

4.2. Highly reduced planetary differentiation and volatile element depletions

Planetary cores have been proposed to act as significant reservoirs for volatile elements, depending on their compositions and/or P - T conditions of core formation (e.g. Wood and Halliday, 2010; Steenstra et al., 2017b; Righter et al., 2017, 2018). These new results can be used to qualitatively assess the potential of planetary cores as a major reservoir for volatile elements in reduced bodies. Despite the negative effects of core Si contents on volatile element partitioning (i.e. positive

ϵ_M^{Si} values), the overall increase of their siderophile behavior with more reducing conditions still results in significant partitioning of volatiles into planetary cores.

In the case of reduced achondrites such as the aubrite meteorite suite, a significant degree of volatile element depletion may be explained by segregating Fe–Si metal during core formation. For example, core formation in the AuPB at $\Delta\text{IW} = -5$ (Casanova et al., 1993) and 1883 K would yield metal-silicate partition coefficients of 1 to 10 for volatile elements Zn, Cd and Pb, 10 to 500 for In, 50 to 1000 for Sn, 100 to 1000 for Cu and 10,000 to 100,000 for As and Sb (Figs. 3–9). Core formation in the AuPB would therefore significantly deplete these elements in its mantle by core formation alone. Volatile elements Se and Te would not be depleted by this process. Their depletions in reduced achondrites may therefore provide insights into other mechanisms such as sulfide segregation and/or planetary volatile loss.

These new experimental results also have implications for the distribution of C in reduced planetary bodies. We confirmed that C solubility is strongly decreased with increasing Si contents, so that the overall bulk of the C inventory of undifferentiated reduced bodies will be expelled to its mantle (see Appendix Section A.4 for a revised empirical model). A significant part of the bulk planet C inventory could in turn degas and/or form a graphitic flotation crust, as proposed for Mercury (Vander Kaaden and McCubbin, 2015). It also has implications for core Si contents. A C-saturated mantle would result in lower core Si contents, which in turn would affect the extent of Si – siderophile element interactions in the core.

5. Conclusions

The metal-silicate partitioning behaviour of 21 siderophile and nominally lithophile elements was studied as a function of $f\text{O}_2$ and Si content of the metal. Using the new data, siderophile element valences in silicate melts were determined across a wide $f\text{O}_2$ range and mostly agree with previous work. Increasing Si in the metal results in a decrease of the activities of all siderophile elements considered here, resulting in less siderophile behaviour and in lower-than-expected metal-silicate partition coefficients given estimated valence state(s). Most of the newly derived 1 GPa interaction coefficients agree well with previously reported interaction coefficients (ϵ_M^{Si}) obtained at comparable pressures. However, we found that the ϵ_M^{Si} values of all elements systematically change with pressure between 1 and 4 GPa. These results show that caution should be taken when extrapolating low pressure thermodynamic parameters to much higher pressure terrestrial core formation scenarios.

It is concluded that core formation in reduced planetary bodies will significantly deplete the majority of the volatile elements considered here. These effects should be taken into account in future studies of volatile depletion patterns of reduced achondrites. The new results presented here provide an internally consistent dataset for future applications of siderophile element systematics in (highly) reduced bodies.

Acknowledgements

This work was supported by a Netherlands Organization for Scientific Research (N.W.O.) Vici award to W.v.W. and by the German Research Foundation grant SFB TRR-170. We thank M. Duncan for providing the Fe_3C standard. We thank John Wade and four anonymous reviewers for their helpful comments on previous versions of this manuscript that greatly improved the quality of this work.

Table 6

Interaction coefficients or ϵ_M^{Si} for siderophile elements in Fe–Si alloys at 1873–2273 K and various pressures. Errors are in round brackets in terms of least digits cited (i.e. 3.4(30) = 3.4 ± 3.0 ; 16(4) = 16 ± 4).

This study	N	R^2	N	R^2	N	R^2	N	R^2	N	R^2	N	R^2
Pressure (GPa)	1		1.5		2		2.5		4			
Cu ¹⁺ (C-sat)	−1.5(21)	8	0.07	3.4(30)	9	0.16	2.2(32)	7	0.08	2.8(42)	7	0.08
Cu ¹⁺ (C-free)	3.7(28)	9	0.67	–	–	–	1.6(22)	7	0.10	2.2(10)	5	0.64
Cr ²⁺ (C-sat)	9.7(19)	8	0.81	16(4)	9	0.73	13(2)	6	0.91	15(3)	7	0.80
Cr ²⁺ (C-free)	1.9(5)	9	0.64	–	–	–	−0.7(4)	7	0.34	0.4(10)	7	0.03
Mn ²⁺ (C-sat)	1.4(18)	8	0.09	4.7(18)	9	0.48	3.7(20)	7	0.40	5.0(28)	7	0.39
Mn ²⁺ (C-free)	2.0(7)	9	0.54	–	–	–	−1.4(18)	7	0.10	−0.3(13)	7	0.01
Ni ²⁺ (C-sat)	13(5)	5	0.69	15(3)	6	0.83	29(8)	4	0.88	22(5)	3	0.95
Ni ²⁺ (C-free)	19(1)	9	0.96	–	–	–	9.2(22)	6	0.82	7.9(77)	4	0.35
Ge ²⁺ (C-sat)	9.7(20)	6	0.85	15(3)	8	0.80	11(3)	6	0.78	20(14)	3	0.67
Zn ²⁺ (C-sat)	8.9(47)	4	0.64	15(4)	6	0.81	19(6)	4	0.84	17(1)	3	0.99
Zn ²⁺ (C-free)	–	–	–	–	–	–	–	–	–	–	–	–
Sn ²⁺ (C-sat)	9.0(6)	7	0.98	15(2)	7	0.95	14(1)	6	0.98	16(2)	6	0.93
Sn ²⁺ (C-free)	23(3)	5	0.97	–	–	–	14(4)	5	0.77	8.9(18)	6	0.85
Cd ²⁺ (C-free)	20(2)	9	0.95	–	–	–	12(3)	7	0.75	15(4)	7	0.74
Pb ²⁺ (C-sat)	13(2)	8	0.87	20(2)	9	0.91	18(2)	7	0.93	15(3)	7	0.82
Pb ²⁺ (C-free)	25(2)	9	0.97	–	–	–	14(3)	7	0.83	18(3)	7	0.89
V ³⁺ (C-sat)	8.7(17)	8	0.81	13(2)	9	0.83	14(3)	7	0.82	12(2)	6	0.88
V ³⁺ (C-free)	11(2)	8	0.90	–	–	–	4.7(11)	7	0.77	3.0(18)	7	0.37
Ga ³⁺ (C-sat)	19(10)	4	0.65	23(7)	6	0.71	31(9)	4	0.84	28(10)	3	0.89
Ga ³⁺ (C-free)	–	–	–	–	–	–	–	–	–	–	–	–
In ³⁺ (C-sat)	16(4)	7	0.79	24(3)	6	0.93	24(2)	6	0.97	24(3)	7	0.94
In ³⁺ (C-free)	40(4)	9	0.94	–	–	–	28(3)	7	0.93	23(3)	7	0.90
Sb ³⁺ (C-free)	45(5)	9	0.93	–	–	–	24(6)	7	0.77	13(4)	7	0.70
Ti ⁴⁺ (C-sat)	20(5)	7	0.75	26(8)	8	0.66	31(8)	6	0.78	28(9)	6	0.72
Ti ⁴⁺ (C-free)	25(4)	7	0.89	–	–	–	19(6)	5	0.76	15(4)	5	0.80
Si ⁴⁺ (C-sat)	9.8(40)	8	0.50	15(5)	9	0.60	14(4)	7	0.68	14(7)	5	0.56
Si ⁴⁺ (C-free)	19(3)	9	0.83	–	–	–	4.3(39)	7	0.20	3.8(41)	7	0.14
Mo ⁴⁺ (C-sat)	40(16)	7	0.56	52(14)	7	0.72	45(13)	6	0.76	64(18)	4	0.86
P ⁵⁺ (C-sat)	55(14)	7	0.75	53(9)	8	0.84	57(11)	6	0.87	76(13)	6	0.90
As ⁵⁺ (C-free)	75(10)	9	0.89	–	–	–	33(4)	6	0.94	23(2)	6	0.96
W ⁶⁺ (C-sat)	34(12)	7	0.60	37(10)	7	0.71	36(8)	6	0.83	49(6)	7	0.92

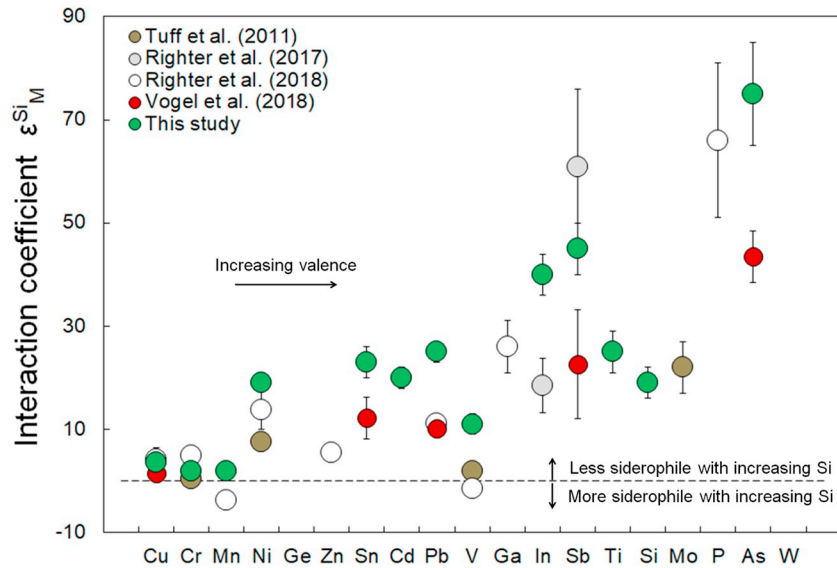


Fig. 9. Interaction coefficients or epsilon values (ϵ_M^{Si}) of siderophile elements in Si-bearing Fe-rich metals that were derived in this study at 1 GPa and 1883 K for C-free Fe(Si) alloys (see also Table 6). Errors represent 2 SE. Valence states of elements increases to the right. Horizontal line represents the transition from less or more siderophile behavior of element M with increasing Si. Plotted for comparison are values from Tuff et al. (2011) obtained at 1 GPa and 1923 K; values from Righter et al. (2017, 2018) for C-free systems obtained at 1 GPa and 1873 K and ϵ_M^{Si} values from Vogel et al., 2018) obtained at 11 GPa and 2600 K, normalized to the reference temperature of 1873 K.

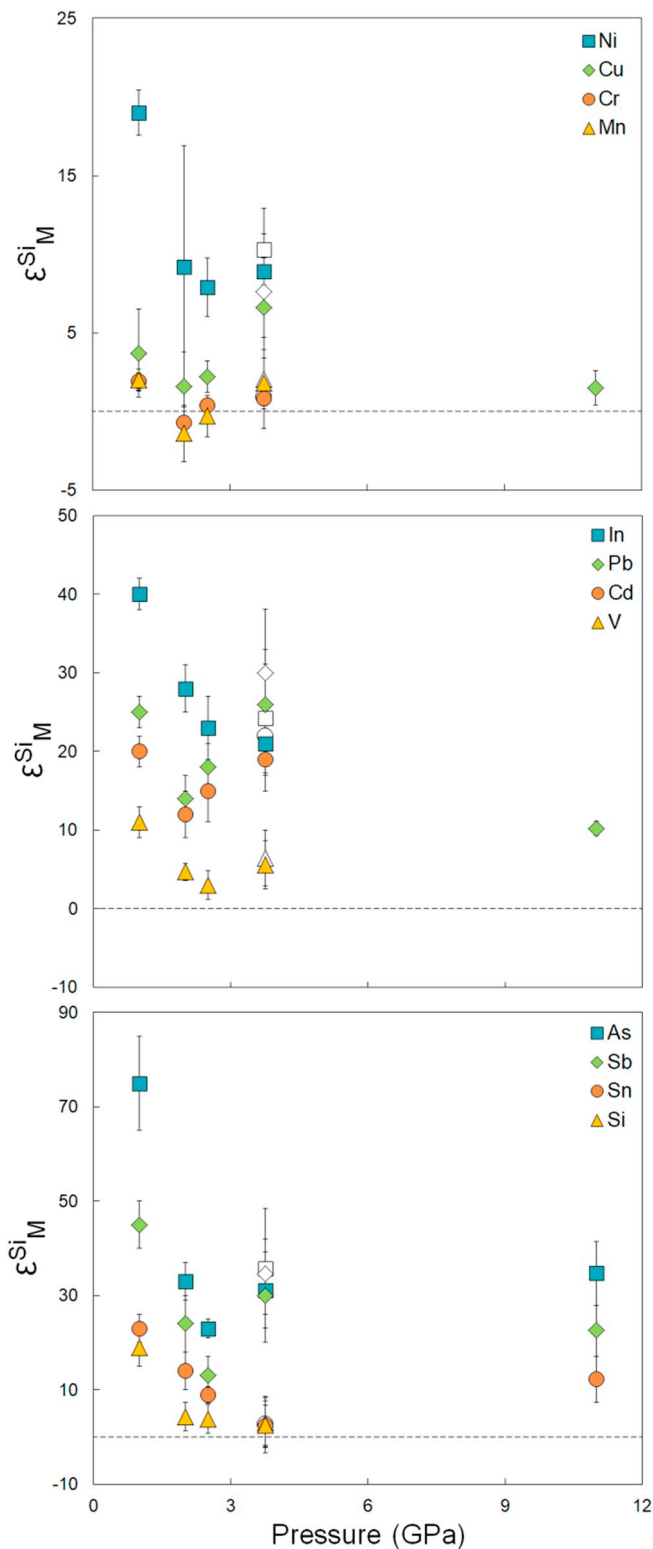


Fig. 10. Effects of pressure on ϵ_M^{Si} values for C-free experiments (see Section 4.1). The 1, 2 and 2.5 GPa values were derived at 1883 K, whereas 4 GPa values were obtained at 2173 K. The 11 GPa values were taken from Vogel et al. (2018), which were derived at 2600 K and corrected to 1873 K. The As^{3+} value of Vogel et al. (2018) was recalculated to As^{5+} . Open symbols at 4 GPa show values corrected to the reference temperature of 1883 K (see main text Table 2). Errors represent 1 SE.

Appendix A. Supplementary data

Supplementary data to this article can be found online at <https://doi.org/10.1016/j.icarus.2019.113391>.

References

- Armstrong, J.T., 1995. A package of correction programs for the quantitative electron microbeam X-ray analysis of thick polished materials, thin films, and particles. *Microbeam Analysis* 4, 177–200.
- Berry, A.J., O'Neill, H.St.C., Scott, D.R., Foran, G.J., Shelley, J.M.G., 2006. The effect of composition on $\text{Cr}^{2+}/\text{Cr}^{3+}$ in silicate melts. *Am. Mineral.* 91, 1901–1908.
- Bouchard, D., Bale, C.W., 1995. Simultaneous-optimization of thermochemical data for liquid-iron alloys containing C, N, Ti, Si, Mn, S, and P. *Metall. Mater. Trans. B Proc. Metall. Mater. Process. Sci.* 26, 467–484.
- Boyd, F.R., England, J.L., 1960. Apparatus for phase-equilibrium measurements at pressures up to 50 kilobars and temperatures up to 1750 °C. *J. Geophys. Res.* 65, 741–748.
- Brown, S.M., Elkins-Tanton, L.T., 2009. Composition of Mercury's earliest crust from magma ocean models. *Earth Planet. Sci. Lett.* 286, 446–455.
- Capobianco, C.J., Amelin, A.A., 1994. Metal-silicate partitioning of nickel and cobalt: the influence of temperature and oxygen fugacity. *Geochim. Cosmochim. Acta* 58, 125–140.
- Capobianco, C.J., Drake, M.J., de Aro, J., 1999. Siderophile geochemistry of Ga, Ge, and Sn: cationic oxidation states in silicate melts and the effects of composition in iron-nickel alloys. *Geochim. Cosmochim. Acta* 63, 2667–2677.
- Casanova, I., Keil, K., Newsom, H.E., 1993. Composition of metal in aubrites: constraints on core formation. *Geochim. Cosmochim. Acta* 57, 675–682.
- Chabot, N.L., Wollack, E.A., Klima, R.L., Minitti, M.E., 2014. Experimental constraints on Mercury's core composition. *Earth Planet. Sci. Lett.* 390, 199–208.
- Corgne, A., Keshav, S., Fei, Y., McDonough, W.F., 2007. How much potassium is in the Earth's core? New insights from partitioning experiments. *Earth Planet. Sci. Lett.* 256, 567–576.
- Corgne, A., Keshav, S., Wood, B.J., McDonough, W.F., Fei, Y., 2008. Metal-silicate partitioning and constraints on core composition and oxygen fugacity during Earth accretion. *Geochim. Cosmochim. Acta* 72, 574–589.
- Cottrell, E., Walter, M.J., Walker, D., 2009a. Metal-silicate partitioning of tungsten at high pressure and temperature: implications for equilibrium core formation in earth. *Earth Planet. Sci. Lett.* 281, 275–287.
- Cottrell, E., Walter, M.J., Walker, D., 2009b. Erratum to: “metal-silicate partitioning of tungsten at high pressure and temperature: implications for equilibrium core formation in Earth”. *Earth Planet. Sci. Lett.* 289, 631–634.
- Drake, M.J., Newsom, H.E., Capobianco, C.J., 1989. V, Cr, and Mn in the earth, moon, EPB and SPB and the origin of the Moon: experimental studies. *Geochim. Cosmochim. Acta* 53, 2101–2211.
- Griffin, W.L., Powell, W.J., Pearson, N.J., O'Reilly, S.Y., 2008. GLITTER: data reduction software for laser ablation ICP-MS. In: Sylvester, P. (Ed.), *Laser Ablation ICP-MS in the Earth Sciences*. vol. 40. pp. 308–311. Current Practices and Outstanding Issues., Mineralogical Association of Canada. Short Course Series.
- Hauck II, S.A., Margot, J.-L., Solomon, S.C., Phillips, R.J., Johnson, C.L., Lemoine, F.G., Mazarico, E., McCoy, T.J., Padovan, S., Peale, S.J., Perry, M.E., Smith, D.E., Zuber, M.T., 2013. The curious case of Mercury's internal structure. *J. Geophys. Res. Planets* 118, 1204–1220.
- Holzheid, A., Lodders, K., 2001. Solubility of copper in silicate melts as function of oxygen and sulfur fugacities, temperature, and silicate composition. *GCA* 65, 1933–1951.
- Jochum, K.P., Nohl, U., Herwig, K., Lammel, E., Stoll, B., Hofmann, A.W., 2005. GeoReM: a new geochemical database for reference materials and isotopic standards. *Geost. Geoanal. Res.* 29, 333–338.
- Karner, J.M., Papike, J.J., Sutton, S.R., Shearer, C.K., Burger, P., McKay, G., Le, L., 2008. Valence state partitioning of V between pyroxene-melt: effects of pyroxene and melt composition, and direct determination of V valence states by XANES. Application to Martian basalt QUE 94201 composition. *Meteorit. Planet. Sci.* 43, 1275–1285.
- Kegler, P.A., Holzheid, D.J., Frost, D., Rubie, C., Dohmen, R., Palme, H., 2008. New Ni and Co metal-silicate partitioning data and their relevance for an early terrestrial magma ocean. *Earth Planet. Sci. Lett.* 268, 28–40.
- Kilburn, M.R., Wood, B.J., 1997. Metal-silicate partitioning and the incompatibility of S and Si during core formation. *Earth Planet. Sci. Lett.* 152, 139–148.
- Knibbe, J.S., van Westrenen, W., 2015. The interior configuration of planet mercury constrained by moment of inertia and planetary contraction. *J. Geophys. Res.: Planets* 120, 1904–1923.
- Lee, S.K., Fei, Y., Cody, G.D., Mysen, B.O., 2003. Order and disorder in sodium silicate glasses and melts at 10 GPa. *Geophys. Res. Lett.* 30, 1845.
- Li, Y., Dasgupta, R., Tsuno, K., Monteleone, B., Shimizu, N., 2016. Carbon and sulfur budget of the silicate Earth explained by accretion of differentiated planetary embryos. *Nat. Geosci.* 9, 781–785.
- Liu, J., Li, J., Ikuta, D., 2016. Elastic softening in Fe_7C_3 with implications for Earth's deep carbon reservoirs. *J. Geophys. Res. Solid Earth* 121, 1514–1524.
- Malavergne, V., Toplis, M.J., Berthet, S., Jones, J., 2010. Highly reducing conditions during core formation on Mercury: implications for internal structure and the origin of a magnetic field. *Icarus* 206, 199–209.
- Malavergne, V., Cordier, P., Richter, K., Brunet, F., Zanda, G., 2014. How mercury can be the most reduced terrestrial planet and still store iron in its mantle. *Earth Planet. Sci. Lett.* 394, 186–197.
- Mann, U., Frost, D.J., Rubie, D.C., 2009. Evidence for high-pressure core-mantle

- differentiation from the metal-silicate partitioning of lithophile and weakly-siderophile elements. *Geochim. Cosmochim. Acta* 73, 7360–7386.
- McCubbin, F.M., Riner, M.A., Vander Kaaden, K.E., Burkemper, L.K., 2012. Is Mercury a volatile-rich planet? *Geophys. Res. Lett.* 39, L09202.
- Morard, G., Sanloup, C., Fiquet, G., Mezouar, M., Rey, N., Poloni, R., Beck, P., 2007. Structure of eutectic Fe-FeS melts to pressures up to 17 GPa – implications for planetary cores. *Earth Planet. Sci. Lett.* 263, 128–139.
- Namur, O., Charlier, B., Holtz, F., Cartier, C., McCammon, C., 2016. Sulfur solubility in reduced mafic silicate melts: implications for the speciation and distribution of sulfur on Mercury. *Earth Planet. Sci. Lett.* 448, 102–114.
- Nittler, L.R., Chabot, N.L., Grove, T.L., Peplowski, P.N., 2019. The chemical composition of Mercury. *Mercury: The View after MESSENGER*, Cambridge University Press, Chapter 2, 30–51.
- Rai, N., van Westrenen, W., 2013. Core-mantle differentiation in Mars. *J. Geophys. Res.: Planets* 118, 1195–1203.
- Rai, N., van Westrenen, W., 2014. Lunar core formation: new constraints from metal-silicate partitioning of siderophile elements. *Earth Planet. Sci. Lett.* 388, 343–352.
- Ricolleau, A., Fei, Y., Corgne, A., Siebert, J., Badro, J., 2011. Oxygen and silicon contents of Earth's core from high pressure metal-silicate partitioning experiments. *Earth Planet. Sci. Lett.* 310, 409–421.
- Righter, K., Drake, M.J., 2000. Metal/silicate equilibrium in the early Earth – new constraints from the volatile moderately siderophile elements Ga, Cu, P, and Sn. *Geochim. Cosmochim. Acta* 64, 3581–3597.
- Righter, K., Sutton, S.R., Newville, M., Lei, L., Schwandt, C.S., Uchida, H., Lavina, B., Downs, R.T., 2006. An experimental study of the oxidation state of vanadium in spinel and basaltic melt with implications for the origin of planetary basalt. *Am. Mineral.* 91, 1643–1656.
- Righter, K., King, C., Danielson, L., Pando, K., Lee, C.-T., 2011. Experimental determination of the metal/silicate partition coefficient of germanium: implications for core and mantle differentiation. *Earth Planet. Sci. Lett.* 304, 379–388.
- Righter, K., Danielson, L.R., Pando, K.M., Shofner, G.A., Sutton, S.R., Newville, M., Lee, C.-T., 2016. Valence and metal/silicate partitioning of Mo: implications for conditions of Earth accretion and core formation. *Earth Planet. Sci. Lett.* 437, 89–100.
- Righter, K., Nickodem, K., Pando, K., Danielson, L., Boujibar, A., Righter, M., Lapen, T.J., 2017. Distribution of Sb, As, Ge, and In between metal and silicate during accretion and core formation in the Earth. *Geochim. Cosmochim. Acta* 198, 1–16.
- Righter, K., Pando, K., Humayun, M., Waesemann, N., Yang, S., Boujibar, A., Danielson, L.R., 2018. Effect of silicon on activity coefficients of Siderophile elements (Au, Pd, Pt, P, Ga, Cu, Zn, and Pb) in liquid Fe: roles of core formation, late sulfide matte, and late veneer in shaping terrestrial mantle geochemistry. *Geochim. Cosmochim. Acta* 232, 101–123.
- Robaut, F., Crisci, A., Durand-Charre, M., Jouanne, D., 2006. Practical aspects of carbon content determination in carburized steels by EPMA. *Microsc. Microanal.* 12, 331–334.
- Rose-Weston, L., Brenan, J.M., Fei, Y., Secco, R.A., Frost, D.J., 2009. Effect of pressure, temperature, and oxygen fugacity on the metal-silicate partitioning of Te, Se, and Si: implications for earth differentiation. *Geochim. Cosmochim. Acta* 73, 4598–4615.
- Rubie, D.C., Jacobson, S.A., Morbidelli, A., O'Brien, D.P., Young, E.D., de Vries, J., Nimmo, F., Palme, H., Frost, D.J., 2015. Accretion and differentiation of the terrestrial planets with implications for the compositions of early-formed solar system bodies and accretion of water. *Icarus* 248, 89–108.
- Sanloup, C., van Westrenen, W., Dasgupta, R., Maynard-Casely, H., Perrillat, J.-P., 2011. Compressibility change in iron-rich melt and implications for core formation models. *Earth Planet. Sci. Lett.* 306, 118–122.
- Schmitt, W., Palme, H., Wänke, H., 1989. Experimental determination of metal/silicate partition coefficients for P, Co, Ni, Cu, Ga, Ge, Mo, and W and some implications for the early evolution of the Earth. *Geochim. Cosmochim. Acta* 53, 173–185.
- Shibazaki, Y., Kono, Y., Fei, Y., 2015. Microscopic structural change in a liquid Fe-C alloy of ~5 GPa. *Geophys. Res. Lett.* 42, 5236–5242.
- Siebert, J., Corgne, A., Ryerson, F.J., 2011. Systematics of metal-silicate partitioning for many siderophile elements applied to Earth's core formation. *Geochim. Cosmochim. Acta* 75, 1451–1489.
- Steenstra, E.S., Knibbe, J.S., Rai, N., van Westrenen, W., 2016. Constraints on core formation in Vesta from metal-silicate partitioning of siderophile elements. *Geochim. Cosmochim. Acta* 177, 48–61.
- Steenstra, E.S., Sitabi, A.B., Lin, Y.H., Rai, N., Berndt, J., Matveev, S., van Westrenen, W., 2017a. The effect of melt composition on metal-silicate partitioning of siderophile elements and constraints on core formation in the angrite parent body. *Geochim. Cosmochim. Acta* 212, 62–83.
- Steenstra, E.S., Lin, Y.H., Dankers, D., Rai, N., Berndt, J., Matveev, S., van Westrenen, W., 2017b. The lunar core can be a major reservoir for volatile elements S, Se, Te and Sb. *Sci. Rep.* 7, 14552.
- Steenstra, E.S., Seegers, A.X., Eising, J., Tomassen, B.G.J., Webers, F.P.F., Berndt, J., Klemme, S., Matveev, S., van Westrenen, W., 2018. Evidence for a sulfur-under-saturated lunar interior from the solubility of sulfur in lunar melts and sulfide-silicate partitioning of siderophile elements. *Geochim. Cosmochim. Acta* 231, 130–156.
- Steenstra, E.S., Berndt, J., Klemme, S., van Westrenen, W., 2019. LA-ICP-MS analyses of Fe-rich alloys: quantification of matrix effects for 193 nm excimer laser systems. *J. Analytical Atom. Spectrometry* 34, 222–231.
- Stolyarova, V.L., Lopatin, S.I., Stolyar, S.V., 2003. Determination of the SiO₂ activity in melts of the CaO-Al₂O₃-SiO₂ system by high-temperature mass spectrometry. *Glas. Phys. Chem.* 29, 451–455.
- Tuff, J., Wood, B.J., Wade, J.W., 2011. The effect of Si on metal-silicate partitioning of siderophile elements and implications for the conditions of core formation. *Geochim. Cosmochim. Acta* 75 (680), 673–690.
- van Achterbergh, E., Ryan, C.G., Jackson, S.E., Griffin, W.L., 2001. Data reduction software for LA-ICP-MS: appendix. In: Sylvester, P.J. (Ed.), *Laser Ablation-ICP Mass Spectrometry in the Earth Sciences: Principles and Applications*. vol. 29. Mineralog. Assoc. Canada (MAC) Short Course Series, Ottawa, pp. 239–243.
- van Kan Parker, M., Mason, P.R.D., van Westrenen, W., 2011. Experimental study of trace element partitioning between lunar orthopyroxene and anhydrous silicate melt: effects of lithium and iron. *Chem. Geol.* 285, 1–14.
- Van Westrenen, W., Van Orman, J.A., Watson, H., Fei, Y., Bruce Watson, E., 2003. Assessment of temperature gradients in multianvil assemblies using spinel layer growth kinetics. *Geochem. Geophys. Geosyst.* 4, 1036.
- Vander Kaaden, K.E., McCubbin, F.M., 2015. Exotic crust formation on mercury: consequences of a shallow, FeO-poor mantle. *J. Geophys. Res. Planets* 120, 195–209.
- Vogel, A.K., Jennings, E.S., Laurenz, V., Rubie, D.C., Frost, D.J., 2018. The dependence of metal-silicate partitioning of moderately volatile elements on oxygen fugacity and Si contents of Fe metal: implications for their valence states in silicate liquids. *Geochim. Cosmochim. Acta* 237, 275–293.
- Wade, J., Wood, B.J., 2005. Core formation and the oxidation state of the earth. *Earth Planet. Sci. Lett.* 236, 78–95.
- Wade, J., Wood, B.J., Tuff, J., 2012. Metal-silicate partitioning of Mo and W at high pressures and temperatures: evidence for late accretion of sulphur to the Earth. *Geochim. Cosmochim. Acta* 85, 58–74.
- Wade, J., Wood, B.J., Norris, C.A., 2013. The oxidation state of tungsten in silicate melt at high pressures and temperatures. *Chem. Geol.* 335, 189–193.
- Wadhwa, M., 2008. Redox conditions on small bodies, the Moon and Mars. *Rev. Mineral. Geochim.* 68, 493–510.
- Wang, Z., Laurenz, V., Petitgirard, S., Becker, H., 2016. Earth's moderately volatile composition may not be chondritic: evidence from In, Cd and Zn. *Earth Planet. Sci. Lett.* 435, 136–146.
- Wohlars, A., Wood, B.J., 2017. Uranium, thorium and REE partitioning into sulfide liquids: implications for reduced S-rich bodies. *Geochim. Cosmochim. Acta* 205, 226–244.
- Wood, B.J., Halliday, A.N., 2010. The lead isotopic age of the earth can be explained by core formation alone. *Nature* 465, 767–770.
- Wood, B.J., Kiseeva, E.S., Mirolo, F.J., 2014. Accretion and core formation: the effects of sulfur on metal-silicate partition coefficients. *Geochim. Cosmochim. Acta* 145, 248–267.
- Wykes J. L., O'Neill H. St. C. and Mavrogenes J. A. (2015) The effect of FeO on the sulfur content at sulfide saturation (SCSS) and the selenium content at selenide saturation of silicate melts. *J. Petrol.* 56, 1407–1424.
- Zolotov, M.Y., Sprague, A.L., Hauck, I.I.S.A., Nittler, L.R., 2013. The redox state, FeO content, and origin of sulfur-rich magmas on Mercury. *J. Geophys. Res.: Planets* 118, 138–146.